MORGAN & CLAYPOOL PUBLISHERS

Structure-Property Relationships under Extreme Dynamic Environments

Shock Recovery Experiments

Cyril L. Williams

SYNTHESIS SEM LECTURES ON EXPERIMENTAL MECHANICS

Structure-Property Relationships under Extreme Dynamic Environments

Shock Recovery Experiments

Synthesis SEM Lectures on Experimental Mechanics

Editor
Kristin Zimmerman, *SEM*

Synthesis SEM Lectures on Experimental Mechanics follow the technical divisions and the direction of The Society for Experimental Mechanics (SEM). The SEM is composed of international members of academia, government, and industry who are committed to interdisciplinary application, research and development, education and active promotion of experimental methods to: (a) increase the knowledge of physical phenomena; (b) further the understanding of the behavior of materials, structures and systems; and (c) provide the necessary physical basis and verification for analytical and computational approaches to the development of engineering solutions. The members of SEM encompass a unique group of experimentalists, development engineers, design engineers, test engineers and technicians, and research and development scientists from industry and educational institutions working in materials; modeling and analysis; strain measurement and structural testing.

Structure-Property Relationships under Extreme Dynamic Environments: Shock Recovery Experiments
Cyril L. Williams
2018

Mechanics of Materials Laboratory Course
Ghatu Subhash and Shannon Ridgeway
2018

The Old and New... *A Narrative on the History of the Society for Experimental Mechanics*
Cesar A. Sciammarella and Kristin B. Zimmerman
2018

Hole-Drilling Method for Measuring Residual Stresses
Gary S. Schajer and Philip S. Whitehead
2018

Structure-Property Relationships under Extreme Dynamic Environments: Shock Recovery Experiments

Cyril L. Williams

www.morganclaypool.com

ISBN: 9781681734521 paperback
ISBN: 9781681734538 ebook
ISBN: 9781681734545 hardcover

DOI 10.2200/S00880ED1V01Y201810SEM004

A Publication in the Morgan & Claypool Publishers series
SYNTHESIS SEM LECTURES ON EXPERIMENTAL MECHANICS

Lecture #4
Series Editor: Kristin Zimmerman, *SEM*
Series ISSN
Print 2577-6053 Electronic 2577-6088

Structure-Property Relationships under Extreme Dynamic Environments

Shock Recovery Experiments

Cyril L. Williams
Army Research Laboratory (ARL)

SYNTHESIS SEM LECTURES ON EXPERIMENTAL MECHANICS #4

MORGAN & CLAYPOOL PUBLISHERS

ABSTRACT

The inelastic response and residual mechanical properties acquired from most shock compressed solids are quite different from those acquired from quasi-static or moderate strain rates. For instance, the residual hardness of many shock compressed metals has been found to be considerably lower than those loaded under quasi-static conditions to the same maximum stress. However, the residual hardness of shock compressed metals is much higher than those loaded quasi-statically to the same total strain. These observations suggest that the deformation mechanisms active during inelastic deformation under shock compression and quasi-static or moderate rates may be quite different. Therefore, the primary objective of this short book is to offer the reader a concise introduction on the Structure-Property Relationships concerning shock compressed metals and metallic alloys via shock recovery experiments.

The first phase of the book, chapters 1 through 3 provides a brief historical perspective on the structure-property relationships as it pertains to shock compression science, then plastic deformation in shock compressed metals and metallic alloys is described in terms of deformation slip, deformation twinning, and their consequences to spall failure. Existing knowledge gaps and limitations on shock recovery experiments are also discussed. The fundamentals of shock wave propagation in condensed media are presented through the formation and stability of shock waves, then how they are treated using the Rankine-Hugoniot jump relations derived from the conservation of mass, momentum, and energy. The equation of states which govern the thermodynamic transition of a material from the unshock state to the shock state is briefly described and the elastic-plastic behavior of shock compressed solids is presented at the back end of the first phase of this book. The second phase of the book describes the geometry and design of shock recovery experiments using explosives, gas and powder guns. Then results derived from the residual mechanical properties, microstructure changes, and spall failure mechanisms in shock compressed metals and metallic alloys with FCC, BCC, and HCP crystal lattice structures are presented. Also, results on the residual microstructure of explosively compacted powders and powder mixtures are presented. Lastly, the book closes with the new frontiers in shock recovery experiments based on novel materials, novel microscopes, novel mechanical processing techniques, and novel time-resolved in-situ XRD shock experiments.

KEYWORDS

shock compression, high strain rate mechanics, dislocation slip, twining, texture evolution, microstructure evolution, phase transformation

To Sally and Yasmin for their patience and unwavering support during the preparation of this manuscript.

Contents

Preface

The primary objective of this book on the subject of *Structure-Property Relationships under Extreme Dynamic Environments* is to offer the reader a concise introduction on the shock compression of condensed matter via shock recovery experiments and stimulate new interests on the subject. The targeted readers are graduate students, and early to mid-career researchers who are pursuing research in the field of shock compression science. The first phase of the book, Chapters 1–3 provides a brief historical perspective on the structure-property relationships as it pertains to compression science, then describes plastic deformation in shock compressed metals and metallic alloys in terms of deformation slip, deformation twinning, and their consequences to spall failure. Existing knowledge gaps and limitations on shock recovery experiments are discussed. The fundamentals of shock wave propagation in condensed media are presented through the formation and stability of shock waves, then how they are treated using the Rankine-Hugoniot jump relations derived from the conservation of mass, momentum, and energy. The equation of states which govern the thermodynamic transition of a material from the unshocked state to the shocked state is briefly described and the elastic-plastic behavior of shock-compressed solids is presented at the back end of the first phase of this book. The second phase of the book (Chapter 4) describes the geometry and design of shock recovery experiments using explosives, gas, and powder guns. Then results derived from the residual mechanical properties, microstructure changes, and spall failure mechanisms in shock-compressed metals and metallic alloys with FCC, BCC, and HCP crystal lattice structures are presented. Also, results on the residual microstructure of explosively compacted powders and powder mixtures are presented. Finally, Chapter 5 concludes the book with the new frontiers in shock recovery experiments based on novel materials, novel microscopy techniques, novel mechanical processing techniques, and novel time-resolved in-situ XRD shock experiments.

This book would have been impossible without the involvement, interaction, and support provided by numerous researchers over the years. Therefore, I am grateful and indebted to them for such support. I am extremely grateful to a long-term colleague at the Army Research Laboratory, Dr. J. D. Clayton (ARL Fellow), for his encouragement, discussion on topics relating to mechanics and shock compression science, meticulous technical review of the final manuscript, and invaluable suggestions. His critique and suggestions were extremely crucial during the assembly of this book. The late Dr. D. P. Dandekar not only introduced me to shock compression science but also introduced me to numerous esteemed shock compression scientists and engineers who have influenced my research direction and thought process over the years. He was a great teacher and mentor and I was extremely fortunate to have him as a co-advisor on my doctoral thesis committee and to have worked with him for over a decade. I am not sure if I can

fully express my gratitude to my doctoral thesis advisor at The Johns Hopkins University, Prof. K. T. Ramesh, but I am extremely indebted to him for introducing me to the world of high rate mechanics. He continues to critique my work and provide very useful insights to my current research. I also thank my Master's thesis advisor at the University of Maryland Baltimore County, Prof. D. Arola, who introduced me to the fascinating subject of failure and fracture of engineering materials.

Dr. D. E. Grady (ARA, Sandia retired) has always being willing to discuss critical problems concerning shock wave research, I am fortunate and extremely thankful for his kindness. As veterans of the US military, Dr. Grady and I have swapped numerous intriguing military stories over the years, which I found to be priceless. I have been extremely auspicious to interact and continue to interact with Dr. W. P. Walters (BRL Fellow retired), Dr. T. Wright (ARL Fellow retired), Dr. J. Macauley (ARL Fellow retired), Dr. R. Becker (ARL Fellow), and Dr. B. Scott at the Army Research Laboratory. I thank them all for the invaluable technical and professional support they have provided over the years. Dr. M. A. Meyers (UCSD), Dr. G. Ravichandran (Caltech), Dr. N. N. Thadhani (Georgia Tech), Dr. G. T. Gray (LANL), and Dr. Y. M. Gupta (WSU) have provided me a wider perspective in shock compression science and are greatly acknowledged. Last but not least, I am thankful to a bright young post-doctoral fellow, Dr. Scott Turnage, for reviewing the final manuscript.

Everything should be made as simple as possible, but not simpler.
Albert Einstein (1879–1955), Theoretical Physicist and Nobelaureate

Cyril L. Williams
October 2018

CHAPTER 1

Introduction

Experimental research in shock compression science is traditionally categorized into two distinct groups: real-time (time-resolved in-situ) shock experiments and end-state (recovery) shock experiments. Unlike time-resolved in-situ shock experiments, which are designed to acquire the velocity-time history of the material being investigated, shock recovery experiments were developed to augment the acquired time-resolved velocity history of the shock wave profile. The primary objective of a well-designed shock recovery experiment is to interrogate the residual structure-property relationships of a material, which has undergone a known uniaxial strain history under shock compression and then released back to ambient conditions without being subjected to rogue radial release waves. Shock recovery experiments are also routinely employed to study incipient spall failure and the characteristics of spall surfaces. Shock recovery experiments are difficult to execute and the acquired microstructural data are often quite complex to interpret. This is partly due to the extreme conditions (such as high stresses, elevated temperatures, high strain-rates, etc.) the material undergoes during shock compression and release but also because of the short time-scales involved (nanosecond shock rise time and few microseconds to completion). In addition to the complexities stated above, there is an existing knowledge gap between the ambient-state and the end-state of the material interrogated. That is, shock recovery experiments do not provide any information between the ambient-state and the end-state. This poses some serious challenges on the interpretation of the microstructural data. However, coupling multiscale modeling with results acquired from shock recovery experiments can help in closing this existing knowledge gap. Nevertheless, end-state shock recovery experiments are well suited to study end-state phenomena such as spall failure and the residual structure/mechanical properties of materials which have been shock compressed and released to ambient conditions.

It is prudent at the early stages of this book on the subject of *Structure-Property Relationships under Extreme Dynamic Environments* to pose and answer three basic questions relevant to shock recovery experiments. (1) *What is a shock wave*? (2) *What are shock recovery experiments*? (3) *What is the relevance of shock wave research*? The answer to the first question is rather straight forward within the framework of mathematics. That is, a shock wave is simply a discontinuity or jump in principal mechanical and thermodynamic parameters such as particle velocity (or stress), strain, density, temperature, volume, etc. However, mathematical discontinuities do not occur in engineering materials. Although they are often used to approximate the shock rise time in shock wave problems, the shock rise time in engineering materials is finite. Therefore, the definition of a shock wave will be restated as follows. *A shock wave is a large amplitude nonlinear*

wave propagating at supersonic velocity, and across the boundary of the shocked and unshocked material, there exists a near-discontinuity or jump in principal mechanical and thermodynamic parameters such as particle velocity (or stress), strain, density, temperature, volume, etc.

The answer to the second question is not as straightforward compared to the definition of a shock wave. However, a general definition of shock recovery experiments can be stated as: *experiments through which a sample has been subjected to a well-defined shock stress and then soft recovered to study the residual structure-property relationships at different length-scales (atomic, nano, micro, meso, and macro) of the material in question*. A more detailed description of shock recovery experiments will be explored in Chapter 3.

Last, shock wave research is highly relevant because it plays a dominant role in most high-rate phenomena. It is a multidisciplinary subject spanning numerous fields such as condensed matter and plasma physics, chemistry, biology, engineering, materials science, medicine, seismology, and military technology. Although shock wave research pre-dates World War II, it radically expanded during and after World War II to create new fields of study such as nuclear explosions, supersonic and hypersonic aerodynamics, impact physics, dynamic fracture mechanics, gas dynamics, shock synthesis, explosive working and forming of metals, explosive cladding (welding) of metals, and laser fusion, to name a few. Some real-life occurrences of shock waves in aerodynamics and ballistics are shown in Figure 1.1 [1–4].

The primary objective of this book is to cultivate new interests in shock wave research pertaining to the structure-property relationships concerning new generations of materials such as nanocrystalline and ultra fine grained metals, high entropy alloys, long period stacking ordered (LPSO) structured materials, metamaterials, etc. The book is organized into five chapters. Chapter 1 provides a historical background on the subject of modern day shock recovery experiments since its inception in 1958 and then presents a brief summary of plastic deformation, spall failure, and bridging the knowledge gap in shock recovery experiments. Chapter 2 provides some background on the fundamentals of shock wave propagation in condensed media useful for understanding and interpreting shock wave data pertaining to the structure-property relationships in metals and metallic alloys. Shock recovery experiments are introduced in Chapter 3 and then a concise background on deformation mechanisms and spall failure is provided in Chapter 4. The book closes with Chapter 5 on the new frontier concerning shock recovery experiments. This book is in no way an exhaustive survey of shock wave research pertaining to the structure-property relationships in shock compressed solids. The reader is encouraged to read the following reviews on the topic [5–24].

1.1 HISTORICAL PERSPECTIVE ON THE STRUCTURE-PROPERTY RELATIONSHIPS PERTAINING TO SHOCK COMPRESSION SCIENCE

It is apparent from the annals of shock wave research that shock recovery experiments predate the World War II. For instance, Sir Charles Parsons in 1920 claimed to have synthesized

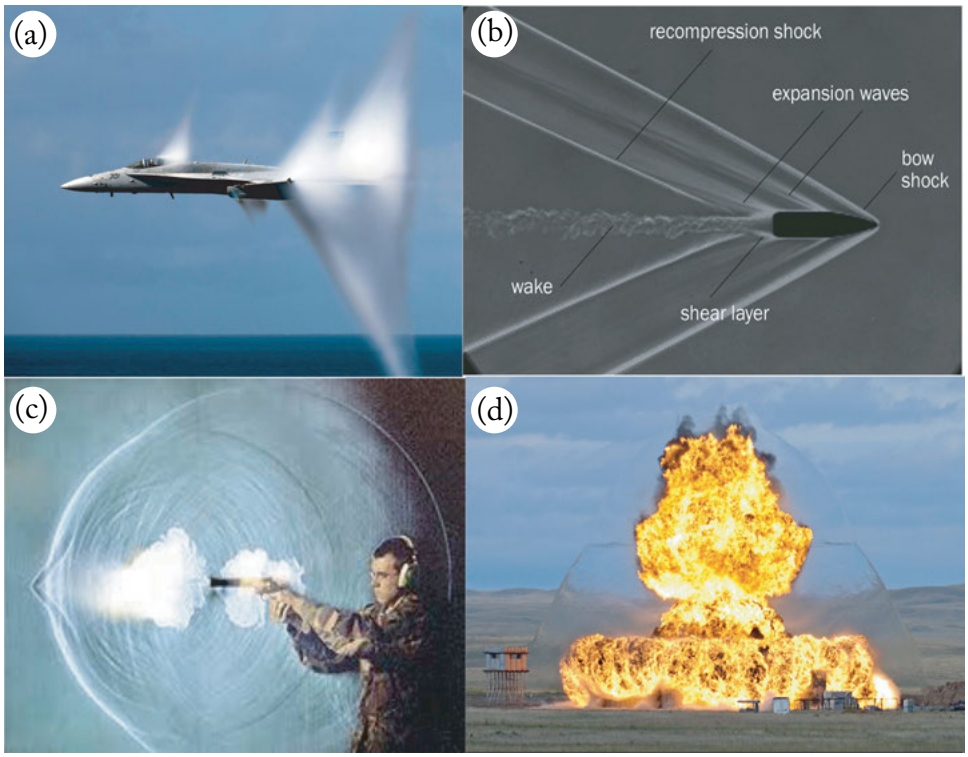

Figure 1.1: Shock waves in real life: (a) an F/A-18C Hornet Fighter jet transitioning to supersonic flight [1]; (b) a high velocity bullet in air with a bow shock at it's nose and turbulence in its wake [2]; (c) a handgun forming two spherical shocks and a bow shock at the nose of the projectile [3]; and (d) an expanding hemi-spherical shockwave from a high explosive warhead [4].

small amounts of carbon into diamond [25] although this claim has been disputed based on the pressure and temperature achieved during his experiment. Likewise, Michel-Levy and Wyart developed a unique recovery experiment in 1939 for the synthesis of minerals [26]. Nonetheless, it is generally accepted that the foundations for modern day shock recovery experiments were laid down between the mid-1950s and mid-1960s. One of the first major breakthroughs in shock recovery experiments was the pioneering research and subsequent classic paper by Cyril Stanley Smith in 1958 on the *Metallographic Studies of Metals after the Passage of an Explosive Shock* [5]. Using a well-designed momentum trapping assembly to mitigate rogue radial release waves, Smith shock-loaded both Oxygen Free High Conductivity (OFHC) copper and α-Iron (Armco) up to 60 GPa and then recovered the samples for metallographic analyses. Smith observed numerous deformation twins in OFHC copper after the passage of approximately 20 GPa shock stress but concluded that their contribution to hardening was insignificant. Smith also

found that α-iron under shock compression develops Neumann bands (twin lamellae) but more importantly, the residual microstructure above 13 GPa transitioned to a different phase, which upon full release leaves a complex microstructure evocative of carbon-free martensite [5]. Prior to Smith's elegant research, momentum trapping rings were not routinely employed and, therefore, the validity of shock recovery experimental results were at best questionable and at worst flawed. Smith's work is considered a milestone in shock compression science and is the benchmark for modern day shock recovery experiments. Other noteworthy milestones in shock recovery experiments include the synthesis of diamond by P. S. Decarli and J. C. Jamieson [27], decomposition of inorganics by I. U. Riabinin [28], inorganic synthesis by Y. Horiguchi and Y. Nomura [29], polymerization of condensed monomers by G. A. Adadurov et al. [30], and powder compaction by O. R. Bergmann and J. Barrington [31]. Table 1.1 is a compilation of notable research derived from shock recovery experiments from 1956 and 1982.

It is clearly evident from Table 1.1 that research pertaining to shock recovery experiments increased globally after the work of C. S. Smith, especially in the United States (U.S.), Soviet Union (U.S.S.R.), and Japan. In the U.S., shock recovery experiments were conducted at Los Alamos National Laboratories (LANL), Sandia National Laboratories (SNL), and few private institutions such as Stanford Research Institute (SRI), the DuPont Company, and Battelle Laboratories. Synthetic diamond is a direct product of shock recovery experimental research in the U.S. and has led to its commercialization for use in the machine tool industry. Bergmann and Barrington [31] at the DuPont Company pioneered research in powder compaction and shock sintering which made it possible to produce cubic boron nitride in the U.S. During the same period, the U.S.S.R. was heavily engaged in shock chemistry and the research efforts by Adadurov et al. [30] led to the synthesis of polymers from condensed monomers. Using explosives, Ignatovich et al. [35] polymerized polycrystalline acrylamide under multiple shock loading conditions. Like the U.S., the U.S.S.R. was also heavily engaged in the production of synthetic diamond. Furthermore, the Japanese were also conducting high level research in shock compression science via recovery experiments. Synthesis of titanium carbide and zinc ferrite from their powder form were achieved by Horiguchi and Nomura [29] and Kimura [32], respectively. The techniques developed for shock recovery experiments between 1950 and 1970 are still employed in contemporary shock recovery experiments with minor modifications.

1.2 A BRIEF BIOGRAPHY OF CYRIL STANLEY SMITH

This book on the subject of *Structure-Property Relationships under Extreme Dynamic Environments* would not be complete without a brief biography on the *father* of modern day shock recovery experiments. Cyril Stanley Smith (shown in Figure 1.2 with the front page of his pioneering paper) was a man of great engineering and scientific repute. He was born in Birmingham, England in 1903 and received his B.Sc. degree in metallurgy from the University of Birmingham in 1924 [47, 48]. He then immigrated to the United States and attained the Sc.D. degree in metallurgy in 1926 at the Massachussetts Institute of Technology (MIT), Cambridge, U.S. [47, 48].

Table 1.1: Research in shock compression science pertaining to the structure-property relationships conducted between 1956 and 1982

Year	Research Topic	Researchers	Country	Ref.
1956	Decomposition of inorganics	I. U. Riabinin	U.S.S.R.	[28]
1958	Metallography of iron	C. S. Smith	U.S.	[5]
1961	Synthesis of diamond	P. S. Decarli and J. C. Jamieson	U.S.	[27]
1963	Inorganic synthesis	Y. Horiguchi and Y. Nomura	Japan	[29]
1963	Shock synthesis	Y. Kimura	Japan	[32]
1965	Polymerization	G. A. Adadurov et al.	U.S.S.R.	[30]
1966	Powder compaction	O. R. Bergmann and J. Barrington	U.S.	[31]
1966	Vulcanization of rubber	I. M. Barkalov et al.	U.S.S.R.	[33]
1969	Polymerization	Babare et al.	U.S.S.R.	[34]
1970	Polymerization	Ignatovich et al.	U.S.S.R.	[35]
1970	Dynamic fracture	T. Barbee et al.	U.S.	[36]
1971	Shock recovery assembly	Adadurov et al.	U.S.S.R.	[37]
1972	Shock recovery assembly	A. L. Stevens and O. Jones	U.S.	[38]
1975	Shock recovery assembly	R. N. Orava and R. H. Wittman	U.S.	[10]
1975	Defect generation	L. E. Murr and K. P. Staudhammer	U.S.	[39]
1976	Dynamic fracture	L. Seaman et al.	U.S.	[40]
1980	Shock chemistry	R. A. Graham et al.	U.S.	[41]
1981	Shock synthesis	B. Olinger and L. R. Newkirk	U.S.	[42]
1981	Shock consolidation	M. A. Meyers et al.	U.S.	[43]
1981	Shock recovery assembly	P. S. Decarli and M. A. Meyers	U.S.	[9]
1981	Defect generation	L. E. Murr	U.S.	[13]
1982	Defect generation	J. E. Vorthman and G. E. Duvall	U.S.	[44]
1982	Shock compaction	A. Sawaoka et al.	Japan	[45]
1982	Shock recovery assembly	L. Davison et al.	U.S.	[46]

He worked for the American Brass Company as a research metallurgist for about 15 years, then joined the War Metallurgy Committee and shortly after, the Manhattan Project at Los Alamos Scientific Laboratory. There he directed metallurgical research on fissionable materials in support of the development of the atomic bomb [48]. Smith was awarded the Presidential Medal for Merit in 1946 for his work at Los Alamos [48].

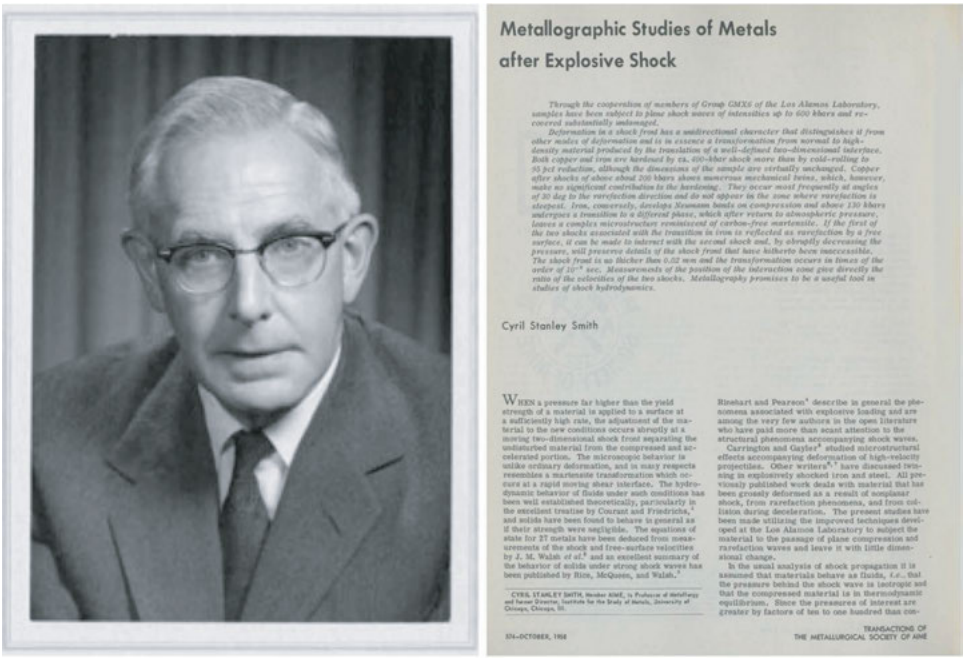

Metallographic Studies of Metals after Explosive Shock

Through the cooperation of members of Group GMX6 of the Los Alamos Laboratory, samples have been subject to plane shock waves of intensities up to 600 kbars and recovered substantially undamaged.

Deformation in a shock front has a unidirectional character that distinguishes it from other modes of deformation and is in essence a transformation from normal to high-density material produced by the translation of a well-defined two-dimensional interface. Both copper and iron are hardened by ca. 400-kbar shock more than by cold-rolling to 95 pct reduction, although the dimensions of the sample are virtually unchanged. Copper after shocks of above about 200 kbars shows numerous mechanical twins, which, however, make no significant contribution to the hardening. They occur most frequently at angles of 30 deg to the rarefaction direction and do not appear in the zone where rarefaction is steepest. Iron, conversely, develops Neumann bands on compression and above 130 kbars undergoes a transition to a different phase, which after return to atmospheric pressure, leaves a complex microstructure reminiscent of carbon-free martensite. If the first of the two shocks associated with the transition in iron is reflected as rarefaction by a free surface, it can be made to interact with the second shock and, by abruptly decreasing the pressure, will preserve details of the shock front that have hitherto been inaccessible. The shock front is no thicker than 0.02 mm and the transformation occurs in times of the order of 10^{-9} sec. Measurements of the position of the interaction zone give directly the ratio of the velocities of the two shocks. Metallography promises to be a useful tool in studies of shock hydrodynamics.

Cyril Stanley Smith

WHEN a pressure far higher than the yield strength of a material is applied to a surface at a sufficiently high rate, the adjustment of the material to the new conditions occurs abruptly at a moving two-dimensional shock front separating the undisturbed material from the compressed and accelerated portion. The microscopic behavior is unlike ordinary deformation, and in many respects resembles a martensite transformation which occurs at a rapid moving shear interface. The hydrodynamic behavior of fluids under such conditions has been well established theoretically, particularly in the excellent treatise by Courant and Friedrichs,[1] and solids have been found to behave in general as if their strength were negligible. The equations of state for 27 metals have been deduced from measurements of the shock and free-surface velocities by J. M. Walsh *et al.*[2] and an excellent summary of the behavior of solids under strong shock waves has been published by Rice, McQueen, and Walsh.[3]

Rinehart and Pearson[4] describe in general the phenomena associated with explosive loading and are among the very few authors in the open literature who have paid more than scant attention to the structural phenomena accompanying shock waves.

Carrington and Gaylor[5] studied microstructural effects accompanying deformation of high-velocity projectiles. Other writers[6,7] have discussed twinning in explosively shocked iron and steel. All previously published work deals with material that has been grossly deformed as a result of nonplanar shock, from rarefaction phenomena, and from collision during deceleration. The present studies have been made utilizing the improved techniques developed at the Los Alamos Laboratory to subject the material to the passage of plane compression and rarefaction waves and leave it with little dimensional change.

In the usual analysis of shock propagation it is assumed that materials behave as fluids, *i.e.*, that the pressure behind the shock wave is isotropic and that the compressed material is in thermodynamic equilibrium. Since the pressures of interest are greater by factors of ten to one hundred than cor-

CYRIL STANLEY SMITH, Member AIME, is Professor of Metallurgy and Former Director, Institute for the Study of Metals, University of Chicago, Chicago, Ill.

574—OCTOBER, 1958

TRANSACTIONS OF THE METALLURGICAL SOCIETY OF AIME

Figure 1.2: Cyril S. Smith and his pioneering research paper on the metallographic studies of metals after explosive shock [48].

After the Manhattan Project, Smith joined the University of Chicago in 1946 where he founded and became the first director of the Institute for the Study of Metals. This was the first interdisciplinary research organization in the United States dealing with materials research [48]. Professor Smith moved back to his alma mater (MIT) in 1961 [47] where he held joint appointments in the Department of Metallurgy and Humanities until his retirement in 1969. He was appointed by President Truman as one of the original members to the general advisory committee to the Atomic Energy Commission. He also served on other notable committes such as the Committee on Science and Public Policy of the National Academy of Sciences, the President's Science Advisory Committee, and Smithsonian Council [48]. Professor Smith was a world-renowned metallurgist and historian of metallurgy. Professor Smith was a member of numerous organizations, including the National Academy of Sciences (NAS), the American Academy of Arts and Sciences, the American Society of Metals (ASM), and the American Physical Society

(APS). He was also an honorary member of the Japan Institute of Metals, the Indian Institute of Metals, and the Akademie der Wissenschaften (Germany). Smith pioneered the application of material science and engineering to the study of archaeological artifacts. Professor Smith was the first chairman of the board of governors of Acta Metallurgica, and he authored several books [49–51] and about 200 journal articles. Professor Smith died on August 25, 1992 in Cambridge, Massachusetts, USA.

1.3 PLASTIC DEFORMATION IN SHOCK COMPRESSED METALS AND METALLIC ALLOYS

The plastic response of metals and metallic alloys under shock compression is substantially different from those observed under quasi-static or moderate strain rates. It is well known that the mechanical properties acquired from most shock recovered metals and metallic alloys are quite different than those acquired from quasi-static to moderate strain rates [6] (from this point forward, the usage of the word *metals* will imply both *metals and metallic alloys* unless otherwise specified). For instance, the residual hardness of many shock compressed metals has been found to be considerably lower than those compressed under quasi-static conditions to the same maximum stress [52, 53]. However, the residual hardness of shock compressed metals are much higher than those compressed quasi-statically to the same total strain [6, 7, 11–16, 23, 24, 52, 53]. It is noteworthy that shock hardening is not ubiquitous in metals. For instance, 6061-T6 aluminum and Ti-6Al-4V titanium alloys do not show any significant shock hardening as compared to the quasi-static case [54, 55]. These observations suggest that the deformation mechanisms active during shock compression are quite different from those active during quasi-static and moderate strain rates.

Plastic deformation in single or polycrystalline metals at high rates can be accommodated by two principal deformation mechanisms: deformation slip and deformation twinning. Slip and twinning may be active jointly or exclusively. However, for most metals, slip is the dominant deformation mechanism under low-to-moderate strain rates at room temperature. Twinning may be dominant at higher strain rates such as those experienced under shock compression and at low temperatures [13, 56–59]. It is well known that deformation twinning is profuse in shock-compressed metals with hexagonal close-packed lattice structures due to their limited slip systems compared to their FCC and BCC counterparts [60–64]. Deformation twins have also been observed in shock-compressed metals with higher numbers of slip systems at room temperature such as copper (FCC) [11, 56, 65, 66], nickel (FCC) [11, 52, 67], iron (BCC) [5, 68, 69], and tantalum (BCC) [70–74].

1.3.1 DEFORMATION SLIP

A microscopic description of plastic deformation is warranted as a prelude to understanding the shock-compressed behavior of metals prior to spall failure, for which the material first under-

goes shock compression and then tensile failure. Plastic deformation by crystallographic slip is accommodated through the motion of edge and screw dislocations along available slip planes and slip directions (slip system). Suppose a tensile force (P) is applied along the longitudinal axis of a single crystal metal bar, as shown in Figure 1.3a. The force (P) can be resolved along the slip direction with unit vector **b** and the normal direction to the slip plane with unit vector **n**, respectively. Taking into consideration the slip plane area (A_s=A_o/ cos ϕ, where A_o is the cross-sectional area of the bar), the resolved shear stress acting on the slip plane and along the slip direction (**b**) is easily determined to be $\tau_{RSS} = \sigma \cos\phi \cos\lambda$ (Schmid's law), where σ (=P/A_o) is the applied normal stress. When the τ_{RSS} reaches some critical value which is characteristic of the single crystal, then plastic flow initiates. This critical resolved shear stress is related to the tensile yield stress through Schmid's law $\sigma_y = \tau_{CRSS}/m$, where m (=cos ϕ cos λ) is the Schmid factor. Schmid's law implies that yielding will occur on the slip system possessing the largest Schmid factor.

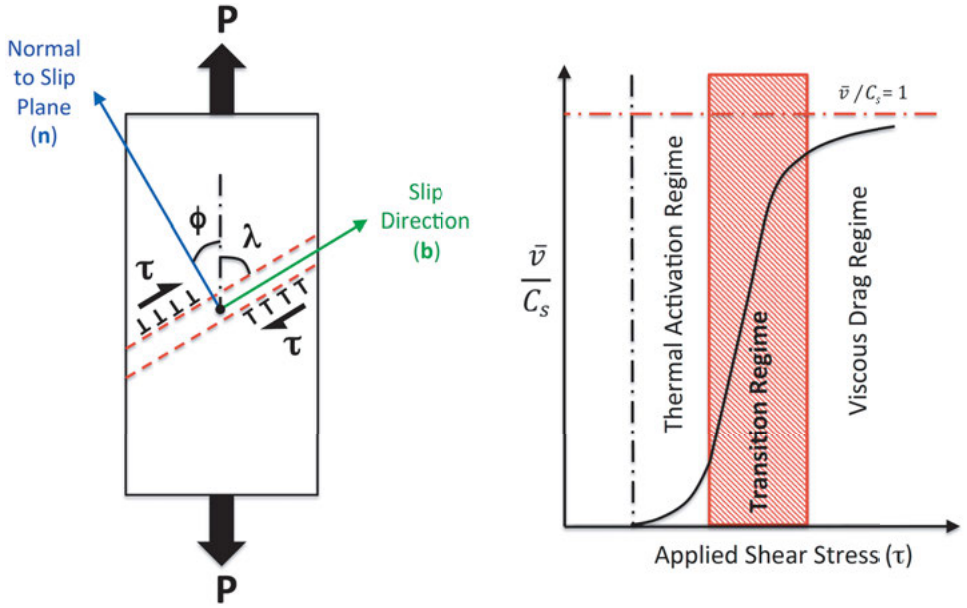

Figure 1.3: An illustration of (a) crystallographic slip in a metallic single crystal and (b) mean dislocation velocity as a function of applied shear stress.

Under the action of shear stresses, both edge, screw, mixed, and partial dislocations accelerate rapidly to a high velocity along the appropriate slip system, as illustrated in Figure 1.3 (with edge dislocation velocity being higher than that of screw [75]). Figure 1.3b reveals the three distinct regimes governing dislocation motion in condensed matter, namely, the thermal

activation regime, the transition regime, and the viscous drag regime [53, 76–78]. If plastic deformation occurs solely by crystallographic slip, then the mean dislocation velocity ($\bar{v}$) is related to the shear strain rate ($\dot{\gamma}$) by the Orowan equation [79]

$$\dot{\gamma} = bN_m\bar{v}, \tag{1.1}$$

where b is the magnitude of the Burgers vector and N_m is the mobile dislocation density. The Orowan equation stipulates that increasing the mobile dislocation density or velocity will increase the shearing rate. The Orowan equation was first applied to shock wave research by Duvall [80] and then quantitatively applied to the shock wave response of materials by Taylor [81]. As dislocations accelerate rapidly to higher velocities, the mobile dislocations encounter energy barriers (obstacles) such as solute atoms, vacancies, inclusions, precipitates (semicoherent to noncoherent), boundaries (grain, twin, etc.), and other dislocations (mobile and immobile). These barrriers are either short-range or long-range; they hinder dislocation motion and must be overcome to accommodate plastic deformation.

Short-range barriers emanate from the lattice structure itself and they affect dislocation motion from one atom to another in a single lattice. They may include the Peierls–Nabarro stress which is the primary short-range barrier for body-centered cubic (BCC) metals, point defects such as vacancies and self-interstitials, substitutional atoms, alloying elements, or forest dislocations which are the primary short-range resistance for face-centered cubic (FCC) and hexagonal-close packed (HCP) metals [58, 78]. Long-range barriers are typically several orders of magnitude larger than short-range barriers or the lattice spacing. They correspond to the elastic stress fields of other dislocations, grain boundaries, and point defects. Short-range barriers can be overcome partly through the process of thermal activation which results in large thermal vibrations that assist the dislocation in overcoming the obstacle and partly by the action of the net shear stress due to the applied external forces. On the other hand, long-range barriers are athermal because thermal activation does not significantly affect dislocations in overcoming them [53, 58, 78]. However, increases in thermal energy affect long-range barriers in two ways. First, through the temperature dependence of the elastic modulus, in particular the shear modulus, and, second, through the effect of the temperature history on the microstructure, in particular the dislocation density. Therefore, it is customary to decouple the flow stress into the thermal component which is associated with short-range barriers and the athermal component which is associated long-range barriers when studying temperature effects on dislocation motion [53, 58, 78, 82].

At higher shear stresses and shear strain-rates, the mechanism governing dislocation motion will transition from thermal activation to viscous drag, as shown in Figure 1.3b [83]. Dislocation motion is primarily dominated by phonon drag in the viscous drag regime. Phonons are elastic waves that arise from vibrating atoms within the crystal, they are definite discrete unit or quantum of vibrational mechanical energy. Phonons impede dislocation motion and phonon drag is primarily facilitated by phonon scattering [76, 84, 85]. Upon the action of external stresses, the fast-running dislocation will attain a steady-state velocity and equilibrium

will be achieved when the applied shear stress (τ) is related to the dislocation velocity (v) in accordance with the following equation:

$$\tau b = Bv, \tag{1.2}$$

where b is the magnitude of the Burgers vector and B is the viscous drag coefficient which is expressed as [86]

$$B = \frac{B_o}{1 - \left(\frac{v}{v_s}\right)^2}, \tag{1.3}$$

where B_o is the viscosity at ambient conditions (zero velocity) and v_s is the shear wave speed. As the dislocation velocity increases, the viscous drag increases. However, it is obvious from the above equation and Figure 1.3b that the dislocation velocity cannot equal or exceed the shear wave speed (the so-called forbidden velocity); the dislocation velocity approaches the shear wave speed asymptotically. Although analytical and computational models have shown the existence of supersonic dislocations [87–91], their existence has not yet been realized or verified experimentally.

1.3.2 DEFORMATION TWINNING

To maintain continuity at grain boundaries in a crystalline solid under an arbitrary plastic deformation field, at least five independent slip systems must be activated simultaneously [92]. Failure to meet such a criterion can lead to premature fracture of the crystalline solid. However, if a crystalline solid does not have sufficient independent slip systems available for activation, then in some metals twinning may be activated to provide the additional deformation mechanisms necessary to accommodate the arbitrary shape change. A twin in a crystalline solid is defined as a region of the crystal in which the orientation of the lattice is a mirror image of that of the matrix material. The boundary between the twinned and un-twinned (matrix or parent) material is delineated by a coherent planar interface called a twin boundary. Figure 1.4 is a representation of an undeformed material without twins and a twinned material. The formation of a twin by shearing between each parallel plane of atoms is illustrated in Figure 1.4b. Dislocation movement during deformation slip takes place in multiples of the unit displacement or dislocation Burger's vector. In contrast, shear displacement during twinning is a fraction of the interatomic repeat distance, that is, every atomic plane shears relative to its neighboring plane. Twinning and slip are highly competitive deformation processes over a wide temperature range. Twins are classified by how they are formed. Those formed during recrystallization are called annealing twins and those formed during deformation are called mechanical or deformation twins. Nevertheless, this book is primarily concerned with mechanical or deformation twinning.

Deformation twinning is prevalent in metals with HCP crystal lattice structure because basal, prismatic, and pyramidal slip do not provide the five independent slip systems necessary

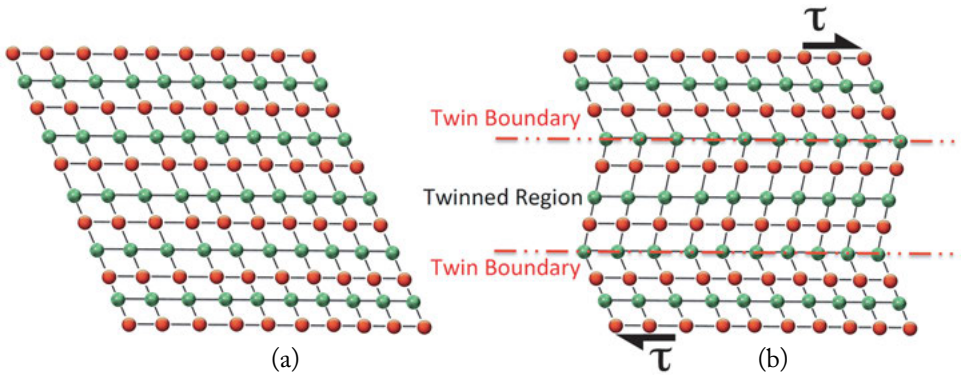

Figure 1.4: Formation of a deformation twin by shear (a) undeformed solid and (b) deformed solid revealing a twinned region and associated twin boundaries.

to accommodate arbitrary shape change, especially when $\langle a + c \rangle$ pyramidal slip is not possible. Twinning has been observed on numerous distinct planes in HCP metals and their alloys. The most common twinning system observed in these HCP metals and their alloys is the $\{10\bar{1}2\}\langle 10\bar{1}1 \rangle$ tensile twinning system [93–100]. Other slip and twinning systems observed in various materials with FCC, BCC, and HCP crystal lattice structures are listed in Table 1.2. Twinning has also been extensively studied in materials with body centered cubic (BCC) crystal lattice structures such as ferritic steels because of their importance in engineering structures. For instance, deformation twins or Neumann bands (as they are referred to in steels) are readily observed in ferritic steels under shock compression at room temperature and low-temperature conditions. A common twinning plane in ferritic steels is the {112} with the shearing direction parallel to $[\bar{1}\bar{1}1]$ [101]. Twinning systems observed in other BCC materials are listed in Table 1.2. Metals with FCC lattice crystal structure exhibit the least propensity for twinning when compared to their BCC and HCP counterparts. Nevertheless, FCC metals are known to twin under cryogenic temperatures and high strain rates, especially those with low stacking fault energies. A common twinning system observed in metals with FCC crystal lattice structure is the $\{111\}\langle 11\bar{2} \rangle$ twinning system; see Table 1.2 for other twinning systems observed in various FCC metals.

Deformation twinning is highly favored in shock-compressed solids because of the high stresses and high strain rates involved [68, 70, 109–114]. For instance, some metals that do not twin under ambient temperature are known to twin under shock compression [115]. Twinning depends on several factors such as stress [39, 52, 116], pulse duration [39, 117, 118], as-received substructure [119, 120], grain size [118, 121], stacking fault energy [112, 122], and crystallographic texture [123, 124]. In general, twin density has been found to increase with increase in shock stress [68, 124, 125] and pulse duration [117, 126]. Furthermore, it has been shown that

Table 1.2: Slip and twinning systems for selected materials with FCC, BCC, and HCP crystal lattice structures at room temperature

Metal	Density (g/cc)	Crystal Structure	Slip System	Twinning System	Reference
Al	2.70	FCC	$\{111\}\langle 110\rangle$		[102]
Cu	8.93	FCC	$\{111\}\langle 110\rangle$	$\{111\}\langle 11\bar{2}\rangle$	[102]
Au	19.32	FCC	$\{111\}\langle 110\rangle$	$\{111\}\langle 11\bar{2}\rangle$	[102]
Ag	10.49	FCC	$\{111\}\langle 110\rangle$	$\{111\}\langle 11\bar{2}\rangle$	[103]
α-Fe	7.87	BCC	$\{110\}\langle 111\rangle$ $\{112\}\langle 111\rangle$ $\{123\}\langle 111\rangle$	$\{112\}\langle 11\bar{1}\rangle$	[104, 105]
W	19.30	BCC	$\{110\}\langle 111\rangle$	$\{112\}\langle 11\bar{1}\rangle$	[106]
Mo	10.22	BCC	$\{110\}\langle 111\rangle$	$\{112\}\langle 11\bar{1}\rangle$ $\{441\}$ $\{332\}$	[106]
Cr	7.19	BCC	$\{110\}\langle 111\rangle$	$\{112\}\langle 11\bar{1}\rangle$	[106]
Mg	1.74	HCP	$(0001)\langle 2\bar{1}\bar{1}0\rangle$ $\{10\bar{1}0\}\langle 2\bar{1}\bar{1}0\rangle$ $\{10\bar{1}1\}\langle 2\bar{1}\bar{1}0\rangle$ $\{11\bar{2}2\}\langle 11\bar{2}3\rangle$	$\{10\bar{1}2\}\langle 10\bar{1}\bar{1}\rangle$ $\{10\bar{1}\bar{1}\}\{10\bar{1}2\}$ $\{10\bar{1}3\}\{30\bar{3}2\}$	[95, 106]
Be	1.84	HCP	$(0001)\langle 2\bar{1}\bar{1}0\rangle$ $\{10\bar{1}0\}\langle 2\bar{1}\bar{1}0\rangle$	$\{10\bar{1}2\}\langle 10\bar{1}\bar{1}\rangle$	[106]
Ti	4.50	HCP	$(0001)\langle 2\bar{1}\bar{1}0\rangle$ $\{10\bar{1}1\}\langle 2\bar{1}\bar{1}0\rangle$ $\{10\bar{1}0\}\langle 2\bar{1}\bar{1}0\rangle$	$\{10\bar{1}2\}\langle 10\bar{1}\bar{1}\rangle$ $\{10\bar{2}1\}\langle 11\bar{2}6\rangle$ $\{10\bar{2}2\}\langle 11\bar{2}3\rangle$	[106]
α-Zr	6.53	HCP	$(0001)\langle 2\bar{1}\bar{1}0\rangle$ $\{10\bar{1}1\}\langle 2\bar{1}\bar{1}0\rangle$ $\{10\bar{1}0\}\langle 2\bar{1}\bar{1}0\rangle$	$\{10\bar{1}2\}\langle 10\bar{1}\bar{1}\rangle$ $\{10\bar{2}1\}\langle 11\bar{2}6\rangle$ $\{10\bar{2}2\}\langle 11\bar{2}3\rangle$	[107, 108]

profuse twinning occurs in annealed materials but not in pre-deformed materials with reasonably high dislocation density [119, 120, 127]. Materials with large grains or low stacking fault energy have also been shown to twin more readily than those with small grains or high stacking fault energy [112, 118, 121, 122].

1.4 SPALL FAILURE IN METALS AND METALLIC ALLOYS

Spall failure is prevalent in materials subjected to high velocity impact events, and in order to mitigate spallation it is essential to understand the underlying fundamental failure mechanisms. Spall failure occurs in metals when two strong decompression or rarefaction waves collide and in the process generate a tensile region in the material. For metals, if the tensile stresses developed are greater than the threshold required for void nucleation, growth, and coalescence, then spall failure will occur in the material. This is also true for brittle materials; however, nucleation, growth, and coalescence of microcracks is the dominant failure mechanism. Spall failure is essentially a rate-dependent process and therefore, spall strength is not considered to be an intrinsic material property. It is strongly a function of shock stress, pulse duration, strain-rate, and other parameters of state. The strain rates usually associated with the spall process from gas gun plate impact experiments can be quite high, ranging from $10^4\ s^{-1}$ to $10^6\ s^{-1}$ [128], and can be higher for explosives and laser shocks. In addition to the high strain rates, the material can also be subjected to extremely high compressive stresses under uniaxial strain conditions (in excess of 1 GPa) in comparison to dynamic compression under uniaxial stress conditions (typically in the MPa range).

The earliest observation of spall failure can be traced back to the work of Hopkinson in 1914 [129] and the phenomenon has been subsequently studied in metals by numerous researchers [74, 130–142]. It was established from early spall experiments that spallation is an evolutionary process in which complete failure of a material occurs through the nucleation and growth of voids or microfractures in the material [143]. The spall and release processes are illustrated in Figure 1.5 from the structural and microstructural perspective. Suppose a flyer plate is driven into a metallic target plate using a light gas gun; one should expect the microstructural response illustrated at the top of Figure 1.5 and the corresponding structural response shown at the bottom. For an elastic-plastic material, a two-wave structure is observed with the elastic precursor (E1 wave) arriving at the target free surface first. Beyond this point (B - Hugoniot Elastic Limit), the material can no longer sustain elastic distortions, then the response transitions from elastic to plastic (P1 wave). The regime between points C and F (shown in red) is responsible for accommodating plasticity through defect generation. Depending on the structure of the shock-compressed metal or metallic alloy, defects such as dislocations, deformation twins, vacancies, vacancy clusters, interstitial atoms, etc. are generated during the compression phase. For materials such as α-iron, polymorphic phase transformation from a BCC crystal lattice structure to HCP will occur at approximately 13 GPa and this is illustrated in the figure by the hypothetical phase transformation from a square lattice structure to triangular between points D and F. This

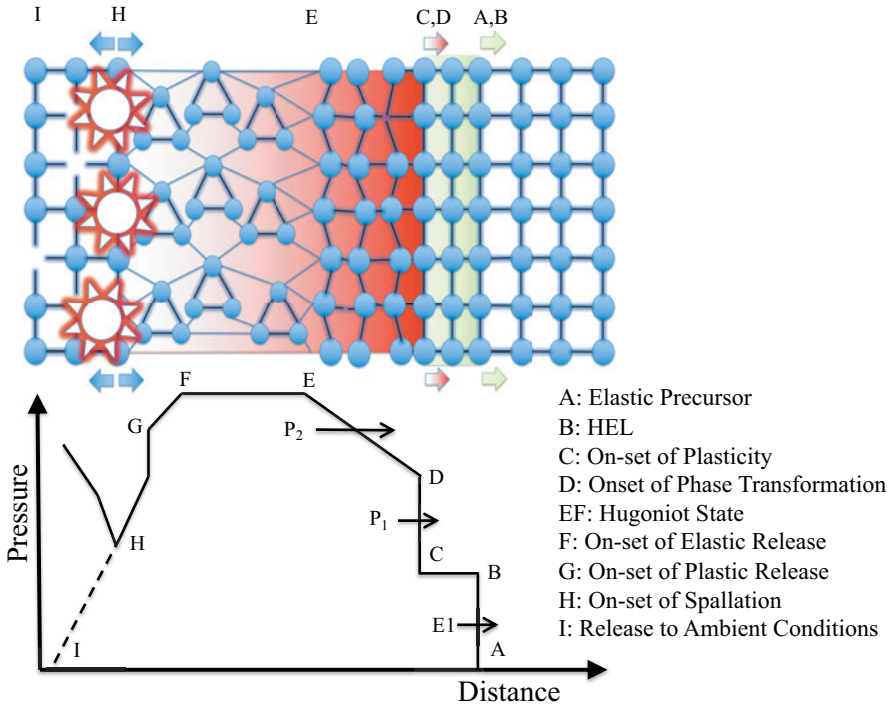

Figure 1.5: A simplified illustration of the various stages of a crystalline material which has been shock compressed and then released to ambient conditions or spalled.

transformation is manifested through a second plastic wave (P2 wave) at point D. A stable shock or Hugoniot state is achieved and maintained between points E and F and then the material releases elastically between points F and G then plastically between points G and H from the stable shock state, respectively. For metastable α-iron, the HCP crystal lattice structure reverts back to BCC upon full release. If the flyer material is thinner than that of the target, then spall failure occurs via the collision of decompression waves through void nucleation, growth, and coalescence if the threshold for failure is satisfied. If the flyer thickness is larger or an impedance match optical window is used, then the target material releases to ambient conditions (I).

Some of the earliest investigations sought to develop a criterion for characterizing the spall failure process. The first criterion developed was based on the premise that spallation occurred at a critical tensile stress which is characteristic of the material [129]. The stress rate or stress gradient criterion was later proposed by Skidmore [144] and Breed et al. [145] to explain the gradual evolution of damage. Soon after, a cumulative damage criterion was proposed by Tuler and Butcher [146] to study the time dependence of spall fracture. Also, the concept of damage as a rate process obeying the Arrhenius rate equations [147] for bond breakage and

healing was introduced by Tobolsky and Eyring [148] and Zhurkov [149]. Curran et al. [150] employ a versatile approach for studying the nucleation and growth (NAG) of voids in metals through empirical constitutive relationships derived from extensive structure-property relationships. Most of these criteria require experimental parameters in order to characterize specific materials, and usually these parameter must be obtained from well-designed shock experiments. In response to these requirements, numerous experimental techniques and diagnostic tools have been developed over the years [151–156].

The spall response of a material can be investigated over length scales on the order of nanometers to millimeters and time scales on the order of nanoseconds to microseconds. The plate impact experiment is the most common of all techniques used for interrogating the spall response of materials. They are generally carried out using gas or powder guns, explosives, electroexplosive devices (electric guns), and radiation devices (lasers). Plate impact experiments provide the ability to measure velocity or stress waveforms in real time and recover the shocked sample for metallurgical evaluation at the end-state. The coupling of both known velocity or stress wave histories and results from metallurgical evaluation is extremely valuable in studying the spall response and failure characteristics of a variety of materials [150, 157–159]. The spall strengths of various metals with FCC, BCC, and HCP crystal lattice structures are listed in Table 1.3. The list comprises of both corrected spall strengths, corrected for elastic-plastic effects and uncorrected spall strengths.

Gas and powder guns are popular because they are relatively straightforward to operate and offer the experimentalist the most control in repeatability. Conducting a gas or powder gun-driven plate impact experiment requires that a flyer plate mounted on a sabot be driven into a target plate, as illustrated in the Lagrangian diagram shown in Figure 1.6a. The impact velocity is acquired from velocity shorting pins or lasers and the free surface and/or particle velocity history of the target is measured using a velocity interferometer for any reflector (VISAR) or photon Doppler velocimetry (PDV), as shown in Figure 1.6b. Upon impact a state of uniaxial strain (lateral strains are zero and this topic will be treated in Chapter 2) is developed in both the flyer and target plates. Two elastic and shock compression waves traveling in the opposite direction are reflected from the flyer and target free surfaces as release or rarefaction waves (see Figure 1.6a). When the release or rarefaction waves collide in the target material (the target is always thicker than flyer for spall experiments), a tensile region is created and if the tensile stresses developed are greater than the threshold for void nucleation, growth, and coalescence then the metal will fail by spallation. This failure process occurring within the target material is interrogated at the free surface using VISAR or PDV; the velocity-time history is recorded as shown in Figure 1.6b and then analyzed. Numerous technical papers and reviews of the plate impact technique are available in the open literature [128, 160–163].

Table 1.3: Spall strength data for selected materials with FCC, BCC, and HCP crystal lattice structures. ρ, C_L, C_o, and σ^* are density, longitudinal sound speed, bulk sound speed, and spall strength, respectively.

Material	Grain Type	$\rho(g/cc)$	$C_L(km/s)$	$C_o(km/s)$	$\sigma^*(GPa)$	Ref.
Al AD1 (FCC)	Polycrystalline	2.71	6.40	5.25	0.87	[164]
Al 1100-O (FCC)	Polycrystalline	2.71	6.45	5.34	1.40	[138]
Al Pure (FCC)	Single Crystal [100]	2.70	6.40	5.77	1.36	[132]
Al Pure (FCC)	Single Crystal [111]	2.70	6.40	5.77	1.17	[132]
Cu M2 (FCC)	Polycrystalline	8.93	4.60	3.96	0.80	[165]
Cu OFHC (FCC)	Polycrystalline	8.93	4.60	3.96	1.20	[166]
Cu (FCC)	Single Crystal [111]	8.93	4.60	3.96	4.50	[165]
Cu (FCC)	Single Crystal [100]	8.93	4.60	3.96	4.50	[165]
Stainless 304 (FCC)	Polycrystalline	7.90	5.74	4.86	3.00	[166]
α-Iron (BCC)	Polycrystalline	7.80	5.97	4.65	1.54	[165]
Tantalum (BCC)	Polycrystalline	16.85	4.16	3.41	4.40	[166]
Molybdenum (BCC)	Polycrystalline	10.21	6.44	5.14	1.80	[136]
Molybdenum (BCC)	Single Crystal [111]	10.21	6.44	5.14	4.20	[136]
Molybdenum (BCC)	Single Crystal [100]	10.21	6.44	5.14	3.30	[136]
Nb (BCC)	Polycrystalline	8.56	5.11	4.52	4.70	[167]
Nb (BCC)	Single Crystal [110]	8.59	5.03	4.44	8.66	[168]
AMX602 (HCP)	Polycrystalline UFG	1.81	5.70	4.32	1.01	[169]
Mg AZ31B-4E (HCP)	Polycrystalline UFG	1.77	5.82	4.62	0.92	[140]
Ti-6Al-4V (HCP)	Polycrystalline	4.43	6.15	5.11	5.00	[170]
Be S200F (HCP)	Polycrystalline	1.85	13.20	8.03	5.00	[171]
Zn (HCP)	Polycrystalline	7.14	4.73	3.03	1.2	[172]
Zn (HCP)	Single Crystal [0001]	7.14	2.98	3.03	1.86	[172]
Zn (HCP)	Single Crystal $[10\bar{1}0]$	7.14	4.73	3.03	1.40	[172]

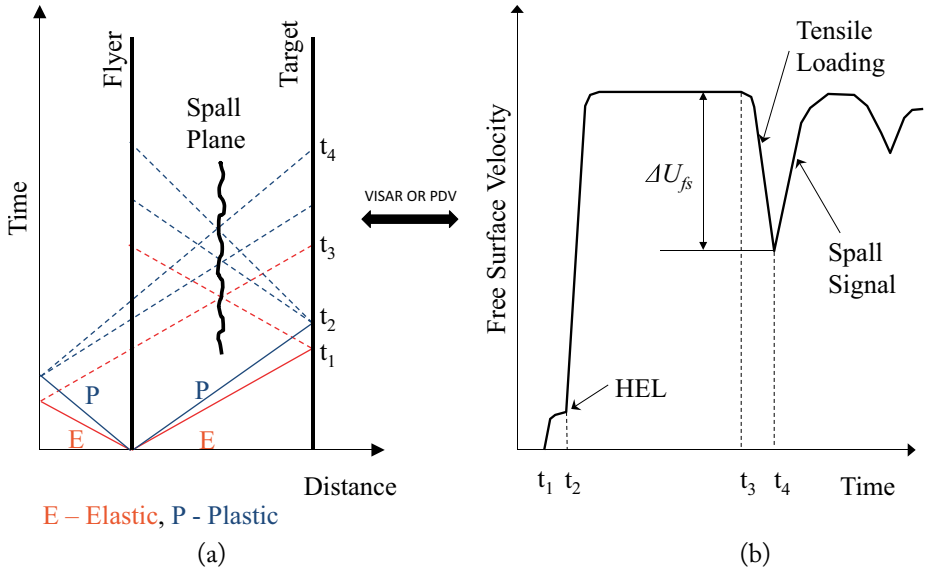

Figure 1.6: (a) A simplified Lagrangian diagram and (b) free surface velocity profile representative of the spall process.

1.5 BRIDGING THE KNOWLEDGE GAP IN SHOCK RECOVERY EXPERIMENTS

Shock recovery experiments are extremely useful for providing data on the residual structure-property relationships of a material that has been shock compressed and released back to ambient conditions. They are also routinely employed to study the microstructural aspects of spall failure. However, a knowledge gap exists between the ambient state and release state (end-state). That is, shock recovery experiments do not provide any information on the microstructure and its evolution between the ambient and release state. Hence, no structure-property relationships can be inferred at the shock state. The high stresses, high strain rates, and elevated temperatures involved under these extreme conditions make it difficult to study the structure-property relationships in real time via traditional shock recovery experiments.

The existing knowledge gap pertaining to shock recovery experiments is illustrated in Figure 1.7. Suppose a solid body under ambient conditions is deformed by a shock wave; every particle behind shock front in the solid body will be displaced in response to the imposed shock stress. Particles ahead of the shock front maintain their position in the reference configuration until the arrival of the shock wave. As shown in Figure 1.7, the particle at position X_1 at the ambient state (reference configuration) will be displaced by u_1 to a new position x_1 at the shock compressed state (intermediate configuration) after time t. When the solid body is released from the shock compressed state to the release state (current configuration), the particle at position

x_1 will be further displaced by u_2 to its final position x_2. As previously stated, shock recovery experiments do not provide any information on how the as-received microstructure at the reference configuration evolves to the current configuration or release state. This knowledge is extremely crucial in developing a fundamental understanding of the deformation mechanisms active under shock compression and release, and their role on the consequent failure of the solid body. Nevertheless, the shock compression science community is working diligently to address this crucial problem. The current state-of-the-art approach to bridging this knowledge gap is multi-scale modeling and time-resolved in-situ X-ray diffraction (XRD) shock experiments.

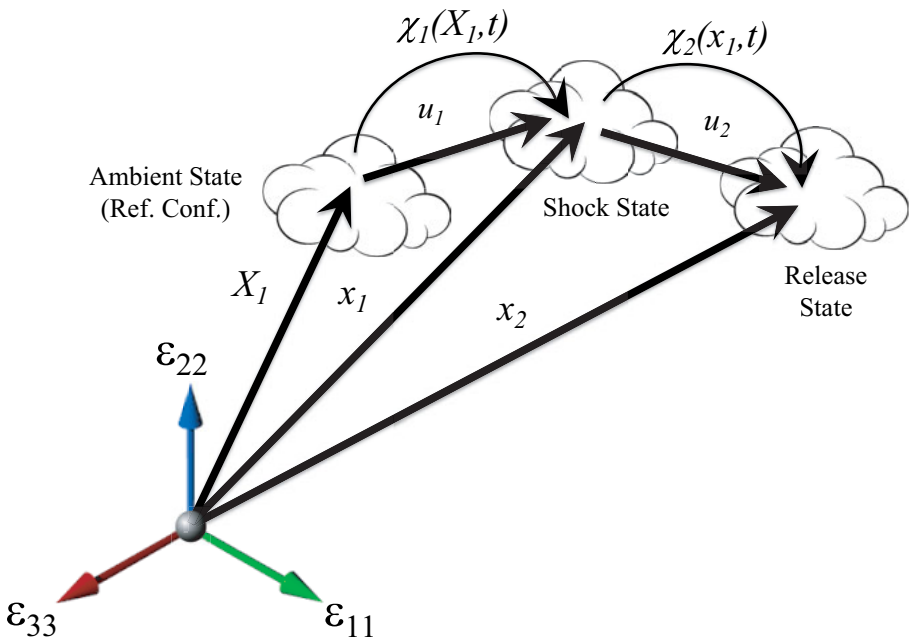

Figure 1.7: The decomposition of the deformation and release of a shock compressed body.

Multiscale modeling of materials involves different length and/or time scales over several orders of magnitudes. Multiscale modeling is gradually becoming a reliable scientific tool for investigating the shock response of condensed matter [173–187]. The length scales of interest and tools required for probing the various length scales and, therefore, bridging the existing knowledge gap in shock recovery experiments are shown in Figure 1.8. The length scales range from the atomic scale to the continuum scale and the tools for probing the various length scales range from High Resolution Transmission Electron Microscopy (HR-TEM) to optical microscopy. Although multiscale modeling is in its infancy, it has already proven to be extremely useful in providing some insights on the deformation mechanisms, microstructure evolution, and failure processes active at different stages of a shock compressed solid with reasonable ac-

curacy. Time-resolved in-situ XRD shock experiments are also emerging as a tool for studying the ambient, shock, and release states. Time-resolved in-situ XRD shock experiments can provide microstructural data essential for validating multiscale models and for interpreting data acquired from shock recovery experiments. Recent results acquired from time-resolved in-situ XRD shock experiments include [113, 153, 188–193]. Shock recovery experiments coupled with results derived from time-resolved in-situ XRD shock experiments and multiscale modeling will bridge the knowledge gap between the ambient and release states in shock-compressed solids.

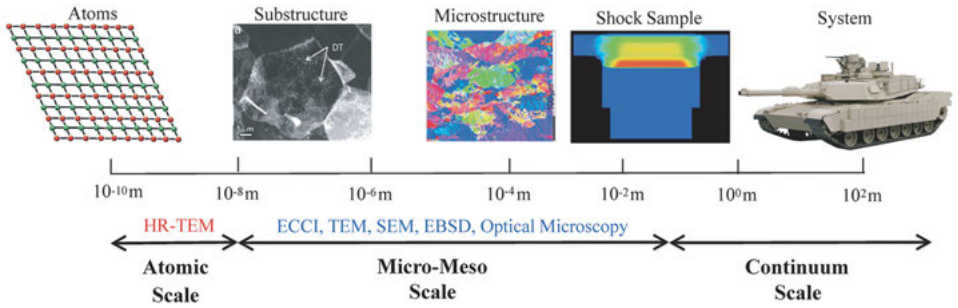

Figure 1.8: An illustration of the hierarchy employed in bridging the various length scale in multi-scale modeling (HR-TEM: High Resolution Transmission Electron Microscopy; ECCI: Electron Channeling Contrast Imaging; SEM: Scanning Electron Microscopy; EBSD: Electron Backscatter Diffraction).

CHAPTER 2

Shock Wave Propagation in Condensed Media

Materials subjected to impulsive loads can exhibit responses that are quite complex and the material response is normally dependent on the intensity of the impulse. Generally, the response of solids subjected to impulsive loads may be divided into three distinct regimes. For loading conditions that produce stresses below the dynamic yield point of the material, the material response is elastic. On the other hand, if the stresses generated are above the elastic limit, the material response will be plastic. With further increase in the intensity of the impulsive load, the stresses generated can exceed the yield strength of the material by several orders of magnitude. For such cases, the material may behave hydrodynamically. For an elastic-plastic material such as aluminum, impulsive loads exceeding the elastic limit can produce a two wave structure, a faster elastic precursor followed by a slower plastic wave (if the transient or shock wave in this case is not overdriven). The aim of this chapter is not to develop an exhaustive treatment of shock waves in condensed matter but to introduce pertinent subjects relating to the research at hand. For a more rigorous treatment of stress waves in solids, the following books are recommended Kolsky [194], Achenbach [195], Drumheller [196], Whitham [197], Wasley [198], Eringen and Suhubi [199], Meyers [58], Courant and Friedrichs [200], Grady [201, 202], and Johnson [203].

2.1 LINEAR ELASTIC MATERIAL

A good prelude to the theory of shock waves is the theory of three-dimensional wave motion in an isotropic linear-elastic material. The solutions to these linear equations are called linear waves. Although the complexities involved in analyzing linear waves are far less than those of nonlinear waves, linear waves do exhibit many important traits of wave propagation. In order to derive the wave equation for an isotropic linear-elastic material, it is necessary to invoke the system of equations governing the motion of a homogeneous isotropic linear-elastic body. These are the stress equation of motion (from balance of linear momentum), constitutive law (Hooke's law), and the strain-displacement relationships. From the balance of linear momentum, the stress equation of motion is

$$\frac{\partial \sigma_{ij}}{\partial x_j} + \rho b_i = \rho \frac{\partial^2 u_i}{\partial t^2}, \tag{2.1}$$

where σ is stress, ρ is density, u is displacement, b is body force, x is a Lagrangian point in the body, and t is time. For an isotropic linear-elastic solid, the constitutive relation is

$$\sigma_{ij} = 2\mu\epsilon_{ij} + \lambda\epsilon_{kk}\delta_{ij}, \tag{2.2}$$

where μ and λ are the Lame's constants and δ_{ij} is Kronecker delta. Furthermore, ϵ_{ij} is the strain and ϵ_{kk} is the dilatation, defined as follows:

$$\epsilon_{ij} = \frac{1}{2}\left(\frac{\partial u_i}{\partial x_j} + \frac{\partial u_j}{\partial x_i}\right) \tag{2.3}$$

$$\epsilon_{kk} = \epsilon_{11} + \epsilon_{22} + \epsilon_{33}. \tag{2.4}$$

Substituting Equation (2.3) into Equation (2.2) and recognizing that

$$\frac{\partial \epsilon_{kk}\delta_{ij}}{\partial x_j} = \frac{\partial \epsilon_{kk}}{\partial x_i}$$

and

$$\frac{\partial^2 u_j}{\partial x_j \partial x_i} = \frac{\partial}{\partial x_i}\left(\frac{\partial u_j}{\partial x_j}\right) = \frac{\partial \epsilon_{kk}}{\partial x_j},$$

the stress equation of motion (2.1) can be restated as

$$(\lambda + \mu)\frac{\partial \epsilon_{kk}}{\partial x_i} + \mu\frac{\partial^2 u_i}{\partial x_j \partial x_j} + \rho b_i = \rho\frac{\partial^2 u_i}{\partial t^2}. \tag{2.5}$$

Replacing

$$\frac{\partial^2}{\partial x_j \partial x_j} = \left(\frac{\partial^2}{\partial {x_1}^2} + \frac{\partial^2}{\partial {x_2}^2} + \frac{\partial^2}{\partial {x_3}^2}\right)$$

with the del operator ∇^2 and ϵ_{kk} with $\triangle$, Equation (2.5) can be further restated as

$$(\lambda + \mu)\frac{\partial \triangle}{\partial x_1} + \mu \nabla^2 u_1 + \rho b_1 = \rho\frac{\partial^2 u_1}{\partial t^2} \tag{2.6}$$

$$(\lambda + \mu)\frac{\partial \triangle}{\partial x_2} + \mu \nabla^2 u_2 + \rho b_2 = \rho\frac{\partial^2 u_2}{\partial t^2} \tag{2.7}$$

$$(\lambda + \mu)\frac{\partial \triangle}{\partial x_3} + \mu \nabla^2 u_3 + \rho b_3 = \rho\frac{\partial^2 u_3}{\partial t^2}. \tag{2.8}$$

Equations (2.6), (2.7), and (2.8) are the equations of motion of an isotropic linear elastic solid and are used to develop the equations for the propagation of longitudinal (dilatational) and

shear (distortional) waves. Taking the partial derivatives of Equations (2.6), (2.7), and (2.8) with respect to x_1, x_2, and x_3, respectively, and summing, we get

$$\begin{aligned}
&\left[(\lambda+\mu)\frac{\partial^2\triangle}{\partial {x_1}^2}+\mu\frac{\partial}{\partial x_1}\bigtriangledown^2 u_1+\rho\frac{\partial}{\partial x_1}b_1\right]+\\
&\left[(\lambda+\mu)\frac{\partial^2\triangle}{\partial {x_2}^2}+\mu\frac{\partial}{\partial x_2}\bigtriangledown^2 u_2+\rho\frac{\partial}{\partial x_2}b_2\right]+\\
&\left[(\lambda+\mu)\frac{\partial^2\triangle}{\partial {x_3}^2}+\mu\frac{\partial}{\partial x_3}\bigtriangledown^2 u_3+\rho\frac{\partial}{\partial x_3}b_3\right]=\\
&\rho\frac{\partial}{\partial x_1}\left(\frac{\partial^2 u_1}{\partial t^2}\right)+\rho\frac{\partial}{\partial x_2}\left(\frac{\partial^2 u_2}{\partial t^2}\right)+\rho\frac{\partial}{\partial x_3}\left(\frac{\partial^2 u_3}{\partial t^2}\right).
\end{aligned} \tag{2.9}$$

Recognizing that the right hand side of Equation (2.9) can be rewritten as

$$\begin{aligned}
&\rho\frac{\partial}{\partial x_1}\left(\frac{\partial^2 u_1}{\partial t^2}\right)+\rho\frac{\partial}{\partial x_2}\left(\frac{\partial^2 u_2}{\partial t^2}\right)+\rho\frac{\partial}{\partial x_3}\left(\frac{\partial^2 u_3}{\partial t^2}\right)=\\
&\rho\frac{\partial^2}{\partial t^2}\left(\frac{\partial u_1}{\partial x_1}+\frac{\partial u_2}{\partial x_2}+\frac{\partial u_3}{\partial x_3}\right)=\rho\frac{\partial^2\epsilon_{kk}}{\partial t^2},
\end{aligned}$$

it is evident that Equation (2.9) can be stated as

$$\begin{aligned}
&\left[(\lambda+\mu)\frac{\partial^2\triangle}{\partial {x_1}^2}+\mu\bigtriangledown^2\epsilon_{11}+\rho\frac{\partial}{\partial x_1}b_1\right]+\\
&\left[(\lambda+\mu)\frac{\partial^2\triangle}{\partial {x_2}^2}+\mu\bigtriangledown^2\epsilon_{22}+\rho\frac{\partial}{\partial x_2}b_2\right]+\\
&\left[(\lambda+\mu)\frac{\partial^2\triangle}{\partial {x_3}^2}+\mu\bigtriangledown^2\epsilon_{33}+\rho\frac{\partial}{\partial x_3}b_3\right]=\\
&\rho\frac{\partial^2}{\partial t^2}(\epsilon_{11}+\epsilon_{22}+\epsilon_{33}).
\end{aligned} \tag{2.10}$$

This can be rearranged to get:

$$\begin{aligned}
&(\lambda+\mu)\left(\frac{\partial^2\triangle}{\partial {x_1}^2}+\frac{\partial^2\triangle}{\partial {x_2}^2}+\frac{\partial^2\triangle}{\partial {x_3}^2}\right)+\\
&\mu\bigtriangledown^2(\epsilon_{11}+\epsilon_{22}+\epsilon_{33})+\rho\left(\frac{\partial}{\partial x_1}b_1+\frac{\partial}{\partial x_2}b_2+\frac{\partial}{\partial x_3}b_3\right)=\\
&\rho\frac{\partial^2}{\partial t^2}(\epsilon_{11}+\epsilon_{22}+\epsilon_{33}).
\end{aligned} \tag{2.11}$$

Finally, assuming there are no body forces ($b_i = 0$), then Equation (2.11) reduces to the wave (or hyperbolic) equation for a dilatation $\triangle$:

$$(\lambda+2\mu)\bigtriangledown^2\triangle=\rho\frac{\partial^2\triangle}{\partial t^2}. \tag{2.12}$$

The three-dimensional wave equation for an unbounded medium can easily be derived from the Navier equation of motion (2.12) by rearranging the terms

$$\frac{\partial^2 \triangle}{\partial t^2} = \frac{(\lambda + 2\mu)}{\rho} \nabla^2 \triangle, \tag{2.13}$$

where $(\lambda + 2\mu)/\rho = C_L^2$ and C_L is the longitudinal (or dilatational) wave speed. The shear wave speed can be derived using a similar approach [196]. However, in order to derive the shear wave speed, Equations (2.6) and (2.7) are differentiated with respect to x_2 and x_1, respectively. Ignoring the body forces, the solution becomes

$$\rho \frac{\partial^2 \omega}{\partial t^2} = \mu \nabla^2 \omega, \tag{2.14}$$

where ω is the rigid body rotation, $\mu/\rho = C_S^2$ and C_S is the shear (or equivoluminal) wave speed.

The wave equation can be solved either by the method due to Cauchy and Fourier or that due to D'Alembert. The Cauchy and Fourier method requires the separation of the partial differential equation into ordinary differential equations then obtaining solutions to the ordinary differential equations through power series while the D'Alembert method requires the method of characteristics. The D'Alembert solution is quite often employed to solve the wave equation and is stated as:

$$u = f(\xi) + g(\zeta), \tag{2.15}$$

where $f(\xi)$ and $g(\zeta)$ are arbitrary functions which are twice differentiable. The D'Alembert solution is a representation of the displacement u as the sum of two arbitrary functions $f(\xi)$ and $g(\zeta)$. Descriptions of the method of characteristics are found in references [196], [200], and [204–208].

2.2 SHOCK WAVES IN CONDENSED MEDIA

A shock wave (here after referred to as a shock) in condensed matter, as defined in Chapter 1, is a large amplitude nonlinear wave propagating at supersonic velocity relative to the unshocked material ahead of it but subsonic relative to the shocked material behind it. Across the boundary of the shocked and unshocked material, there exist a near-discontinuity or jump in principal mechanical and thermodynamic parameters such as particle velocity (or stress), strain, density, temperature, volume, etc. [109, 196, 200, 204, 209–212]. The intent of this section is to briefly introduce the concept of a shock propagating in condensed matter and state or derive the pertinent equations used in its analysis.

2.2.1 SHOCK FORMATION

The formation of a shock is easily explained using the schematic representation of a propagating disturbance in a condensed medium shown in Figure 2.1. When a solid material is disturbed, the velocity with which the disturbance travels is the sum of the adiabatic sound speed,

$c\left(=V\left(-\partial\sigma/\partial V\right)_s^{1/2}\right)$ and the particle velocity (u_p), where σ, V, and S are stress, volume, and entropy, respectively. The velocity of the disturbance increases with stress and therefore, the particles designated by A, B, and C in Figure 2.1 will move from left to right with respect to their surroundings at the local sound speed of c_A, c_B, and c_C, respectively. Since the local sound speed and particle velocity increase with stress, then $V_C > V_B > V_A$. Therefore, as the distance traveled by the shock increases, the velocity at points B and C will eventually catch up with that of point A resulting in a jump or discontinuity in stress. The resulting shock is nonlinear and, therefore, superposition of solutions is no longer valid. It is noteworthy to point out that real shock profiles are not a true discontinuity. However, for most materials, the magnitude of the shock rise time is in the order of nanoseconds. As the strain rate increases, dissipative mechanisms such as viscosity and heat transport become active and tend to smear out the wave front [213]. At high strain rates, the dissipative forces become more pronounced and start to cancel out the effect of increasing sound speed with stress. Eventually, as the opposing effects cancel one another, the profile of the wave no longer evolves with time and therefore, the shock becomes steady [213].

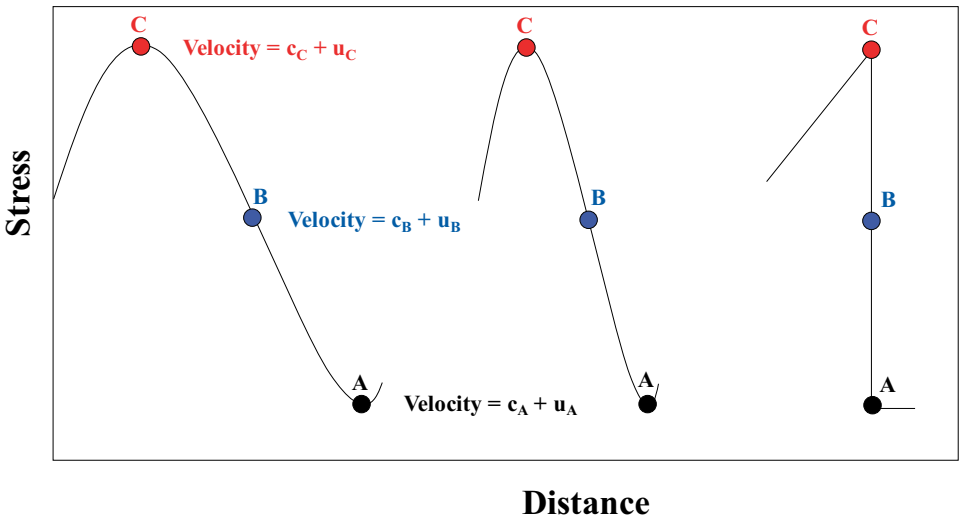

Figure 2.1: An illustration of stress as a function of distance of a disturbance propagating from left to right in a condensed medium (shocking up).

2.2.2 SHOCK STABILITY

In general, shocks do not always develop when a transient load is applied to a condensed medium such as the case for the vast majority of uniaxial stress loading (Kolsky bar experiments). However, once developed, they may or may not be stable, and if they become unstable, the shock will break up. Consider the schematic in Figure 2.2 of a shock front moving in a solid body and

suppose it is moving from left to right. If an observer moves with the shock front (shock coor-

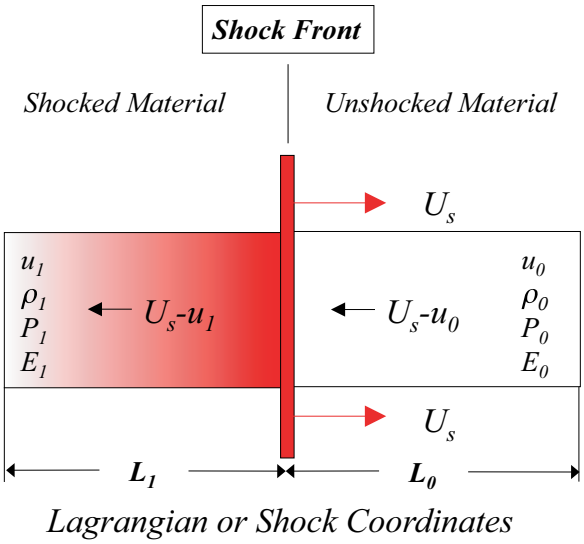

Figure 2.2: An illustration of a shock front moving in a condensed medium from left to right.

dinates), then he/she will observe the material approaching the shock front with a velocity U_s (assuming $u_0 = 0$, the material ahead of the shock front is at rest) and leaving the shock front with a velocity $U_s - u_1$, where U_s, u_0, and u_1 are the shock velocity, particle velocity ahead of the shock, and particle velocity behind the shock, respectively. If $U_s > u_1 + c$, then the disturbance behind the shock front would not be able to catch up with the shock front and therefore, the shock would become unstable and decay. On the other hand, if a small compressive disturbance is ahead of the shock, it must move slower than the shock front or else, the small compressive disturbance will out run the shock and become unsteady. Considering both cases, the following criteria must be satisfied for shock stability in normal materials [213]:

$$\frac{dc}{d\sigma} > 0 \quad \text{(sound speed increases with stress)} \tag{2.16}$$

$$c + u_p \geq U_s \quad \text{(shock wave is subsonic w.r.t. shock state)} \tag{2.17}$$

$$U_s > c_0 \quad \text{(shock wave is supersonic w.r.t. unshock state),} \tag{2.18}$$

where U_s is the shock velocity, and c and c_0 are the sound speed at the shock state and initial state, respectively. Note that σ is positive in compression. Some materials such as distended materials do not satisfy the stability criteria listed above; however, their treatment is beyond the scope of this book.

2.2.3 RAREFACTION WAVES

A material cannot remain in the shocked state indefinitely and after some finite time will unload to ambient conditions. The same property responsible for shocking up compression waves in condensed matter (i.e., the increase in sound speed with increase in compressive stress) is responsible for unloading the material. A rarefaction wave is a mechanism by which a disturbance propagates into the shocked material and lowers the stress to that of ambient conditions. Rarefaction waves are sometimes referred to as unloading waves, expansion waves, decompression waves, or release waves. In general, rarefaction waves do not propagate as discontinuities although their existence have been reported in the open literature [214–216]. They are analyzed differently than shock waves and their analysis is beyond the scope of this book.

The rarefaction process can be easily described using Figures 2.3 and 2.4. Shown in Figure 2.3 is a reflected square shock profile (frame 1) from a free surface and it is propagating from left to right with a velocity of U_s at a steady shock stress. Similar to the case of shock formation, the velocity at points B and C is traveling faster than point A ($V_C > V_B > V_A$) due to their differences in stress. However, the shock front which is subjected to the stability criteria travels with a constant velocity, U_s. Therefore, the point C will eventually catch up with the shock front resulting in the spreading of the wave at the backend of the square shock profile as shown in frames 2–4 in Figure 2.3. This spreading or diverging of the waves is traditionally referred to as a rarefaction fan and the concept is shown in the Lagrangian (X-t) diagram (Figure 2.4). As shown in the figure, the head of the rarefaction travels faster than the tail. With further increase in time, the square shock profile becomes a saw tooth wave (frames 3 and 4). At this point, the rarefaction wave begins to attenuate the shock and eventually, the wave is no longer a shock (frame 5) but just a stress wave without a discontinuity.

2.2.4 RANKINE–HUGONIOT JUMP RELATIONS

The mathematical treatment of shocks was first developed by Rankine [217] and later refined by Hugoniot [218]. Rankine showed that there was no steady adiabatic process in which pressure forces alone could describe the changes from one constant state to another by a continuous change. Rankine then proposed that the process be adiabatic globally but locally heat could be exchanged. Hugoniot later described the relationship of energy and entropy involved in continuous and discontinuous flow. He was the first to show that ideal continuous flow implies conservation of entropy and that an increase in entropy must occur across a shock front. Figure 2.5 shows a picture of (*a*) the Scottish engineer and physicist William John Rankine (1820–1872) and (*b*) the French engineer and physicist Pierre Henri Hugoniot (1851–1887). The intent of this section is to derive the Rankine–Hugoniot jump relations and use them to analyze the shock process from a mathematical point of view.

Consider a planar shock traveling from left to right in a condensed medium, as shown in Figure 2.2 with a velocity U_s. Ahead of the shock front, the particles in the condensed medium have zero velocity ($u_0 = 0$), since it has not been disturbed. Note that the shock coordinate

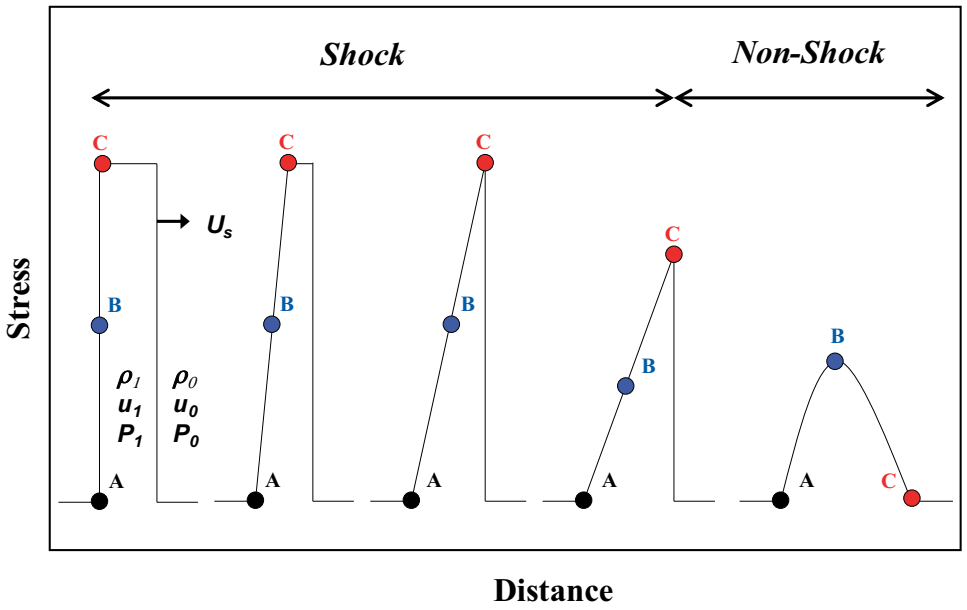

Figure 2.3: An illustration of a Stress-Distance plot of a decaying disturbance (spreading of a rarefaction wave).

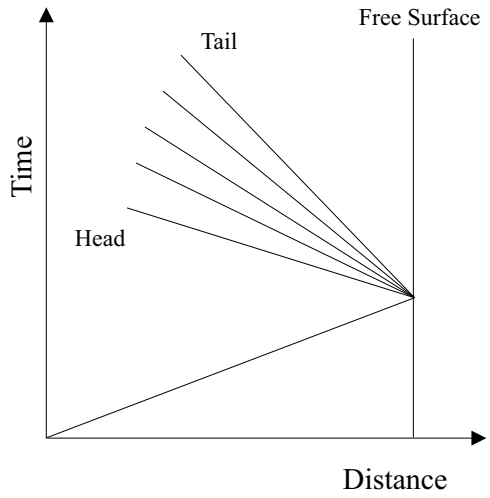

Figure 2.4: A Lagrangian (X-t) diagram of a shock wave reflected from a free surface as a rarefaction wave.

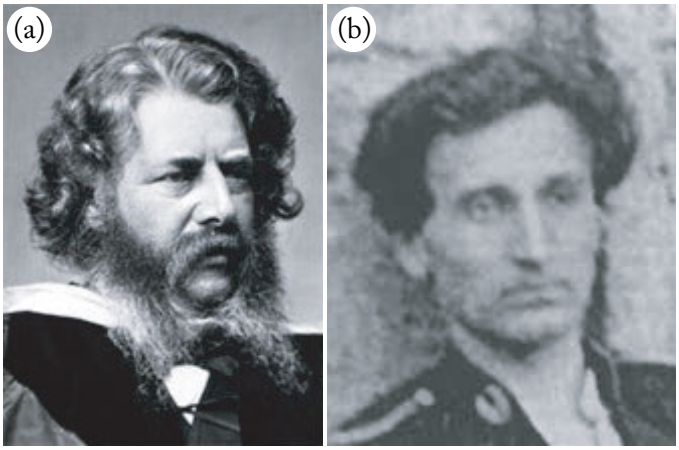

Figure 2.5: (a) The Scottish engineer and physicist William John Rankine (1820–1872) and (b) the French engineer and physicist Pierre Henri Hugoniot (1851–1887).

system is Lagrangian. If one considers a particle in front of the shock front, it will approach the shock front with a relative velocity equal to $(U_s - u_0)$. On the other hand, a particle behind the shock front will move away with a relative velocity $(U_s - u_1)$. With this in mind, the conservation of mass is applied. The mass entering the shock front must be equal to the mass exiting the shock front. The mass entering the shock front is

$$A\rho_0 \left(U_s - u_0\right) dt \tag{2.19}$$

and the mass exiting the shock front is

$$A\rho_1 \left(U_s - u_1\right) dt. \tag{2.20}$$

Therefore,

$$A\rho_0 U_s dt = A\rho_1 \left(U_s - u_1\right) dt \tag{2.21}$$

since u_0 is zero in most cases except for the reshock case and A is the cross-sectional area of the control mass. The equation for the conservation of mass can be easily obtained from Equation (2.21) and is

$$\rho_0 U_s = \rho_1 \left(U_s - u_1\right). \tag{2.22}$$

The conservation of linear momentum requires that the time rate of change of momentum for the control mass to go from the unshocked state in front of the shock front to the shocked state behind the shock front must be equal to the applied force. Therefore, the difference in the time rate of change of momentum is

$$\triangle M' = \rho_1 A \left(U_s - u_1\right) u_1 \tag{2.23}$$

since u_0 is zero (the time rate of change of momentum of the unshocked state (0) is zero) and $\triangle M' = M_1' - M_0'$ is the difference in the time rate of change of momentum between state 1 and state 0. The applied force is

$$F = A(\sigma_1 - \sigma_0), \tag{2.24}$$

where σ_1 and σ_0 are the shock stresses behind and ahead of the shock front, respectively. Equating the time rate of change of momentum (2.23) and applied force (2.24) we get

$$A(\sigma_1 - \sigma_0) = \rho_1 A\,(U_s - u_1)\,u_1. \tag{2.25}$$

Recognizing that $\rho_0 U_s = \rho_1(U_s - u_1)$ from the conservation of mass equation ((2.21)) and substituting into Equation (2.25), the equation of conservation of momentum can be stated as

$$(\sigma_1 - \sigma_0) = \rho_0 U_s u_1. \tag{2.26}$$

The product of the density and shock velocity ($\rho_0 U_s$) is traditionally referred to as the shock impedance.

The conservation of energy states that the rate of energy increase of the control mass is equal to the rate of work being done on it. Therefore, the rate at which work is done on the control mass is

$$\frac{dW}{dt} = A(\sigma_1 u_1 - \sigma_0 u_0). \tag{2.27}$$

The difference in total energy (kinetic plus internal) between the unshocked state (0) and shocked state (1) is

$$E_T = (K_1 - K_0) + (E_1 - E_0), \tag{2.28}$$

where K_1 and K_0 are the change in kinetic energy of the shock state (1) and the unshocked state (0), respectively. Similarly, E_1 and E_0 are the change in the internal energy of the shock state (1) and the unshocked state (0), respectively. Therefore,

$$(K_1 - K_0) = \frac{1}{2}\left[\rho_1 A(U_s - u_1)u_1^2\right] - \frac{1}{2}\left[\rho_0 A(U_s - u_0)u_0^2\right]. \tag{2.29}$$

Recalling that u_0 is zero, Equation (2.29) can be restated as

$$(K_1 - K_0) = \frac{1}{2}\left[\rho_1 A(U_s - u_1)u_1^2\right]. \tag{2.30}$$

Also,

$$(E_1 - E_0) = \rho_1 A e_1(U_s - u_1) - \rho_0 A e_0(U_s - u_0), \tag{2.31}$$

where e_1 and e_0 are the change of the specific internal energy of the shock state (1) and the unshocked state (0), respectively. Combining Equations (2.27) and (2.28), then substituting for $(K_1 - K_0)$ and $(E_1 - E_0)$ using Equations (2.30) and (2.31), respectively, plus setting u_0 to zero gives

$$\sigma_1 A u_1 = \frac{1}{2}\left[\rho_1 A(U_s - u_1)u_1^2\right] + \rho_1 A e_1\,(U_s - u_1) - \rho_0 A e_0 U_s. \tag{2.32}$$

But $\rho_0 U_s = \rho_1 (U_s - u_1)$ from the equation of conservation of mass (2.21), therefore, Equation (2.32) can be simplified and rearranged to get

$$\sigma_1 u_1 = \frac{1}{2}\rho_0 U_s u_1^2 + \rho_0 U_s (e_1 - e_0). \tag{2.33}$$

With further simplification, Equation (2.33) can be arranged into a common form as

$$e_1 - e_0 = \frac{\sigma_1 u_1}{\rho_0 U_s} - \frac{1}{2}\rho_0 \frac{U_s u_1^2}{\rho_0 U_s}. \tag{2.34}$$

But from the conservation of momentum, $u_1 = (\sigma_1 - \sigma_0)/\rho_0 U_s$, therefore, substituting for u_1 in the above equation gives

$$e_1 - e_0 = \frac{\sigma_1 (\sigma_1 - \sigma_0)}{\rho_0^2 U_s^2} - \frac{1}{2}\frac{(\sigma_1 - \sigma_0)^2}{\rho_0^2 U_s^2}. \tag{2.35}$$

Invoking $\rho_0 U_s = \rho_1 (U_s - u_1)$ from the conservation of mass and using Equation (2.26) the following can be obtained:

$$\rho_0 U_s^2 = -\rho_1 (\sigma_1 - \sigma_0) \frac{1}{\rho_0 - \rho_1}, \tag{2.36}$$

and recognizing that $1/\rho = V$ the following is achieved

$$\rho_0^2 U_s^2 = \frac{(\sigma_1 - \sigma_0)}{V_0 - V_1}. \tag{2.37}$$

Substituting Equation (2.37) into Equation (2.35) and solving gives

$$e_1 - e_0 = \frac{1}{2}(\sigma_1 + \sigma_0)(V_0 - V_1). \tag{2.38}$$

Equations (2.39), (2.40), and (2.41) are the conservation equations known as the **Rankine–Hugoniot jump relations**:

$$\rho_0 U_s = \rho_1 (U_s - u_1) \tag{2.39}$$

$$(\sigma_1 - \sigma_0) = \rho_0 U_s u_1 \tag{2.40}$$

$$(e_1 - e_0) = \frac{1}{2}(\sigma_1 + \sigma_0)(V_0 - V_1). \tag{2.41}$$

The Rankine–Hugoniot jump relations are often referred to as jump conditions because the initial values of the state in front of the shock jumps to the final state behind the shock as the shock front passes by. The jump conditions are particularly useful in the form stated in

Equations (2.39)–(2.41). For shock compressed solids (excluding the shock-reshock or double-shock problem), the shock stress is normally far greater than the ambient stress which is usually ambient atmospheric pressure. Also, E_0 is also taken to be zero because the internal energy is a thermodynamic state function and can be referenced to any initial state. Taking the previous two statements into account, the jump conditions can be written in their simplest and common form

$$\frac{\rho_0}{\rho_1} = \left(1 - \frac{u_1}{U_s}\right) \tag{2.42}$$

$$\sigma_1 = \rho_0 U_s u_1 \tag{2.43}$$

$$e_1 = \frac{1}{2}\sigma_1 \left(V_0 - V_1\right). \tag{2.44}$$

In the above equations, only five variables are present: stress (σ), density (ρ) or volume (V), particle velocity (u_p), shock velocity (U_s), and specific internal energy (e). This is an ill-posed problem, because to solve for the five variables, five equations are needed. The first four equations required come from the jump conditions plus the equation of state which will be discussed next in this section. Therefore, there is only one independent variable remaining and it is prescribed from experiments. These experiments are usually referred to as the Rankine–Hugoniot experiments or simply Hugoniot experiments and they can be represented in any two-dimensional plane. The three most useful are pressure-volume ($P - v$ or $\sigma - v$) Hugoniot where $v = V/V_0$ is the specific volume, pressure-particle velocity ($P - u_p$ or $\sigma - u_p$) Hugoniot, and shock velocity-particle velocity ($U_s - u_p$) Hugoniot. The stress-specific volume, stress-particle velocity, and shock velocity-particle velocity Hugoniots for selected materials with FCC, BCC, and HCP lattice structures shock compressed to 40 GPa are shown in Figures 2.6, 2.7, and 2.8, respectively. Pressure (P) and stress (σ) are sometimes used interchangeably in shock wave research and must not be confused by their distinct difference in solid mechanics. It is important to note that the $P - v$ or $\sigma - v$ Hugoniot is not the path followed during shock compression but it is rather a collection of loci of all possible end states achieved during shock compression of a material at a given initial state. The path followed by a steady shock during compression is the Rayliegh line connecting the initial state and the end state [163, 210, 219] and will be discussed later in this section.

It is useful to compare shock compression to isentropic and isothermal compression. Figure 2.9 is a $P - V$ plane of a representative material and it is assumed here that the material has not undergone any polymorphic or allotropic phase transformation in the solid state. The curves shown in the figure are projections from a $P - V - E$ or $P - V - T$ Equation of State (EOS) surface into the $P - V$ plane. In the interest of space, only the Hugoniot (red), isentrope (green), release isentrope (dashed green), isotherm (cyan) curves, and Rayliegh line (dashed red) will be discussed. As pointed out in the previous section, the Hugoniot or shock adiabat is a collection of loci of all possible end states achieved during the shock compression of a material at a

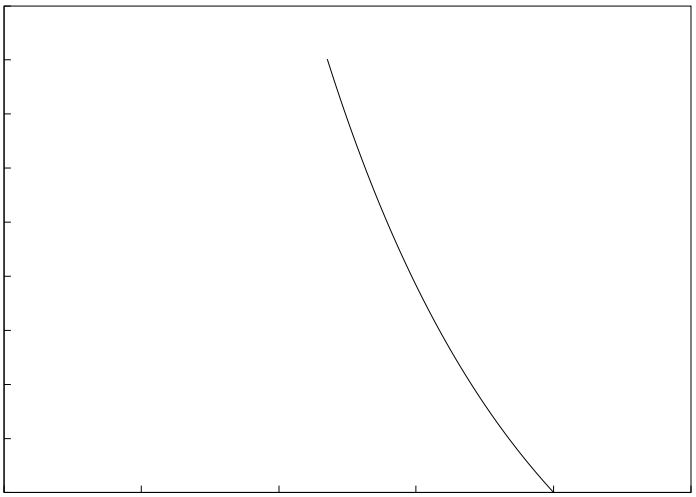

Figure 2.6: Stress vs. specific volume ($\sigma - v$ or $P - v$) Hugoniot for selected metals with FCC, BCC, and HCP lattice structures shock compressed to 40 GPa.

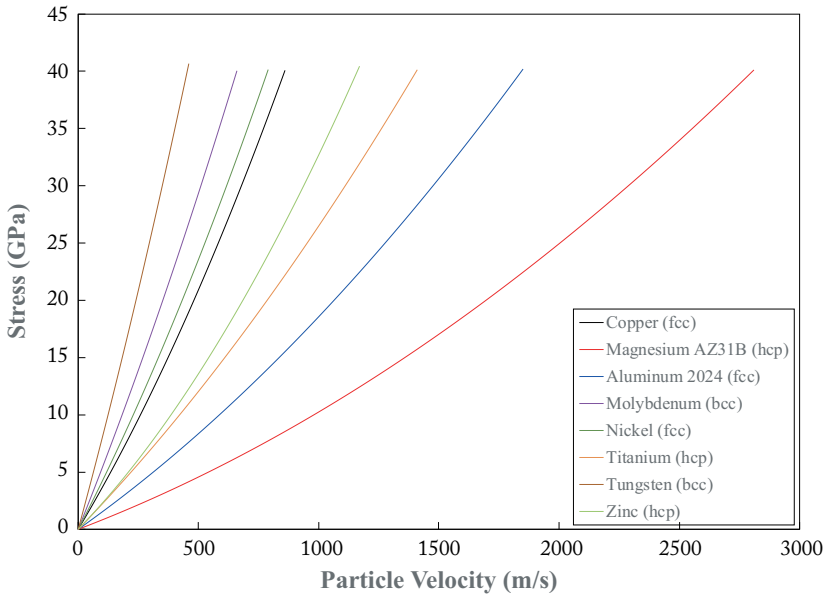

Figure 2.7: Stress vs. particle velocity ($\sigma - u_p$ or $P - u_p$) Hugoniot for selected metals with FCC, BCC, and HCP lattice structures shock compressed to 40 GPa.

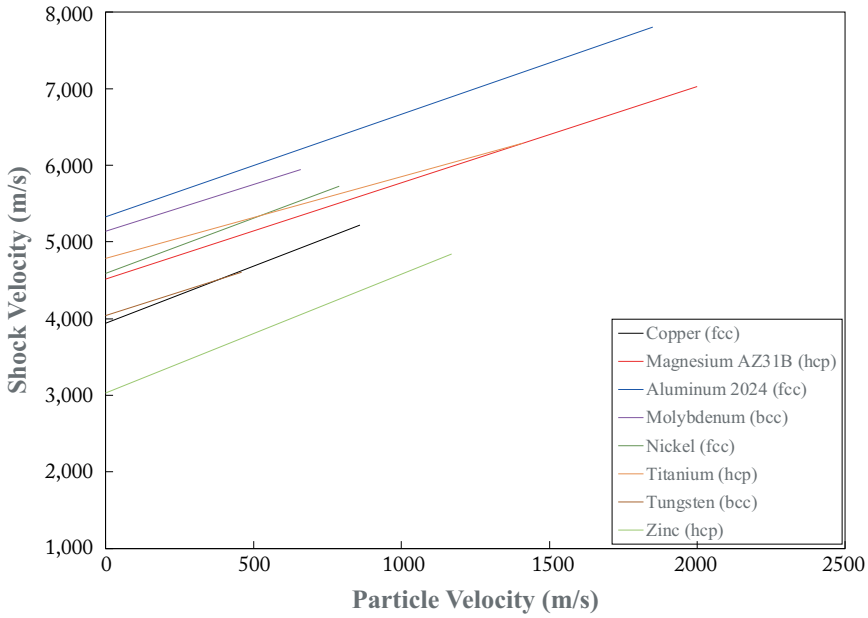

Figure 2.8: Shock velocity vs. particle velocity ($U_s - u_p$) Hugoniot for selected metals with FCC, BCC, and HCP lattice structures shock compressed to 40 GPa.

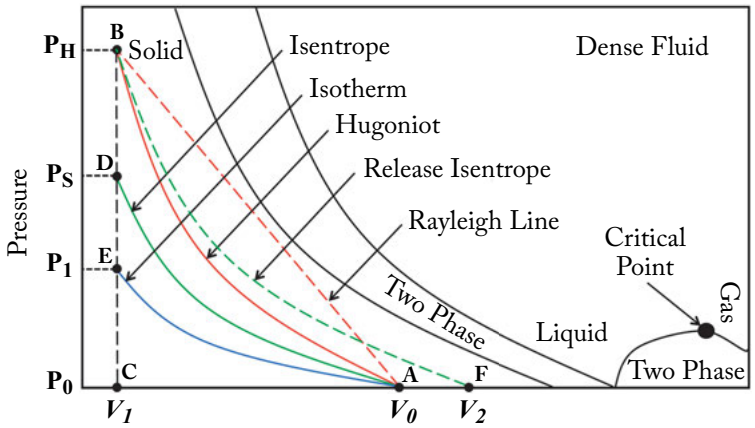

Figure 2.9: The P-V plane for a representative material.

given initial state and it is not the path followed during the shock compression of a condensed material. The Hugoniot curve is adiabatic, that is, during shock compression, the heat exchange between the system and its surroundings in going from state A to state B is zero (see Figure 2.9). Unlike the Hugoniot curve, the isentrope and the isotherm both represent a collection of loci of all states that can be realized continuously. The primary difference in practice between the Hugoniot and both the isentrope and isotherm is that, developing a Hugoniot involves a series of experiments whilst the isentropic and isothermal curves can be obtained from a single experiment (Z-Accelerator for isentropic or shockless compression and Diamond Anvil Cell (DAC) for isothermal compression).

When a solid body is shock compressed from an initial volume, V_0 (point A) to a volume, V_1 (point B), the process path from A to B is along the Rayleigh line not the Hugoniot (see Figure 2.9). Therefore, the energy required to achieve such compression is the area ABC under the Rayleigh line. The area ABC enclosed by the Rayleigh line is always greater than the area enclosed by the Hugoniot or else the shock will not be steady or stable. The energy required to compress the solid body from point A to point B is calculated using Equation (2.45), where P_H, P_0, V_0, and V_1 are the Hugoniot pressure or stress, ambient pressure or stress, initial volume, and compressed volume, respectively:

$$\triangle E_H = \frac{1}{2}\left(P_H + P_0\right)\left(V_0 - V_1\right). \tag{2.45}$$

After the passage of the shock wave, the solid body is then released back to ambient pressure along the path BF (release isentrope). The release of the solid body from the shock state to ambient pressure is isentropic as shown in Figure 2.9. The volume, V_2, at the release state (point F) is greater than the initial volume, V_1 (point A). This is due to thermal expansion, which is a consequence of temperature rise in the solid body from the passage of the shock and plastic work. However, the material reverts back to the original volume after cooling back to ambient conditions. For weak to moderate shock stresses, the release isentrope BF and the Hugoniot AB are traditionally assumed to be approximately the same. When this assumption holds true, the area enclosed between the Hugoniot and the Rayleigh line represents the residual energy or waste heat and it is associated with the irreversible process of shock compressing a solid body. Similarly, the path followed during isentropic compression of a material from its initial volume, V_0 to a compressed volume, V_1 (point D) can be represented by the area ADC. The energy required to compress the material from point A to point D (isentropically) can be calculated using the following equation:

$$\triangle E_s = -\int_{V_0}^{V} P\, dV_s, \tag{2.46}$$

where S is the entropy. Note that in Figure 2.9, the isentrope is lower than the shock adiabat or Hugoniot. This is always the case since the rate at which pressure changes with respect to energy at constant volume is always greater than zero, i.e., $((\partial P/\partial E)_V > 0)$.

Furthermore, when a material is isothermally compressed from its initial volume V_0 to a volume V_1, the path followed is AE, as shown in Figure 2.9. The energy required for an isothermal compression from point A to E is the least for all three processes and it is represented by an area which is less than the area AEC by the term $\int_{V_0}^{V} T\left(\frac{\partial P}{\partial T}\right)_V dV_T$. Therefore, the energy required for isothermal compression can be computed using Equation (2.47). From Figure 2.9, it can be deduced that the increase in energy going from the isothermal process to the Hugoniot process is followed by a progressive increase in temperature:

$$\triangle E_I = -\int_{S_0}^{S} T dS_T - \int_{V_0}^{V} P dV_T = \int_{V_0}^{V} T\left(\frac{\partial P}{\partial T}\right)_V dV_T - \int_{V_0}^{V} P dV_T. \tag{2.47}$$

The Rankine–Hugoniot relationships are fundamental in shock wave research for experimental design, EOS development, and shock wave data interpretation.

2.3 EQUATION OF STATE

The Rankine–Hugoniot jump conditions stated in Equations (2.39)–(2.41) describe the relationship between the thermodynamic equilibrium states in front and behind a shock wave in one-dimensional deformation of solids. However, an EOS is generally required to determine a complete thermodynamic description of a material response at high pressure states using existing experimental data. The EOS describes the pressure of a material as a function of density and temperature; it is required to solve the continuity, momentum, and energy equations, which govern the thermodynamic transition of a material from the unshocked state to the shocked state. In this book, the discussion of the EOS used in hydrocodes for plate impact problems is limited to the Mie–Grüneisen EOS because it is the most common EOS used for such problems.

In order to completely describe the volumetric response of a material under shock loading conditions, the values of the thermodynamic state variables are required at every state of the material. Thermodynamic state variables such as pressure, temperature, specific volume, internal energy, entropy, and enthalpy are properties which are only dependent on the state of a material, not the path taken to get to those states. Therefore, to completely describe the state of a material which has not undergone phase changes, knowledge of the material's pressure as a function of density and temperature is sufficient if there is no strength.

Generally, thermodynamic state data are represented in three forms. First, they can be tabulated from experimental data over a large range of states for which interpolation becomes necessary to obtain data in between state points. Second, thermodynamic state data can be compiled in a graphical form from which state variables can be accurately and promptly extracted

if the thermodynamic process is known. The tabulated and graphical forms require extensive experimental testing in order to develop the required data. Third, the most common way to represent thermodynamic state data is in analytical form and is often referred to as an equation of state. The primary advantage of the analytical form is its compactness which makes it easy to transform into computer codes. Also, it provides a more fundamental understanding of the thermodynamic process because of the mathematical relationships between state variables. However, because equations of states are formulated based on intrinsic assumptions about the response of materials, they are prone to errors. For instance, assuming constant specific heats may only be valid over a small range of possible states.

All equations of state require experimental data in order to be functional. The Mie-Grüneisen EOS which is most commonly used for plate impact problems, thermodynamic state variables are expressed relative to states experimentally determined from the pressure-volume (Hugoniot) curve. The EOS is required to solve the continuity, momentum, and energy equations. In shock compression problems, the thermodynamic state change is adiabatic and under such conditions the energy equation need not explicitly contain temperature. Therefore, the governing equations may be solved if either the internal energy or the entropy is known as a function of pressure and density. The Mie-Grüneisen EOS relates the internal energy (not the temperature) to pressure and density. It provides the framework from which the states can be tied back to an arbitrary reference function [212, 220–222] and it is generally stated as

$$P = \rho^2 \frac{dU}{d\rho} + \Gamma\rho\,(E - U)\,, \tag{2.48}$$

where P is pressure, U is the specific interatomic potential energy (a function of density only), E is the specific internal energy, Γ is the Gruneisen gamma (a function of density only), and ρ is the density of the material, respectively. Note that the terms $\rho^2 dU/d\rho$ and $(E - U)$ represent the "cold pressure" and the specific vibrational internal energy, respectively. The "cold pressure" is the compression pressure at absolute zero, in the absence of specific vibrational internal energy.

For a known or assumed "cold pressure" and known thermodynamic states along the reference Hugoniot, then the Gruneisen gamma may be inferred as a direct function of density. However, if the thermodynamic states are known only along the "non-cold" reference curve and if a functional relationship is assumed for the Gruneisen gamma, then the interatomic potential function may be implicitly removed by referencing the thermodynamic state at any point (P, ρ, E). This is achieved by taking the difference of the Mie-Grüneisen EOS at two states and this approach is what is universally adopted for hydrocodes. This approach reduces Equation (2.48) to

$$P - P_{ref} = \Gamma\rho\left(E - E_{ref}\right). \tag{2.49}$$

Furthermore, if the reference function is chosen as the Hugoniot, then the Mie-Grüneisen EOS becomes

$$P - P_H = \Gamma\rho\,(E - E_H)\,, \tag{2.50}$$

where P_H and E_H are the pressure and specific internal energy at the reference Hugoniot state. The Gruneisen gamma can be expressed by restating Equation (2.50) as $dP = (\Gamma/V)dE$, where $\rho = 1/V$ and since V is a constant, Γ is equivalent to

$$\Gamma = V\left(\frac{\partial P}{\partial E}\right)_V = V\left(\frac{\partial P}{\partial T}\right)_V\left(\frac{\partial T}{\partial E}\right)_V \tag{2.51}$$

or

$$\Gamma = \frac{V}{C_v}\left(\frac{\partial P}{\partial T}\right)_V = -\frac{V}{C_v}\left(\frac{\partial P}{\partial V}\right)_T\left(\frac{\partial V}{\partial T}\right)_P \tag{2.52}$$

since $(\partial P/\partial T)_V = -(\partial P/\partial V)_T\,(\partial V/\partial T)_P$. From Equations (2.51) and (2.52), T and C_v are the temperature and specific heat at constant volume, respectively. For detailed descriptions of the Mie-Grüneisen EOS, the reader is encouraged to review the following references [219, 222–227].

2.4 ELASTIC-PLASTIC MATERIAL RESPONSE

Plate impact experiments are traditionally used to study shock wave propagation in condensed matter. Unlike Kolsky bar experiments, which impose a state of uniaxial stress in the material being studied, plate impact experiments impose a state of uniaxial strain. That is, there is only one non-zero component of strain or displacement in the strain tensor and it is in the direction of the shock wave. However, the stress state is three-dimensional because of the effective lateral constraints. With the plate impact configuration, hydrodynamic considerations become very important with increasing impact velocity or stress. In general, both the hydrostatic (pressure) and deviatoric (shear stress) parts of the stress and strain tensors are involved. However, at extremely high shock stresses (overdriven) when the phase of the material approaches liquidus, shear stresses are much smaller than pressure and can be neglected. One of the earliest theoretical analyses of an elastic-plastic material undergoing shock compression was conducted by Morland [228]. However, other researchers [196, 211, 212, 229–234] have also analyzed uniaxial strain problems in depth. Although a good amount of basic understanding of the shock response of elastic-plastic materials has been developed, there are still more underlying questions on the structure-property relationships. Therefore, the intent of this section is to provide a concise theoretical background for understanding and interpreting of shock wave data.

Suppose the half space of an elastic-plastic material initially at rest is subjected to a sudden compression pulse in the direction designated 1, as shown in Figure 2.10. If the resulting stresses do not exceed the dynamic yield stress, the material response will be elastic and a single elastic wave is generated. However, if the resulting stresses are greater than the dynamic yield stress (Hugoniot Elastic Limit, HEL in this case); a two-wave structure will be generated. From the wave profile shown in Figure 2.10, a faster elastic wave (denoted by E) usually referred to as the elastic precusor will lead a slower plastic wave (denoted by P).

If a small volume element is considered within the half space, a state of uniaxial strain will exist in the direction 1, while the lateral edges are constrained (i.e., $\epsilon_{11} \neq 0$ and $\epsilon_{22} = \epsilon_{33} =$

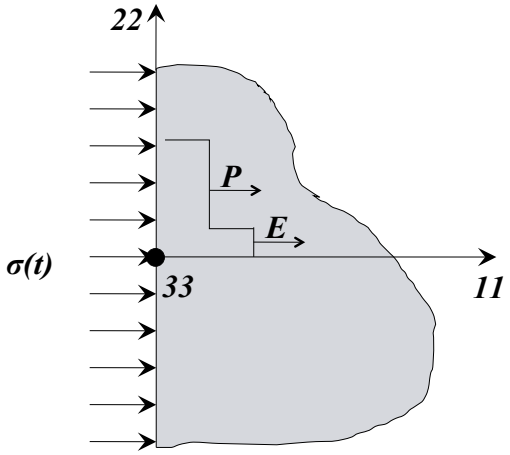

Figure 2.10: The half space of an elastic-plastic material subjected to a sudden compression.

$\epsilon_{12} = \epsilon_{13} = \epsilon_{23} = 0$). However, the state of stress is not uniaxial and can be represented by the stress tensor σ_{ij} as

$$\sigma_{ij} = \begin{bmatrix} \sigma_{11} & 0 & 0 \\ 0 & \sigma_{22} & 0 \\ 0 & 0 & \sigma_{33} \end{bmatrix}. \tag{2.53}$$

The components of stress, σ_{11} and $\sigma_{22} = \sigma_{33}$ are normal to the surface elements on which they are applied and are normal stresses.

Furthermore, the stress tensor σ_{ij} can be broken up into the hydrostatic part which is responsible for volume change and the deviatoric part which is responsible for shape change. Therefore, the stress tensor σ_{ij} can be restated as

$$\sigma_{ij} = S_{ij} + \sigma\delta_{ij}, \tag{2.54}$$

where $\sigma = \left(\frac{1}{3}\right)\sigma_{kk}$ is the mean normal stress, $\sigma_{kk} = \sigma_{11} + \sigma_{22} + \sigma_{33}$, and δ_{ij} is Kronecker delta. But from symmetry $\sigma_{22} = \sigma_{33}$, which implies that $\sigma = \frac{1}{3}(\sigma_{11} + 2\sigma_{22})$. The deviatoric stress tensor can now be defined as the difference between the stress tensor σ_{ij} and the mean normal stress σ as:

$$S_{ij} = \sigma_{ij} - \sigma\delta_{ij}. \tag{2.55}$$

The deviatoric tensor then becomes

$$S_{ij} = \begin{bmatrix} \frac{2}{3}(\sigma_{11} - \sigma_{22}) & 0 & 0 \\ 0 & -\frac{1}{3}(\sigma_{11} - \sigma_{22}) & 0 \\ 0 & 0 & -\frac{1}{3}(\sigma_{11} - \sigma_{22}) \end{bmatrix}. \tag{2.56}$$

The first, second, and third invariants of the deviator stress tensor are

$$I_S = 0 \tag{2.57}$$

$$II_S = \frac{1}{3}(\sigma_{11} - \sigma_{22})^2 \tag{2.58}$$

$$III_S = \frac{2}{27}(\sigma_{11} - \sigma_{22})^3 . \tag{2.59}$$

The maximum value of the shear stress and the mean normal stress are stated in Equations (2.60) and (2.61), respectively:

$$\tau_{max} = \frac{1}{2}|\sigma_{11} - \sigma_{22}| \tag{2.60}$$

$$\sigma = \frac{1}{3}(\sigma_{11} + 2\sigma_{22}) . \tag{2.61}$$

During shock compression of solid materials, the applied stress can be increased without bounds. This implies that the hydrostatic part of the stress tensor or the mean normal stress will continue to increase in response to the increasing applied stress but the deviatoric stresses will attain limiting values. In shock compression problems, it is customary to modify the Von Mises yield condition for an elastic-plastic material such that

$$(\sigma_{11} - \sigma_{22})^2 \leq Y^2, \tag{2.62}$$

where Y is the yield strength in simple tension. As a result of the above modification, both the second invariant of the deviatoric stress tensor and the maximum shear stress can be restated, respectively, as

$$J_2 \leq \frac{1}{3}Y^2 \tag{2.63}$$

$$\tau_{max} \leq \frac{1}{2}Y. \tag{2.64}$$

If the inequality in Equation (2.62) holds true, then the material response is elastic and satisfies Hooke's law (assuming the material is linear elastic) for which

$$\sigma_{ij} = 2\mu\epsilon_{ij} + \lambda\epsilon_{kk}\delta_{ij}, \tag{2.65}$$

where μ and λ are the Lame's constants. On the other hand, if the equality in Equation (2.62) does not hold true, then the material response is plastic. Considering the plastic response, it is customary to separate the principal strains into an elastic and plastic part. Note that the normal strains ϵ_{11}, ϵ_{22}, and ϵ_{33} are the principal strains in the uniaxial strain case because the shear strains are zero. This implies that

$$\epsilon_{11} = \epsilon_{11}^e + \epsilon_{11}^p \tag{2.66}$$

$$\epsilon_{22} = \epsilon_{22}^e + \epsilon_{22}^p \tag{2.67}$$

$$\epsilon_{33} = \epsilon_{33}^e + \epsilon_{33}^p. \tag{2.68}$$

Recalling from the uniaxial strain conditions

$$\epsilon_{22} = \epsilon_{33} = 0. \tag{2.69}$$

Applying the above conditions to Equations (2.67) and (2.68) leads to

$$\epsilon^e_{22} = -\epsilon^p_{22} \tag{2.70}$$

$$\epsilon^e_{33} = -\epsilon^p_{33}. \tag{2.71}$$

Since the plastic deformation of solid bodies is incompressible (volume preserving, i.e., no volume change), this implies that

$$\epsilon^p_{11} + \epsilon^p_{22} + \epsilon^p_{33} = 0. \tag{2.72}$$

But because of symmetry $\epsilon^p_{22} = \epsilon^p_{33}$, therefore

$$\epsilon^p_{11} = -2\epsilon^p_{22}. \tag{2.73}$$

Substituting ϵ^p_{22} from Equation (2.70) into Equation (2.73), the following is obtained:

$$\epsilon^p_{11} = 2\epsilon^e_{22}. \tag{2.74}$$

The total strain ϵ_{11} in Equation (2.66) can now be restated as

$$\epsilon_{11} = \epsilon^e_{11} + 2\epsilon^e_{22}. \tag{2.75}$$

Restating Hooke's law in Equation (2.65) in terms of stresses and elastic constants, and also taking into consideration that $\sigma_{22} = \sigma_{33}$ due to symmetry, the following relationships are obtained:

$$\epsilon^e_{11} = \frac{1}{E}\sigma_{11} - \frac{2\nu}{E}\sigma_{22} \tag{2.76}$$

$$\epsilon^e_{22} = \frac{(1-\nu)}{E}\sigma_{22} - \frac{\nu}{E}\sigma_{11} \tag{2.77}$$

$$\epsilon^e_{33} = \frac{(1-\nu)}{E}\sigma_{33} - \frac{\nu}{E}\sigma_{11}, \tag{2.78}$$

where ν and E are the Poisson's ratio and elastic modulus, respectively. By substituting Equations (2.76) and (2.77) into Equation (2.75), the following relationship for ϵ_{11} is obtained for the elastic regime:

$$\epsilon_{11} = \frac{(1-2\nu)}{E}\sigma_{11} - \frac{2\,(1-2\nu)}{E}\sigma_{22}. \tag{2.79}$$

Recalling from Equation (2.64), it is known that $(\sigma_{11} - \sigma_{22}) = Y$ for the plastic deformation case and also, $\sigma_{22} = \sigma_{33}$. Therefore, σ_{22} can be defined in terms of the yield strength as $\sigma_{22} =$

$\sigma_{11} - Y$ and substituted in Equation (2.79) and simplified to get Equation (2.80) for the plastic regime:

$$\sigma_{11} = K\epsilon_{11} - \frac{2}{3}Y, \tag{2.80}$$

where $K = (E/3)(1-2\nu)$ is the bulk modulus. Since the bulk modulus K increases nonlinearly with stress, the stress-strain response of solids is usually concave up (or shock up), as shown in Figure 2.11 [209, 235]. The primary difference between uniaxial strain (plate impact experiments) and uniaxial stress (Kolsky bar experiments) is the bulk compressibility term in Equation (2.80). For the uniaxial strain case, the stresses rapidly increase regardless of the yield strength or strain hardening due to the increase in bulk sound speed which is a function of pressure and hence, increase in bulk modulus.

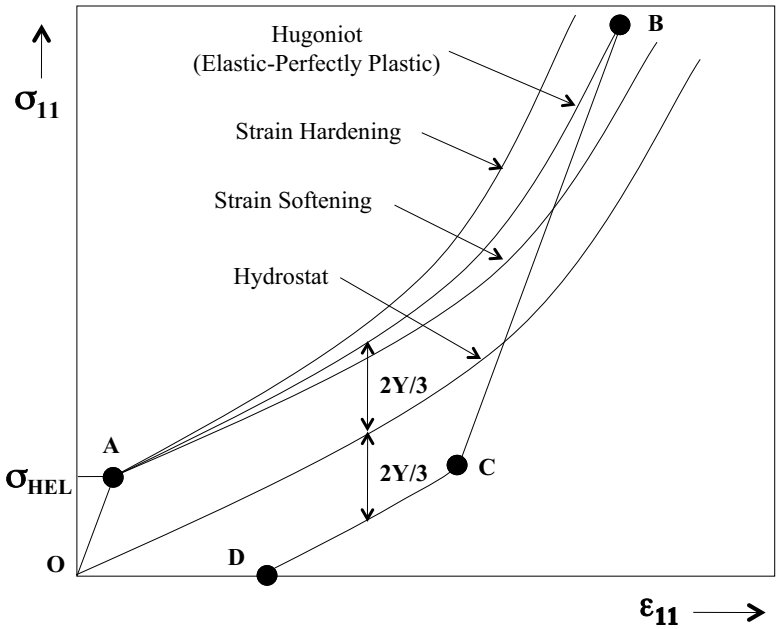

Figure 2.11: The uniaxial strain stress-stress response of an elastic-plastic material.

The elastic-plastic response is the simplest idealization of solid materials. The stress-strain response of an elastic-perfectly plastic solid is shown in Figure 2.11. The figure shows three distinct curves plus a loading (OAB) and unloading (BCD) path. The three distinct curves represent the hydrostat, strain hardening, and strain softening. Note that σ_{11} and ϵ_{11} in Figure 2.11 represents the shock stress and volumetric strain (dV/V_0), respectively. Under uniaxial compression, the response of the solid is elastic along OA until a limiting stress is reached. This limiting stress is referred to as the Hugoniot elastic limit (HEL) and it is the point at which the material can no longer sustain elastic distortions under uniaxial strain conditions. The HEL is the point at

which the solid material transitions from elastic to plastic response and it can be computed for an isotropic material using Equation (2.81) [211]:

$$\sigma_{HEL} = \frac{(1-\nu)}{1-2\nu} Y. \tag{2.81}$$

For an elastic-perfectly plastic solid, deformation beyond the elastic regime along AB is represented by the Hugoniot (which is a collection of loci of all possible end states achieved during the shock compression of a material at a given initial state). However, it is not the path followed during shock compression as mentioned earlier. The shock compression path is the Rayleigh line. The Hugoniot for an elastic-perfectly plastic solid has been found to deviate from the hydrostat by $(2/3)Y$ [109, 196, 211, 230, 235]. The hydrostat represents the mean normal stress. At point B, the material starts to unload elastically along BC then plastically along CD until the material is fully relieved of stress. Similar to the Hugoniot case for an elastic-perfectly plastic solid, the plastic unloading curve CD has been found to deviate from the hydrostat by $(2/3)Y$. Therefore, the total deviation between the Hugoniot and the plastic unloading curve is $(2/3)Y$. The dashed line above the Hugoniot curve represents a material undergoing strain hardening and that below the Hugoniot curve represents a material undergoing strain softening.

CHAPTER 3

Shock Recovery Experiments

The essence of a well-designed shock recovery experiment is to interrogate the residual structure-property relationships of a material, which has undergone a known uniaxial strain history under shock compression and then released back to ambient conditions without been exposed to collisions between planar free surface release waves and rogue edge radial release waves from lateral boundaries. Collisions between planar free surface release waves and rogue edge radial release waves can generate undesirable tensile stresses in the sample and, therefore, violate the uniaxial strain history essential for a successful shock recovery experiment. Therefore, all possible efforts must be utilized to trap rogue edge radial release waves emanating from lateral boundaries.

In shock wave research pertaining to the structure-property relationships in metals and metallic alloys, it is customary to subdivide shock recovery experiments into two types, namely shock-release experiments and shock-release-spall experiments. For shock-release experiments, the subject material is shock compressed to a desired stable Hugoniot stress, then released to ambient conditions and recovered for metallurgical analyses. Likewise, for shock-release-spall recovery experiments, the subject material is shock compressed to a desired stable Hugoniot stress, then released to a known fraction of the stable Hugoniot stress (not to ambient conditions) and then subjected to tensile stresses prior to recovery. If the tensile stresses are sufficiently high to nucleate, grow, and coalesce voids, then the subject material will fail by spallation. Shock-release recovery experiments are well suited to study deformation mechanisms and texture evolution; they are generally referred to as shock recovery experiments. Shock-release-spall recovery experiments are well suited to study incipient and complete spall failure (fractography); they are generally referred to as spall recovery experiments.

It is noteworthy to point out that the definition of spall recovery experiments is not consistent with the definition of a well-designed shock recovery experiment in a strict sense because the subject material is not released back to ambient conditions. However, they are generally classified as recovery experiments in shock wave research. This chapter pertains to shock recovery experiments but is limited to those executed using light gas gun and explosively driven shock recovery experiments and should not be considered a complete review of the subject. For more insight on the subject of recovery experiments pertaining to shock wave research, the reader is referred to [5–24, 27–31, 33–37, 40–42, 44–46, 236–239].

3.1 ROGUE EDGE RADIAL RELEASE WAVES

The primary challenge in shock recovery experiments is the trapping of the ubiquitous rogue edge radial release wave. Rogue edge radial release waves are intrinsic to the plate impact process. That is, when a flyer plate with sufficiently high velocity impacts a stationary target plate, two sets of compression waves (elastic and plastic or shock) are generated at the impact interface but travel in the opposite directions, left going into the flyer plate and right going into the target plate, as shown in Figure 3.1. At the same instant, edge radial release waves are generated at the impact edge designated as **I** in Figure 3.1a. As the elastic and shock waves in both flyer and target plates traverse toward their respective free surfaces in time *(t)*, the edge radial release waves traverse toward the center of both flyer and target plates simultaneously. Snapshots from a hydrocode simulation of a symmetric impact involving aluminum 1100-O [240] capturing the generation, propagation, and interactions between the elastic, plastic, and release waves at different time-steps during a plate impact event are shown in Figures 3.1b–e.

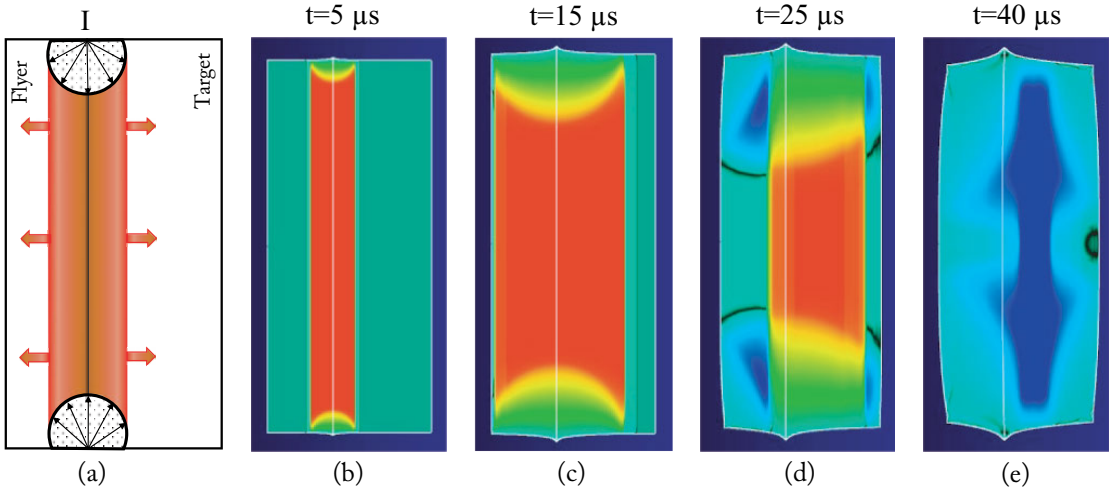

Figure 3.1: (a) An illustration of the ubiquitous rogue radial release wave resulting from a flyer plate impacting a stationary target and (b,c,d,e) are hydrocode simulation of an aluminum 1100-O flyer plate impacting an aluminum 1100-O target at various time steps ranging from 5–40 μs. The flyer plate is shown on the (left) and target plate on the (right) in all figures [240].

Figure 3.1b is a snapshot of the impact event taken at 5 μs after impact. The figure clearly reveals two shock waves traveling in opposite directions and an expanding radial release wave from the impact edge traversing to the center of the flyer and target plates. Note that red represents the compressed regions, blue the tensile regions, dark green the unshocked regions, and lime green the released regions in Figures 3.1b-e. At 15 μs (Figure 3.1c), the shocks and edge radial release waves have traveled further into the flyer and target plates. However, at 25 μs

(Figure 3.1d), the shock waves in both plates have reflected from their respective planar free surfaces as release waves and have collided with the edge radial release waves and consequently generated tensile regions in both the flyer and target plates. Finally, at 40 μs, it is clearly evident from Figure 3.1e that the bulk of the flyer plate has undergone full release but the mid-plane of the target plate is in tension. This mid-plane is referred to as the spall plane and if the tensile stresses are strong enough to nucleate, grow, and coalesce voids, then the material will fail by spallation.

For time-resolved in-situ (real-time) shock experiments, i.e., spall and release experiments, the detrimental effects of edge radial release waves are circumvented by using a conservative diameter-to-thickness ratio of approximately 5:1 or greater. Using such conservative estimates allows for the acquisition of pertinent shock and release transit data prior to the arrival of the rogue edge radial release waves at the center portion of the shocked sample. For shock recovery experiments, radial release waves must be mitigated in order to avert the detrimental effects of colliding release waves and, hence, maintain the uniaxial strain history required for successful shock recovery experiments. Tensile stresses resulting from colliding release waves are forbidden in shock recovery experiments, except for spall recovery experiments, where the sample being interrogated is allowed to spall due to tensile stresses resulting from colliding release waves.

Mitigating edge radial release waves requires some fundamental knowledge about the geometry of interacting shock and release waves resulting from a plate impact event [208]. Consider the plate impact geometry shown in Figure 3.2, which is one-half of a plate impact geometry, the center of the sample is designated by the dashed line C_L. When a flyer plate impacts a target plate, a fast-running elastic precursor wave (not shown in the figure) followed by a slower plastic or shock wave are generated in both the target and flyer plates. The stresses at the free surface edges are zero and, therefore, edge radial release waves are instantaneously generated and then expand into both the flyer and target plates as depicted by the curved red dashed line in Figure 3.2.

Ignoring the flyer plate and assuming that the stable shock stress in the material does not undergo attenuation from dissipative mechanisms, the particle at point A in Figure 3.2 moving with velocity u will traverse along the edge by a distance ut to point B after time t. During this same time period, the shock front will traverse a distance $U_s t$ in the target plate, where U_s is the shock velocity. The edge radial release wave at point B advances into the target material by a distance of ct, where c is the sound speed behind the shock wave. As the initial edge radial release wave behind the shock advances into the target material along the path AC, it catches up with the shock front at point C and progressively attenuates the shock wave. The shock front begins to acquire a curvature at point C, which moves inward into the target material as time progresses. Knowing the distances BC and BD, the distance DC can be easily computed.

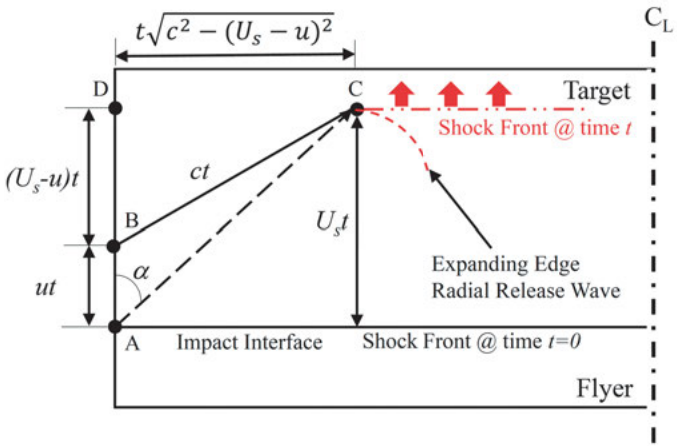

Figure 3.2: The geometry of interacting shock and release waves resulting from a plate impact event.

Therefore, the angle α, the angle between AC and AD is computed using the following equation:

$$\tan\alpha = \frac{t\sqrt{c^2-(U_s-u)^2}}{U_s t} \tag{3.1}$$

or

$$\tan\alpha = \sqrt{\left(\frac{c}{U_s}\right)^2 - \left(\frac{U_s-u}{U_s}\right)^2}. \tag{3.2}$$

It is a generally accepted practice to allow for the angle α to be approximately 45° or less when locating velocimetry detectors such as Velocity Interferometry System for Any Reflector (VISAR), Photon Doppler Velocimetry (PDV), and electrical shorting pins for in-situ measurement of shock transit time. Also, the detectors must be positioned to the right of point C in order to acquire the steady shock wave velocity profile without the influence of edge release waves.

Mitigating edge radial release waves is an essential component for conducting successful shock recovery experiments. The general consensus within the shock wave research community is to employ momentum trapping rings for mitigating edge radial release waves. Considerable efforts have been devoted to the design, analyses, and development of effective shock recovery assemblies over the past six decades [5, 22, 24, 37, 38, 46, 61, 241–243]. One of the prevailing designs currently employed by numerous researchers (including this author) to study the residual structure-property relationships in condensed matter is shown in Figure 3.3 [61]. The simulation results shown in Figure 3.3 [61] represent snapshots of a one-dimensional shock of approximately 9 GPa traversing a well-designed copper shock recovery assembly. At 2 μs relative to impact, the shock has traversed well into the copper sample and at 4 μs, release waves (green) are clearly evident at the boundaries of the momentum trapping rings. Further in time, between

6 μs and 10 μs, the release waves are shown to be trapped within the boundaries of the trapping rings allowing the sample to remain in uniaxial strain until release to ambient conditions. In addition to the lateral momentum trapping rings, spall plates at the back of the assembly are used to trap release waves from the back free surface. The results attained by this design when compared to those shown in Figure 3.1 have proven to be clearly effective for gas/powder gun shock recovery experiments.

Figure 3.3: A simulation of copper on copper impact (symmetric) using a well-designed shock recovery assembly for trapping rogue radial release waves. The numbers at the bottom represent 0 μs, 2 μs, 4 μs, 6 μs, and 10 μs relative to impact [61].

3.2 GAS/POWDER GUN-DRIVEN RECOVERY EXPERIMENTS

Gas and powder guns are the preferred methods of choice for conducting shock recovery experiments. However, they are limited in terms of impact velocity because the soft recovery process becomes extremely difficult at higher impact velocity. Therefore, explosives are generally used for studies where higher stresses are of interest. This section concerns the use of gas and powder gun driven shock recovery experiments and the next section deals with explosive-driven shock recovery experiments. The configurations of gas and powder gun-driven shock recovery experiments are identical except for the driving medium. Gas is used for gas gun operations and propellant for powder gun operations. An illustration of the general configuration for both gas and powder gun operations is shown in Figure 3.4, nevertheless some components may vary from one research laboratory to another.

The general configuration consists of four main components, namely gas/powder breech (not shown in the Figure 3.4), gun barrel, test chamber, and catch tank. The reader should note that the gun control system is excluded for austerity. The gas/powder breech is a high pressure vessel used for driving a launch package down the length of the gun barrel via a compressed gas

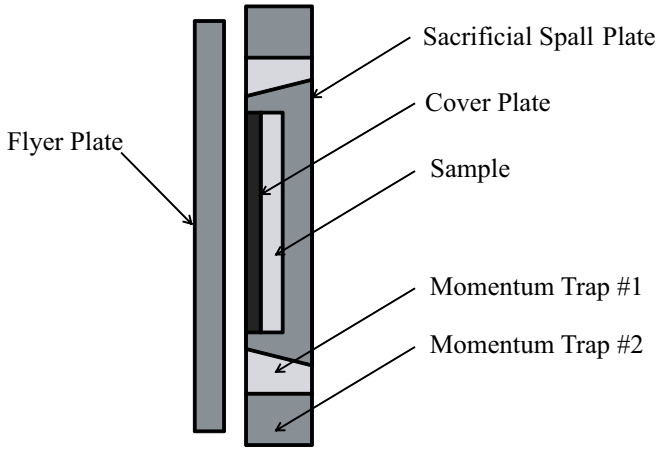

Figure 3.5: A cross-sectional illustration of the flyer plate and shock recovery assembly loading configuration used for both gas and powder gun shock recovery experiments [236].

can be easily dislodged from the inner momentum trapping ring (#1) after impact. A minimum of two concentric momentum trapping rings must be used for trapping radial release waves. The appropriate spall plate thickness, (h), and trapping rings width, (w), are determined using the following equations, respectively [12]:

$$h \geq \frac{C_L}{C_o}\left[\left(\frac{U_s + C_o}{U_s + C_L}\right) d^D + \left(\frac{U_s - C_o}{U_s + C_L}\right) d^T\right] \tag{3.3}$$

$$w \geq \frac{C_L}{C_o}\left[\left(\frac{U_s + C_o}{U_s}\right) d^D + d^T\right], \tag{3.4}$$

where C_o is the bulk sound speed at ambient pressure, C_L is the longitudinal wave speed, U_s is the shock velocity in the trapping ring material, and d^D and d^T are the thicknesses of the driver (flyer) and target (sample) plates, respectively.

The sample is tightly sandwiched inside the spall plate cavity by a cover plate fabricated from a tough impedance matching material for increased protection during impact and the soft recovery process. After impact, the cover plate, sample, and spall plate assembly are separated from the trapping rings, while the sabot is stripped by the high strength steel containment positioned within the test chamber (see Figure 3.4). The cover plate, sample, and spall plate assembly first travel through a series of structural foams stacked in sequence from low to high density in the test chamber in order to gradually decelerate the shock recovery assembly and, therefore, minimize detrimental effects emanating from secondary impacts. Secondary impacts may possibly change the microstructure achieved at the shock state and possibly lead to erroneous conclusions. The assembly then enters the catch tank and goes through a cylindrical block of chilled ballistic foam. The ballistic foam is chilled at an average temperature of approximately

9°C and is used for quenching and decelerating the assembly. As a final step, the assembly is soft recovered in rags and then retrieved for sectioning and metallurgical examination. Note that some researchers use more than two momentum trapping rings and multiple spall plates for added assurances on mitigating rogue radial release waves; see Figure 3.3 [61]. The shock recovery process was previously described by Williams et al. [236] using commercially pure 1100-O aluminum sample.

3.3 EXPLOSIVE-DRIVEN RECOVERY EXPERIMENTS

Gas gun-driven systems are generally preferred over explosive driven systems for conducting shock recovery experiments because they offer better experimental control, i.e., impact velocity and planarity; however, they are generally limited in terms of impact velocity and, hence, shock stress. Note that high stresses can also be generated at lower impact velocities using gas gun-driven flyer plates fabricated from high impedance materials such as tungsten, tungsten carbide, tantalum, etc., but such non-symmetric loading configurations can lead to complex wave interactions and complications in data interpretation.

For instance, to achieve a 20 GPa stable shock stress in magnesium using symmetric gas gun-driven plate impact experiments will require an impact velocity in excess of 3.3 km/s. For such impact velocity, the soft recovery process becomes impractical. Consequently, explosive driven systems are well suited for such high stresses and the sample can be soft recovered reasonably well. Explosive-driven systems are relatively cost effective to setup and execute compared to gas gun driven systems but require rigorous safety protocols. Explosives handling require great care due to the violent nature of explosives. This section is limited to two types of explosive driven shock recovery experimental setups: the first concerns the generation of planar shock waves in materials and are well suited for studying deformation mechanism and spall failure in metals/metallic alloys, the second concerns the compaction and consolidation of powders and powder mixtures.

Different explosive-driven shock recovery experimental setups have been developed over the past several decades for studying the structure-property relationships in materials under extreme dynamic environments but the two commonly used are shown in Figure 3.6 [58, 244]. Both experimental setups shown in Figures 3.6a,b can offer the experimentalists a wide variety of shock stresses and pulse durations. They are similar in design but with one primary difference, the experimental setup in Figure 3.6b employs a flyer plate at a prescribed standoff, which allows for variations in pulse duration.

Immediately after initiation of the detonator, the resulting detonation wave is transformed into a planar shock by a plane wave generator or plane wave lens. At a later time, the planar shock will simultaneously initiate the main explosive charge along its surface. Detonation of the main explosive charge generates the desired shock stress for loading the sample, as shown in Figure 3.6a, or energy for driving the flyer plate to the prescribed velocity, as shown in Figure 3.6b. As revealed in the figure, the sample must be sandwiched within an impedance matching mo-

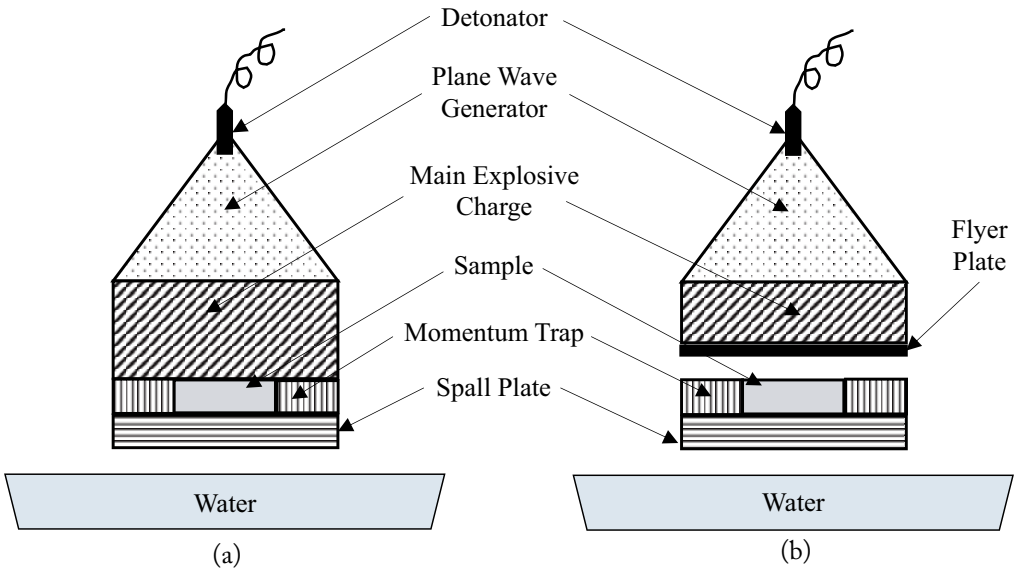

Figure 3.6: Illustrations of (a) a plane wave generator and (b) a stand-off flyer plate plane wave generator commonly used for explosive-driven shock recovery experiments [58, 244].

mentum trapping material in order to mitigate rogue release waves. A sacrificial spall plate of matching impedance is also used if the objective of the research is to study deformation mechanisms or else it can be removed to study spall failure. The sample is finally recovered in a water bath in order to quench and, therefore, prevent reorganization of the residual substructure or static recovery in the sample at elevated temperature. Both experimental setups are widely used to study the structure-property relationships of materials under extreme conditions.

Powder metallurgy in a broad sense implies the compaction and consolidation of powders and powder mixtures to form materials or near net-shape commercial products. The use of high explosives offer an efficient way of depositing the energy required for shock compaction and consolidation of powders and powder mixtures. The resulting products acquired from shock compaction and consolidation possess high density with improved mechanical properties such as ductility, strength, and hardness [244]. The use of high explosives for shock compaction and consolidation of powders and powder mixtures can be traced back to the 1950s and has since been used in the production of hard materials such as artificial diamond [27, 245], boron nitride [246], silicon carbide [247], etc. [248], from their powder form. Reviews on the shock compaction and consolidation of powders and powder mixtures have been written by Gourdin [249], Prummer [250], Thadhani [237, 251], Meyers [58], Sawaoka [252], and Murr [244, 253].

The most common and simplest of all experimental design used for shock compaction and consolidation of powders and powder mixtures is the single tube cylindrical configuration

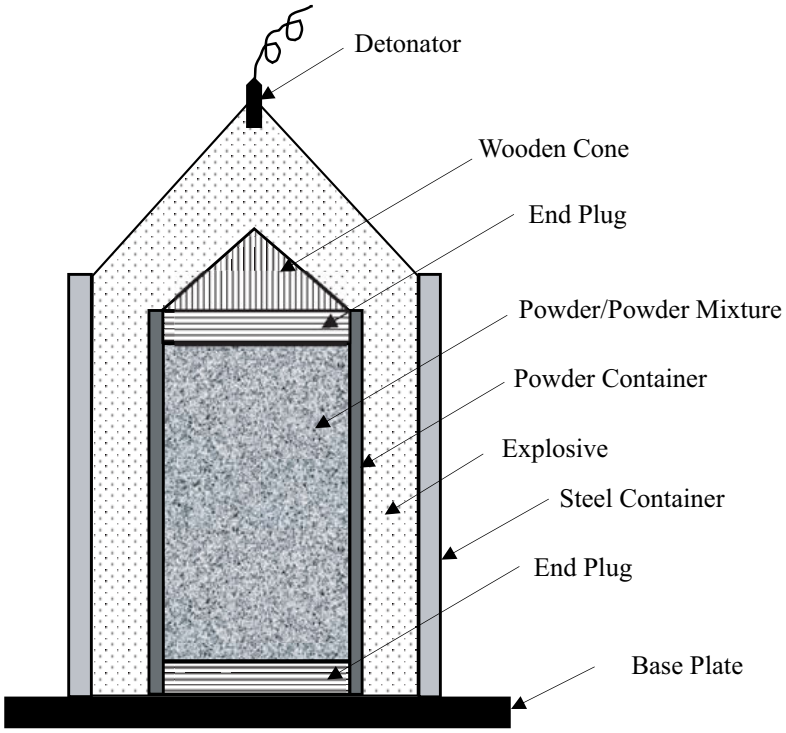

Figure 3.7: An illustration of the basic components of a simple single tube cylindrical configuration used for shock compaction and consolidation of powders and powder mixtures [58, 237, 244, 249–251, 253].

shown in Figure 3.7. The overall design is quite simple and the required components can be easily fabricated. Because of its simplicity, the total cost of conducting such experiment is relatively low. The basic components of a simple single-tube cylindrical configuration used for shock compaction and consolidation of powders and powder mixtures are shown in Figure 3.7.

The powder or powder mixture to be compacted or consolidated is packed in a metallic powder container and then encapsulated by end plugs. The powder container is then placed in a steel container which is filled with the chosen explosive. The explosive is chosen based on the desired shock pressure required for compaction and consolidation; the desired shock pressure can be varied by increasing or decreasing the amount of explosive used. In general, explosives with high detonation velocities will generate higher shock pressures than those with lower detonation velocities. Table 3.1 shows a list of common explosives and their corresponding properties [254–256].

After detonation of the explosive, the pressure pulse traverses along the powder container from top to bottom and converges toward the central axis. If the pressure pulse is excessive, a

Table 3.1: A list of common explosives and their corresponding properties. ρ_o, V_D, ρ_{CJ}, and P_{CJ} are density, detonation velocity, density at the Chapman–Jouget state, and Chapman–Jouget pressure, respectively [254–256].

Explosive	Composition	$\rho_o(g/cc)$	$V_D(m/s)$	$\rho_{CJ}(g/cc)$	$P_{CJ}(GPa)$
ANFO	5.8% Fuel Oil	0.82	4.55	1.21	5.5
Comp B	RDX/64, TNT/36	1.72	8.02	2.33	29.2
HMX		1.89	9.11	2.52	39.0
HMX/Insert	95/5	1.78	8.73	2.37	33.5
Octol	75.25	1.80	8.55	2.35	30.7
PBX-9502		1.90	7.71	2.55	28.9
Pentolite	50/50	1/64	7.52	2.26	25.2
PETN		1.77	8.27	2.45	33.5
RDX		1.80	8.59	2.42	34.1
RDX/TNT	78/22	1.76	8.31	2.38	31.7
TNT		1.64	6.95	2.33	17.7
Baratol	72/28	2.45	5.00	3.27	15.4
Lead Azide		3.70	4.48	4.70	15.8
HMX/Viton	85/15	1.87	8.47	2.53	35.0
HBX-1		1.71	7.31	2.26	22.0

central hole is formed due to the convergence of the shock waves at the central axis of the powder container [257]. This phenomenon is known as Mach stem formation and can be eradicated by placing a solid metal rod at the central axis of the powder container or changing the explosive to one with lower detonation velocity and, hence, lower shock pressure. Cracking and Mach stem formation are of serious concern in shock compaction and consolidation of powders and powder mixtures but they can be mitigated by making specific adjustments; see Staudhammer and Johnson [257], Carton et al. [258], Nishida et al. [259], and Meyers and Wang [260].

CHAPTER 4

Deformation Mechanisms and Spall Failure

As previously stated in Section 1.3, the plastic response and residual mechanical properties of most shock compressed metals and metallic alloys are quite different than those acquired from quasi-static to moderate strain rates. These observed changes in the plastic response and residual mechanical properties across various strain rate regimes are manifestations of the microstructure and microstructure evolution which can have important consequences on the spall failure of materials. The microstructure and its evolution are highly influenced by numerous shock wave parameters but the two main influential are the shock stress and pulse duration. The nucleation and accumulation of defects which progresses to damage and consequent spall failure in metals and metallic alloys cut across multiple length scales (from atomic-to-micro-to-continuum) [74, 261–264]. These defects can range from vacancies and vacancy clusters, interstitial atoms, dislocations and dislocation networks, stacking faults, deformation twins, to inter-metallic and second-phase particles, voids, and cracks. Therefore, the primary objective of this chapter is to elucidate the role of microstructure and microstructure evolution on the structure-property relationships pertaining to shock compressed metals-metallic alloys and powders-powder mixtures.

4.1 MECHANICAL PROPERTY CHANGES IN SHOCK COMPRESSED METALS

The spallation process is made more complicated by the fact that materials are first subjected to shock compression prior to tensile loading, and during the shock compression phase, the original microstructure of the material may evolve. Depending on the magnitude of the preceding shock stress, large amounts of lattice defects such as dislocations can be introduced in the material which can lead to strengthening effects such as hardening and therefore, change the material behavior [6, 13, 14, 16, 58, 236, 265, 266]. However, a material cannot be hardened indefinitely; therefore, a saturation level may be attained in the strength, and then the hardness may even decrease with further increase in shock stress [23, 244, 267]. This behavior is sometimes attributed to shock induced heating which may lead to dynamic recovery and recrystallization [268].

Dynamic recovery involves the annihilation of dislocations by glide and cross-slip in mixed sub-boundaries. It is strongly influenced by thermal activation but can also occur mechanically, in principle even at absolute zero temperature [269]. At low temperatures, climb is not sig-

nificant and therefore, edge dislocations cannot annihilate [269]. With increase in stress and temperature, edge dislocations not only begin to diffuse but combine to form edge dipoles. Previously stored dislocations are rearranged under the action of stress, temperature, and strain rate into lower energy configurations such as dipoles and incipient sub-boundaries [269]. This rearrangement is primarily responsible for dynamic recovery. Furthermore, changing either the stress, temperature, or strain rate can influence the degree of rearrangement in the deformed material [270]. These rearrangements are usually reflected in the substructure of the shock recovered material.

For instance, increases in the residual dislocation debris within the cell interior and/or suppression of dislocation cells are both manifestations of the thermally activated nature of dynamic recovery [236, 270–273]. Dislocation debris left in the wake of the advancing dislocations can also act as a hardening agent [274]. That is, they become obstacles to trailing dislocations and are believed to cause self hardening [78, 274]. The mechanism of dislocation debris hardening is not well understood. However, their contributions to the total hardening of the plastically deformed metal or metallic alloy is probably small [274]. The activation energy required for cross slip is inversely proportional to the stacking fault energy [273, 275]. Therefore, metals with high stacking fault energy such as aluminum ($\sim$ 200 mJ/m^2) require low activation energy for cross-slip and are therefore predisposed to favor dynamic recovery, while metals with low stacking fault energy do not [58, 138, 276–280]. Dynamic recovery usually manifests itself as work or shock softening [267, 281].

Numerous researchers have extensively studied the structure-property relationships in shock-compressed solids and have extracted important data from shock recovered samples that shed light on the residual hardness and post-shock mechanical properties [6, 13, 14, 39, 60, 64, 236, 266, 282–285]. Their findings show that there are simplified empirical linear relationships between residual hardness and peak shock stress up to a point for a significant number of materials as shown in Figure 4.1. These relationships are generally represented by the empirical forms:

$$\sigma = \sigma_0 + \alpha\mu b\sqrt{\rho} + K_1 d^{-1} + K_2\Delta^{-1/2} \tag{4.1}$$

$$(\sigma - \sigma_0) = \zeta(H - H_0) = 2\alpha\mu b\sqrt{P}, \tag{4.2}$$

where σ is the post-shock yield strength, σ_0 is the pre-shock yield strength, ρ is the dislocation density, K_1 and K_2 are material parameters, α is a constant ~ 0.5, μ is the shear modulus, d is the cell size, Δ is the twin spacing, b is the magnitude of the Burger's vector, ζ is a constant, H and H_0 are the post-shock and pre-shock hardnesses, and P is the peak shock pressure or stress. Equation (4.1) implies that the post-shock yield strength increases with increase in dislocation density, decrease in cell size, and decrease in twin spacing. The twin spacing term in Equation (4.1) can be neglected for polycrystalline materials that do not exhibit twinning. In general, the dislocation density increases with increase in shock stress and the cell size decreases with increase in shock stress. Consequently, Equations (4.1) and (4.2) suggest that increasing

the peak shock stress will result in an increase in the post-shock yield strength and hence residual hardness.

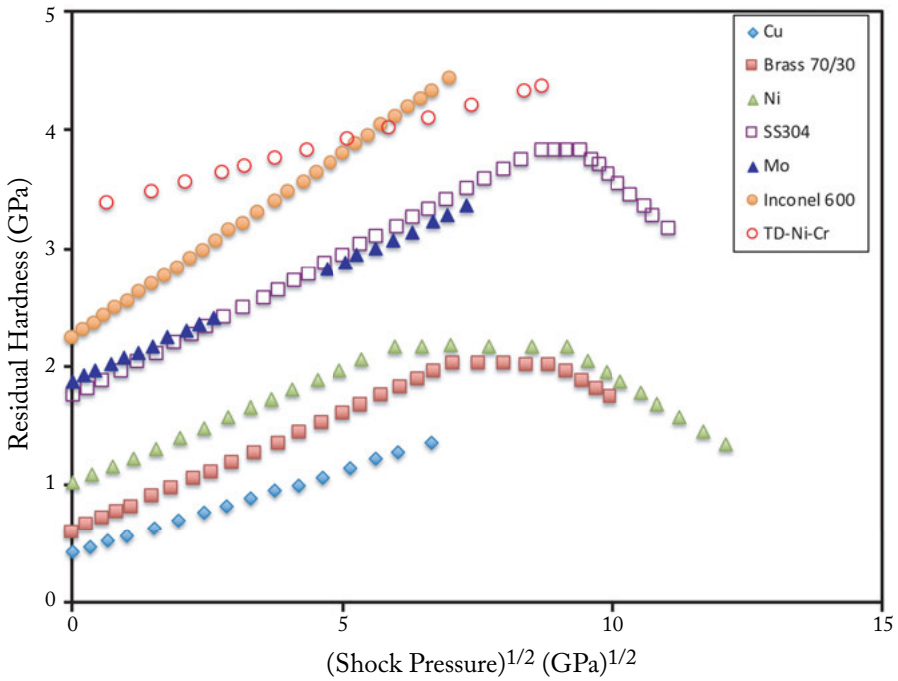

Figure 4.1: Residual hardness as a function of peak shock stress for several important metals and metallic alloys. Reproduced from [244].

Previous observations from experiments support the fact that increasing the peak shock stress and pulse duration do lead to a significant increase in the post shock yield strength of many metals and metallic alloys. Shown in Figure 4.2a [286, 287] is the stress-strain behavior of ordered FCC intermetallic Ni_3Al samples which have been shocked to approximately 14.0 GPa and 23.5 GPa stress, respectively. The ordered FCC intermetallic Ni_3Al samples exhibit rate-dependent hardening behavior and a significant increase in the post shock yield stress when compared to their annealed counterparts. Similar observations were made for FCC Ni shocked to 10.0 GPa, as shown in Figure 4.2b [286, 287]. The stress-strain behaviors exhibited by FCC intermetallic Ni_3Al and FCC Ni are consistent with Equations (4.1) and (4.2). Shock-strengthening behavior has been previously observed in molybdenum [288, 289], copper [290], and 304 stainless steel [291]. Also shown in Figures 4.2a,b are the rate insensitive behavior and lack of shock strengthening in intermetallic Ti-48Al-2Cr-2Ni alloy and BCC Ta [286, 287], respectively. All these changes in the structure-property relationships are manifestations of the microstructure and microstructure evolution.

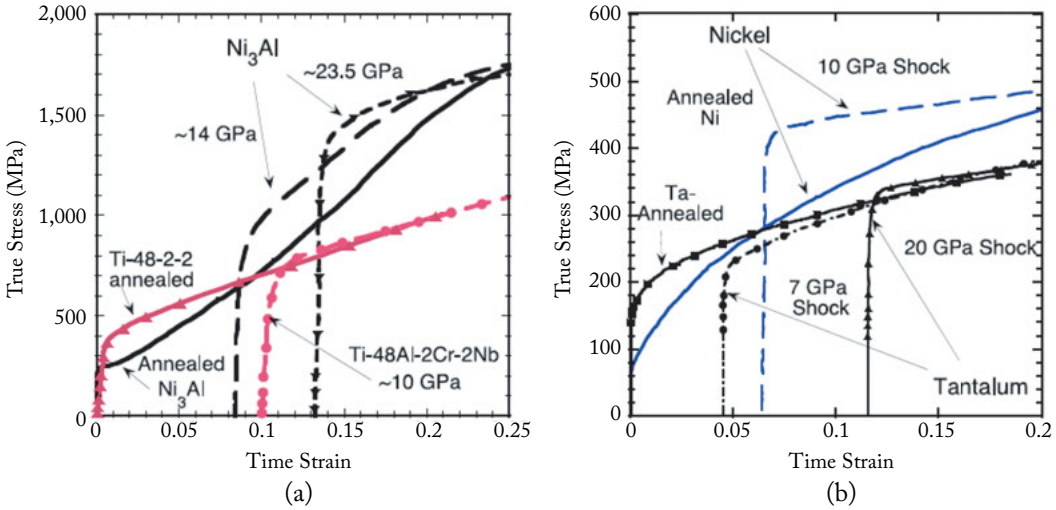

Figure 4.2: Stress-strain response of pre-shock and post-shock metals and metallic alloys [287].

4.2 MICROSTRUCTURE CHANGES IN SHOCK COMPRESSED METALS

When metals and metallic alloys are subjected to shock waves, a specific type of substructure is developed in order to accommodate plastic deformation. This substructure may consist of lattice defects such as vacancies and vacancy clusters, interstitial atoms, dislocations, dislocation cells and networks, stacking faults, deformation twins, etc. The defects generated in metals and metallic alloys under shock compression depends on several factors such as shock parameters (peak shock stress, pulse duration, strain-rate), crystal structure (FCC, BCC, HCP), grain size and type (single crystal, nanocrystal, ultra-fine grained, coarse grained), alloying elements, second-phase particles, and temperature. This section is concerned with the substructure and substructure evolution of lattice defects in shock compressed metals and metallic alloys.

4.2.1 SUBSTRUCTURE IN SHOCK COMPRESSED METALS WITH FCC LATTICE STRUCTURE

It is well known that the stacking fault energy of a material to a large extent determines the nature of the dislocation substructure formed during plastic deformation. For instance, materials with high stacking fault energy such as aluminum, copper, and nickel form a well-defined cell structure at room temperature [17]. Whereas materials with low stacking fault energy such as 304 stainless steel and Hadfield steel tend to form planar arrays of dislocations [17]. Williams et al. [236] examined the substructure and its evolution in shock compressed FCC 1100-O aluminum. Their results reveal that the original equiaxed grains shown in Figure 4.3a evolved into

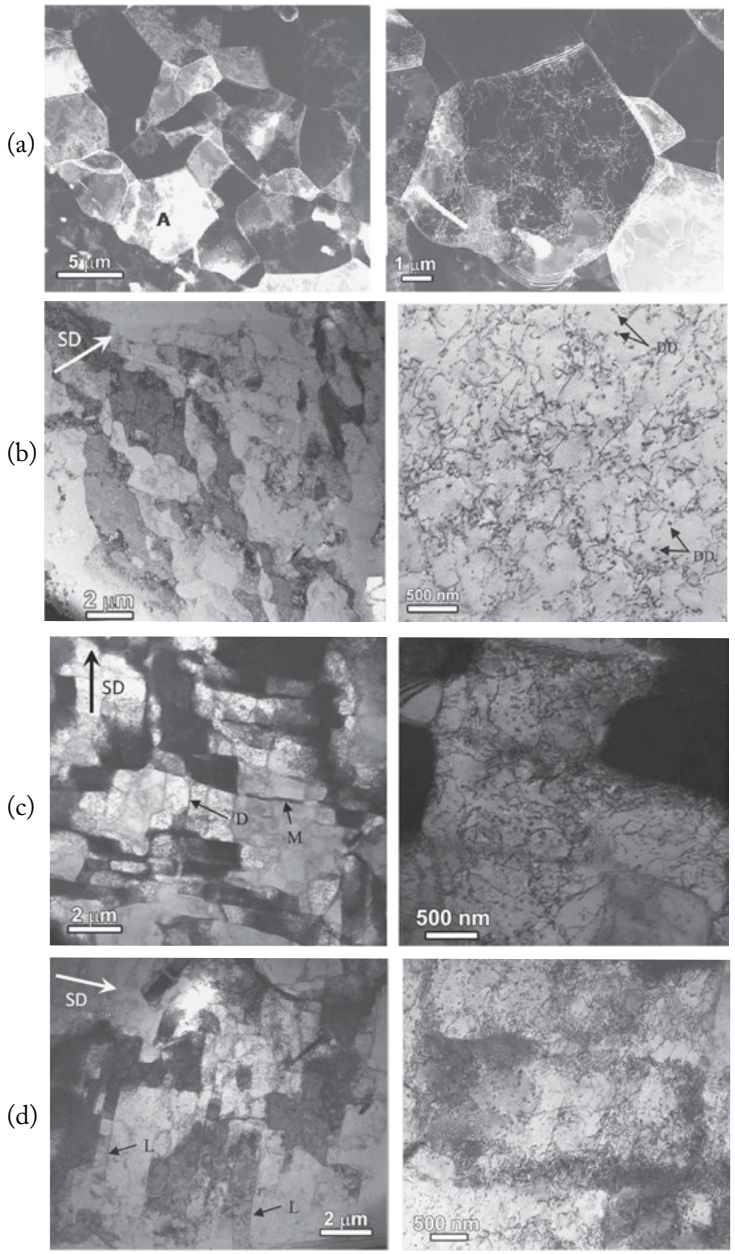

Figure 4.3: TEM micrographs of (a) the as-recieved, (b) shocked at 4 GPa, (c) shocked at 6 GPa, and (d) shocked at 9 GPa 1100-O aluminum [236]. The right column is a magnified view of the left column.

severely elongated sub-grains with cells in their interior when shock compressed to 4 GPa, as shown in Figure 4.3b. Slightly tangled dislocation substructures also begin to develop in the interior of the sub-grains (Figure 4.3b). Dislocation debris (denoted DD in the figure) is also observed to be uniformly distributed throughout the micrograph (Figure 4.3b). Dislocation debris is a direct consequence of the double cross-slip mechanism [78, 274].

Williams et al. [236] found the substructure of 1100-O aluminum shock compressed to 6 GPa (Figure 4.3c) to be distinctly different from that shocked at 4 GPa (Figure 4.3b). The starting microstructure evolved into densely packed cell blocks delineated by dense dislocation walls (DDWs: denoted by D) and microbands (MBs: denoted by M), as depicted in Figure 4.3c. The cell block boundaries (DDWs and MBs) accommodate the strain mismatch between cell blocks and are therefore referred to as geometrically necessary boundaries (GNBs) [292]. The formation of DDWs and MBs in plastically deformed aluminum has been described previously by Hansen [292] and Bay et al. [293]. A magnified view of the interior of a cell block is shown in Figure 4.3c and it reveals a substructure of discrete dislocations and dislocation debris reminiscent to that obtained at 4 GPa. For a shock stress of 9 GPa, the starting microstructure evolves into a plate-like lamellar structure as shown in Figure 4.3d. The lamellar structure (denoted by L) exhibits long strips with flat boundaries running almost parallel to each other with a single cell block spanning across them. Also observed in Figure 4.3d are aggregated dislocations and dislocation debris reminiscent to those observed at 4 GPa and 6 GPa peak shock stress. These results show a substantial evolution of the substructure with increase in peak shock stress.

Furthermore, the substructure and substructure evolution in shock compressed FCC aluminum have been studied under different shock loading conditions. Gray [59] and Gray and Huang [265] studied the influence of single and repeated shock loading on the substructure evolution of 99.99 wt.% aluminum at −180°C and made the following observations. Dislocation cells with a high density of vacancy loops are formed for a single shock (see Figure 4.4) but the substructure evolution with respect to repeated shocks is observed to be progressive in nature and reminiscent to the dislocation arrangements in FCC single crystals and polycrystals with increasing strain. They also observed the substructure evolve from dislocation cells to planar slip bands to microbands and this was found to be particularly evident adjacent to grain boundaries. Although coarse-grained aluminum and aluminum alloys do not show any propensity for deformation twinning at room temperature because of their high stacking fault energies, the residual microstructure of Al-4.8 wt.% Mg shocked to 13 GPa at approximately 100 K (see Figure 4.5) [59] and 6061-T6 aluminum shocked to 13 GPa at 298 K [294] have revealed their existence.

The substructure evolution in shock-compressed polycrystalline and single-crystal FCC copper (Cu) has been extensively studied for many years [56, 65, 66, 268, 271, 295–301]. Senser et al. [282] studied the influence of pre-strain and shock-pulse shape on the structure-property behavior of polycrystalline copper shock loaded to 6.6 GPa. They employed both square-topped and triangular-shaped shock pulse configurations at room temperature. They found that the Cu samples shock loaded using a triangular-shaped shock pulse exhibited a 10% higher yield

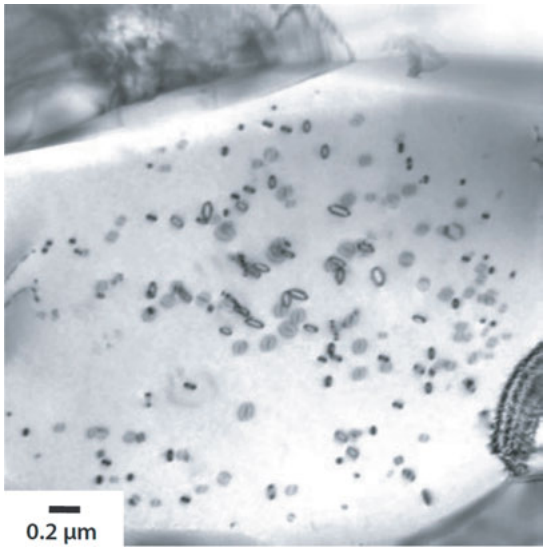

Figure 4.4: Bright-field electron micrograph of vacancy loops formed in shocked 99.99 wt.% aluminum at −180°C [59, 265].

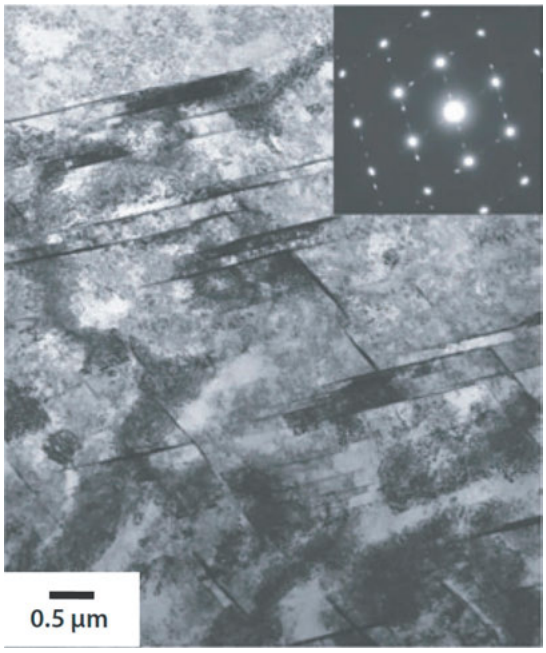

Figure 4.5: Bright-field electron micrograph showing two deformation twin variants in Al-4.8 wt.% Mg shock compressed to 13 GPa at approximately 100 K [59].

strength than Cu samples shocked using the square-topped wave. Their results also show subtle differences in the residual substructure between the Cu samples shocked with a triangular-shaped shock pulse and those shocked with a square-topped shaped shock pulse as shown in the micrograph in Figure 4.6. Transmission Electron Microscope (TEM) examinations of the pre-strained copper samples which were subsequently shock loaded to 6.6 GPa revealed a significant change in the substructure. The non-uniform cell size of the samples which were quasi-statically pre-strained (at 10^{-3} s^{-1}) to 5% plastic strain became uniform and reduced in size after being shocked with the square-topped and triangular-shaped waves (see Figure 4.7). The substructure did not reveal any deformation twins possibly due to the low shock stress.

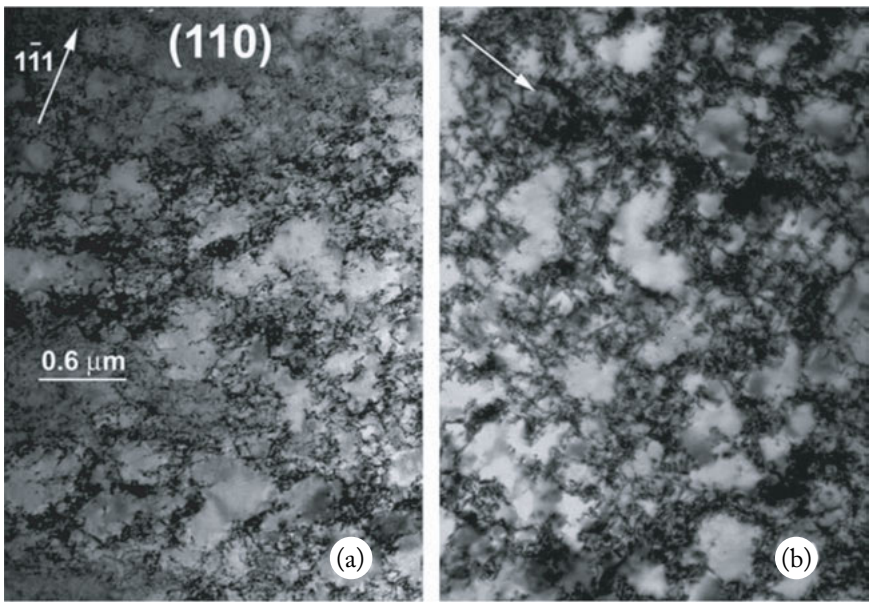

Figure 4.6: Bright-field TEM images of the shocked copper samples: (a) triangular-shaped wave and (b) square-topped wave [282].

The substructures developed in M1 copper samples shock and quasi-isentropically compressed to stresses ranging from 20–80 GPa and at strain rates ranging from 10^5–10^9 sec^{-1} were interrogated by Podurets et al. [302]. Deformation twins were observed in the substructures of both the shock and quasi-isentropically compressed M1 copper samples with initial grain size of 20 μm. For the shock compressed samples, they categorized the residual deformation twins into three distinct groups based on their characteristic sizes. As shown in Figure 4.8, deformation twins with thicknesses smaller than 10 nm and approximately 100 nm are classified as *thin* twins and *thick* twins, respectively. Furthermore, a group of deformation twins which is approximately 4 μm thick is classified as *bands* of twins. Podurets et al. [302] concluded that the aggregate of these groups of deformation twins are responsible for the formation of localized strain bands

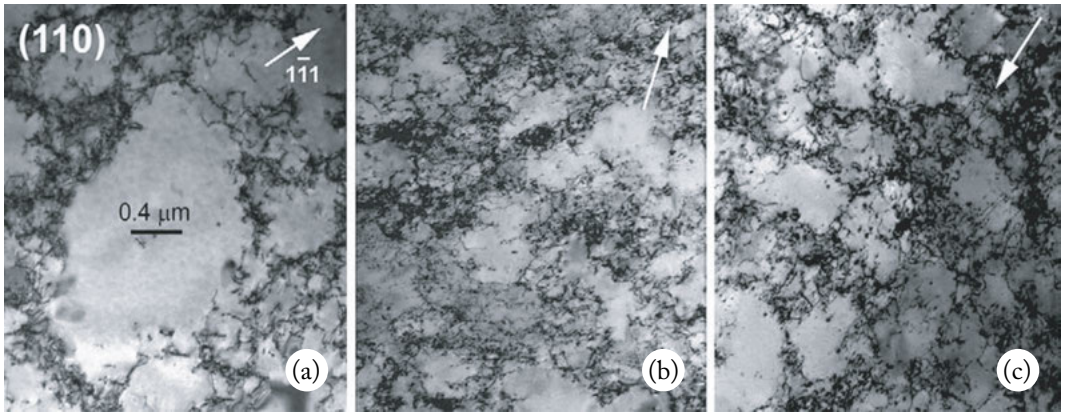

Figure 4.7: Bright-field TEM images of copper samples after pre-straining to (a) 5% plastic strain quasi-statically, (b) shock loaded with a triangular-shaped wave, and (c) shock loaded with a square-topped wave [282].

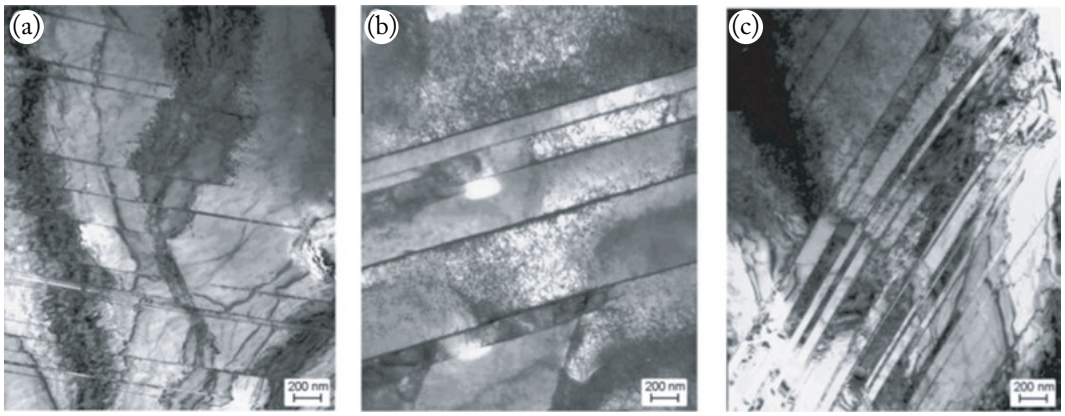

Figure 4.8: The morphology of the twin structures developed in shock-compressed copper, (a) thin parallel twins, (b) thick twins, and (c) band of twins [302].

(LSBs) within the grain interior. The number of bands within the microstructure was found to increase as the grain size and strain rate increases and with decreasing sample temperature. They estimated the characteristic time of formation of twin bands in copper to be 0.3 μs.

The role of interface structure on the substructure and substructure evolution in shock-loaded copper [100]/[111] multicrystal was studied by Perez-Bergquist et al. [303]. Their results show that the substructure evolution was highly dependent on grain orientation (see Figure 4.9). The [100] grains exhibited loose dislocation tangles but not well developed dislocation cells, as

shown in Figure 4.9a. Also, the [100] grains reveal extensive deformation twinning (see Figure 4.9b). Additionally, the [111] grain exhibited no deformation twins but exhibited more extensive dislocation accumulation and well-defined dislocation cells (see Figure 4.9c). The slip system activity and substructure evolution in monocrystalline copper samples with [001] and [221] orientations shocked to 30 GPa and 57 GPa, respectively, at 90 K were investigated by Cao et al. [304] and they concluded that the residual substructures are dependent on crystalline orientation and shock stress. The differences in residual substructure as a function of crystal orientation are attributed to the different resolved shear stresses on specific crystallographic planes. Cao et al. [304] show that the sample with [001] orientation shocked to 30 GPa exhibited slip bands and stacking faults, as shown in Figure 4.10a (note that the slip bands are not revealed in the micrograph). The figure clearly shows two sets of stacking fault traces, $[0\bar{2}\bar{2}]$ and $[02\bar{2}]$ in the (100) plane. They postulated that the stacking faults in the $[0\bar{2}\bar{2}]$ direction were formed prior to those in the $[02\bar{2}]$ direction because they are continuous, while the $[02\bar{2}]$ stacking faults are segmented. On the other hand, the sample with [221] orientation shocked to 30 GPa reveal both microbands and slip bands, as shown in Figure 4.10b (note that the slip bands are not revealed in the micrograph). At higher stresses, the sample with orientation [001] shocked to 57 GPa, reveal a nonuniform substructure consisting of different defects, such as bands (see Figure 4.11a), microtwins (see Figure 4.11b), and dislocations (see Figure 4.11c) randomly distributed throughout the entire sample. The sample with orientation [221] shocked to 57 GPa were fully recrystallized revealing annealing twins within the grains, as shown in Figure 4.12, which is a characteristic feature of static recrystallization.

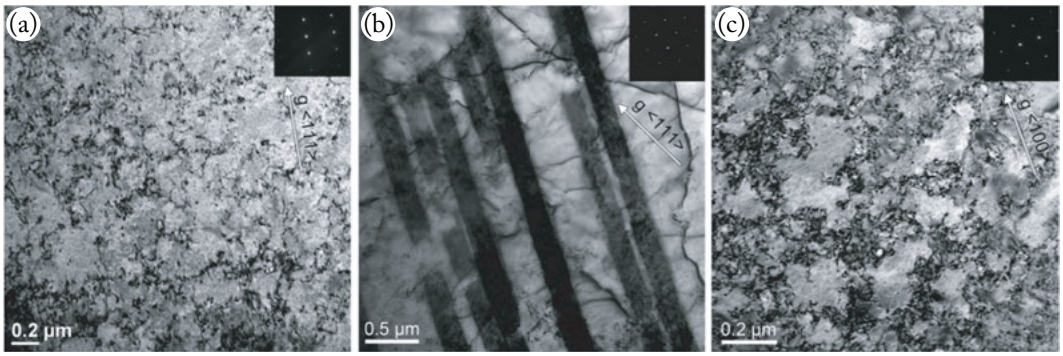

Figure 4.9: TEM micrographs showing the bulk substructure of (a, b) the shocked [100] grain and (c) the shocked [111] grain. The shocked [100] grain exhibited (a) loose dislocation tangles and (b) extensive twinning. The shocked [111] grain exhibited (c) more well-defined dislocation cells but no twinning [303].

A substantial amount of recovery experiments spanning over four decades have been conducted in order to probe the microstructure and microstructure evolution in nickel undergoing shock compression [124, 285, 305–313]. The general consensus derived from these experimental

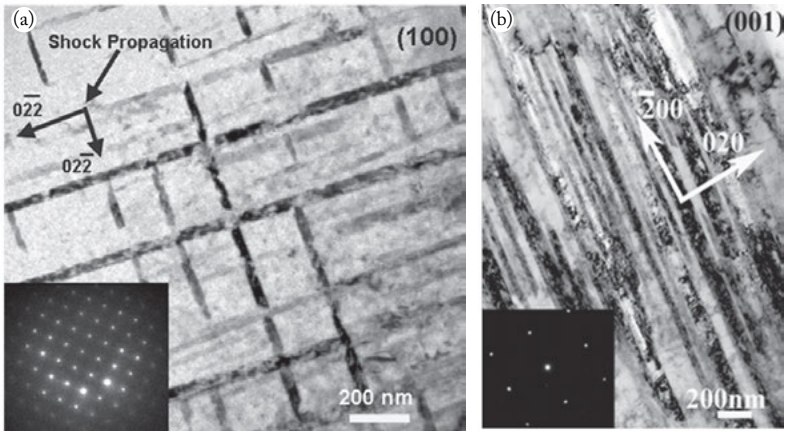

Figure 4.10: TEM micrographs showing (a) stacking faults on the (100) plane in [001] monocrystalline copper shocked to 30 GPa and (b) microbands on the (001) plane in [221] monocrystalline copper shocked to 30 GPa [304].

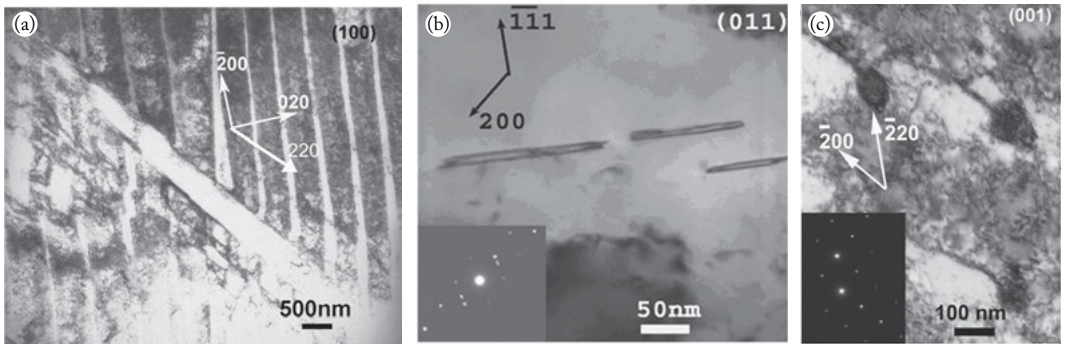

Figure 4.11: TEM micrographs showing (a) microbands on the (100) plane, (b) microtwins on the (011) plane, and (c) dislocation structures on the (001) plane in [001] monocrystalline copper shocked to 57 GPa [304].

results according to Greulich and Murr [124], stipulates that when nickel is shock compressed up to 30 GPa, the substructure primarily consists of dislocation cells. Beyond 30 GPa shock stress, the dominant substructural features are stacking faults and deformation twins. These substructural features are known to be hardening mechanisms in shock compressed nickel and have been corroborated by the experimental results by Esquivel et al. [309], as shown in Figure 4.13. The as-received coarse-grained Ni consisting of poorly-formed dislocation cells (Figure 4.13a), when shock compressed to 30 GPa (which is the critical stress required for twinning in coarse-grained polycrystalline Ni) evolves to deformation microtwins (Figure 4.13b). But when the as-received

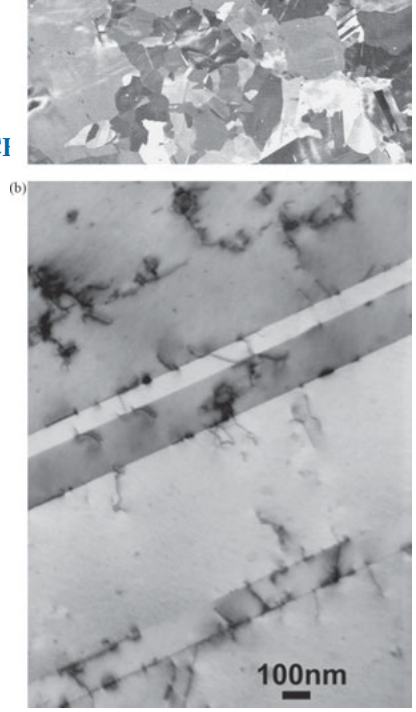

Figure 4.12: TEM micrograph showing annealing twins as well as dislocation structures in [221] monocrystalline copper shocked to 57 GPa [304].

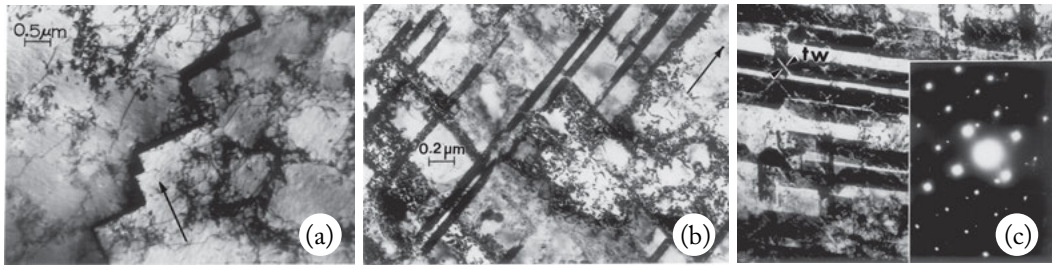

Figure 4.13: TEM micrographs of (a) as-received coarse-grained Ni consisting of poorly formed dislocation cells, (b) coarse-grained Ni shock compressed to 30 GPa consisting of deformation microtwins, and (c) coarse-grained Ni shock compressed to 45 GPa showing higher density of deformation microtwins [309]. Note that the scale bar in (b) and (c) are the same.

Ni is shock compressed to 45 GPa, above the critical stress required for deformation twinning, the density of deformation microtwins increases significantly (Figure 4.13c) [297]. The microstructural response of nanocrystalline (NC) Ni was quite different from coarse-grained Ni when compressed up to 70 GPa shock stress. The results show that dislocations were the dominant deformation mechanism in NC Ni [310]. No deformation twins were observed on the residual substructure as shown in Figure 4.14 although the stresses were more than twice the threshold required for deformation twinning in coarse-grained polycrystalline Ni. These results

suggest that deformation twinning might be an arduous process in nanocrystalline Ni undergoing shock compression [310].

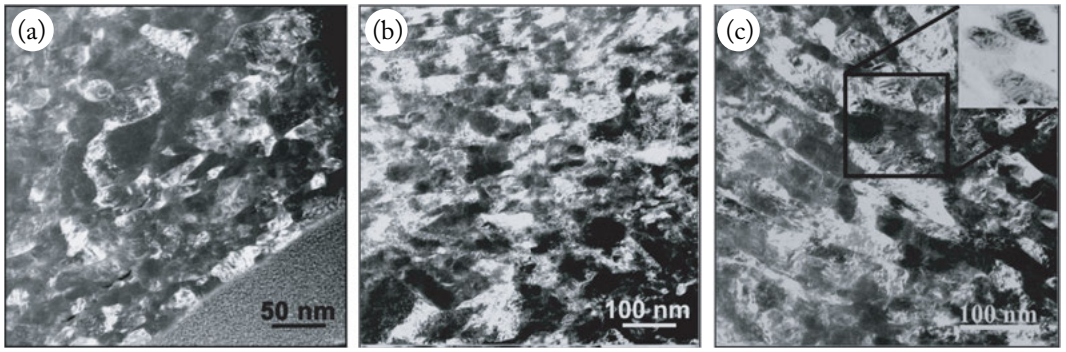

Figure 4.14: TEM micrographs of (a) as-received NC Ni with an average grain size of 30–50 nm, (b) residual substructure of NC Ni after 20 GPa shock stress, and (c) residual substructure of NC Ni after 40 GPa shock stress [310].

4.2.2 SUBSTRUCTURE IN SHOCK-COMPRESSED METALS WITH BCC LATTICE STRUCTURE

The plastic response of BCC metals such as α-iron, molybdenum, niobium, tungsten, tantalum, vanadium, and chromium is different from their FCC and HCP counterparts because of their high Peierls-Nabarro stress. The Peierls–Nabarro stress is the primary short-range barrier for BCC metals and it is 10 times greater for screw dislocations than that of non-screw dislocations [314]. The flow stress is strongly temperature dependent in BCC metals because of the high Peierls–Nabarro stress and, therefore, at low temperatures and/or at high strain rates, high stresses are required to move screw dislocations. Although deformation slip is the preferred mode to accommodate plasticity for a wide range of temperatures at low strain rates for BCC metals, deformation twinning becomes more prevalent at low temperatures and high strain rates; at low temperatures, the stress required for deformation twinning is less than that required for deformation slip [315]. The shock compressed behavior of some metals with BCC lattice structure has gained significant research interests over the past few decades because of their applications in ballistics and nuclear weapons [70–72, 118, 316–322].

Hsiung and Lassila [71, 316–318, 323] conducted comprehensive research studies on the substructure evolution in tantalum and tantalum (Ta)-tungsten (W) alloys shock compressed to high stresses. At a shock stress of 45 GPa and pulse duration of 1.8 μs, they observed for the first time a displacive shock-induced phase transformation from β (BCC) to ω (hexagonal) in polycrystalline tantalum [316]. Furthermore, Hsiung and Lassila [71] investigated the residual substructures developed in single crystal Ta, polycrystalline Ta, and polycrystalline Ta-W

alloys shock compressed to 15 GPa and 45 GPa, respectively. They identified two alternative paths for shock-induced shear transformations in the polycrystalline samples, i.e., $\{\bar{2}11\}\langle 111\rangle$ deformation twinning and omega transformation. Although deformation twins were observed in samples shock compressed to 15 GPa and 45 GPa, respectively, the shock-induced omega phase was only present in samples shock compressed to 45 GPa. The residual substructures also reveal a higher volume fraction of the omega phase in Ta-W alloys than in pure Ta which suggests that deformation twinning and omega transformation are facilitated by solid solution alloying. The residual substructure of the [011] single-crystal Ta shock compressed to 45 GPa exhibited neither deformation twins nor an omega phase possibly due to the relatively low dislocation density. Figure 4.15 shows the residual substructures of the single-crystal Ta, polycrystalline Ta, and polycrystalline Ta alloy shock compressed to 45 GPa.

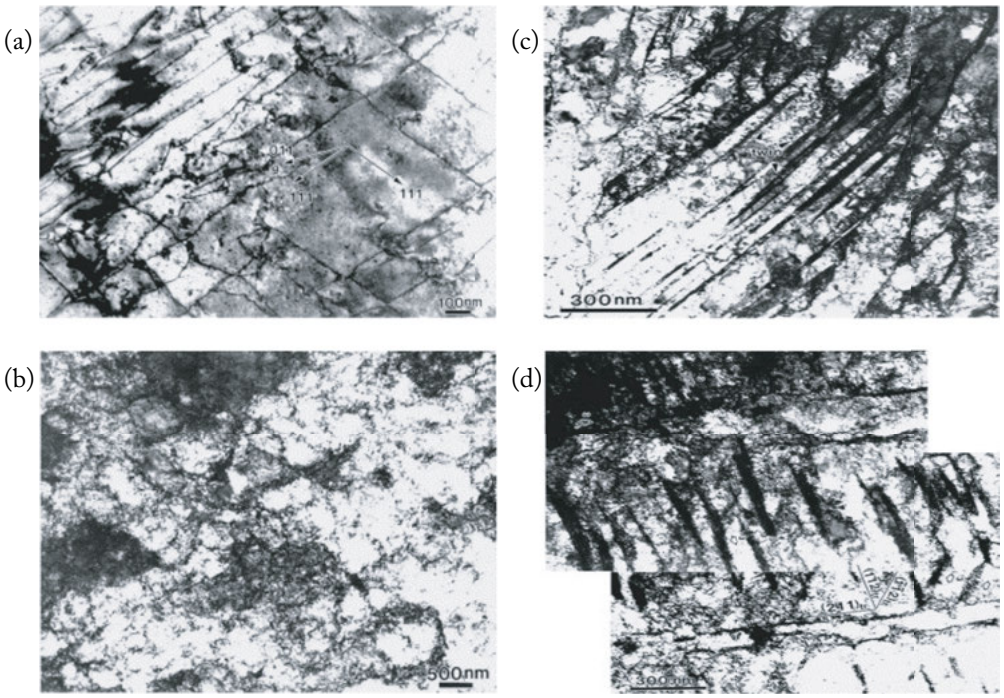

Figure 4.15: TEM images showing the residual substructures of (a) [011] single-crystal Ta with dislocation structures, (b) polycrystalline Ta with dislocation structures, (c) long twin lamellae in polycrystalline Ta-10W alloy, and (d) short omega plates observed in polycrystalline Ta-10W alloy; all shock compressed to 45 GPa [71].

Since the pioneering observation of polymorphic phase transformation in shock-compressed Iron from α-phase (BCC) to ϵ-phase (HCP) by Bancroft et al. [324] in 1956, followed by the elegant research by C. S. Smith [5] on the metallographic studies of α-Iron af-

ter the passage of an explosive shock in 1958, a comprehensive understanding of the α to ϵ phase transformation (polymorphic and allotropic) in iron and some steels became of great interest to materials scientists and engineers. For instance, Dougherty et al. [325] studied the quasi-static and dynamic shear response of as-received and shock-prestrained 1018 steel at room temperature to determine the influence of shock-prestraining on the shear behavior of ferrite. They shock compressed 1018 steel samples up to 12.5 GPa (below the phase transformation stress which is 13.0 GPa) and 14.0 GPa (above the phase transformation stress), respectively, and observed deformation twins and microbands only in the residual substructure of the shock-prestrained samples as shown in Figure 4.16. Subsequent quasi-static compression experiments showed an increase in yield and compressive strengths as a function of peak shock stress. All the samples subjected to dynamic shear produced shear localization, with the shear band occurring only in the shock-prestrained samples. They found at the shear band edge, elongated cells dominate the microstructure, with more shock-induced twins remaining intact in the 12.5 GPa sample than in the 14.0 GPa sample.

The microstructural fingerprints of the $\alpha \rightarrow \epsilon \rightarrow \alpha$ polymorphic phase transformation in iron have been detected and deciphered by Wang et al. [326]. From shock recovery experiments, they were able to determine that the residual microstructure (characteristic morphologies) in shock compressed iron consists of needle-like colonies and three sets of $\{112\}\langle 111\rangle$ twins with a threefold symmetry (see Figure 4.17). As shown in Figure 4.17a the presence of numerous needle-like regions with twin lamellae within them are evident and they form networks which divide the original single α-grain into many blocks. From this evidence, Wang et al. [326] were able to isolate areas that have undergone martensitic phase transformation from those that have not in the post-shock recovered samples. Wang et al. [326] were also able to quantify and evaluate the volume percentage of the transient ϵ-phase formed at different areas in the residual microstructure of the polycrystalline sample at different shock stresses.

Shock recovery experiments were conducted by Huang and Gray [320] to develop a better understanding of the substructure evolution and deformation modes in polycrystalline niobium shock compressed to 6.0 GPa and 37.0 GPa, respectively. They observed profuse dense dislocation tangles and loops within the residual substructure of the sample shock compressed to 6 GPa (see Figure 4.18). However, the residual substructure of the recovered sample shock compressed to 37.0 GPa comprises of slip bands and microbands on the $\{110\}$ crystallographic planes and deformation twins on the $\{112\}$ twinning planes in addition to dislocation tangles and loops (see Figure 4.19). The deformation twins they observed possess the characteristic lenticular shape reminiscent to those observed in shock compressed molybdenum which are consistent with the shape predicted by existing deformation twinning models. Huang and Gray [320] established that the deformation twinning elements and characters were not different from those induced by other conventional deformation loading configurations at low strain rates. The resulting slip bands on $\{110\}$ crystallographic planes were determined to result from an independent deformation mode which is not a consequence of the termination of twin growth within the crystal. The

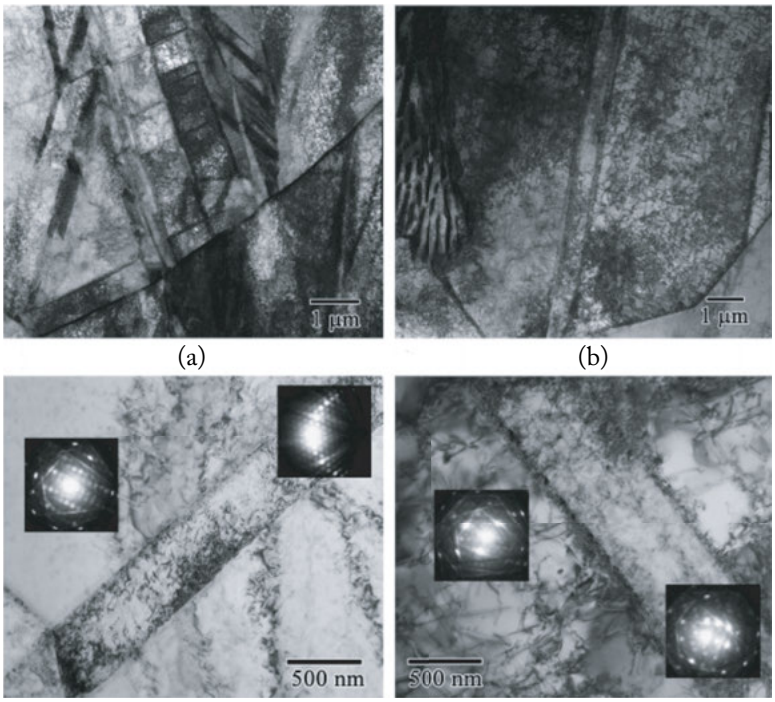

Figure 4.16: TEM micrographs revealing twins and microbands in 1018 steel shock compressed to 12.5 GPa (a,c) and 14.0 GPa (b,d). Although the band-like features in (c) and (d) appear similar to microbands, they were determined to be twins as determined through convergent beam electron diffraction (CBED) [325].

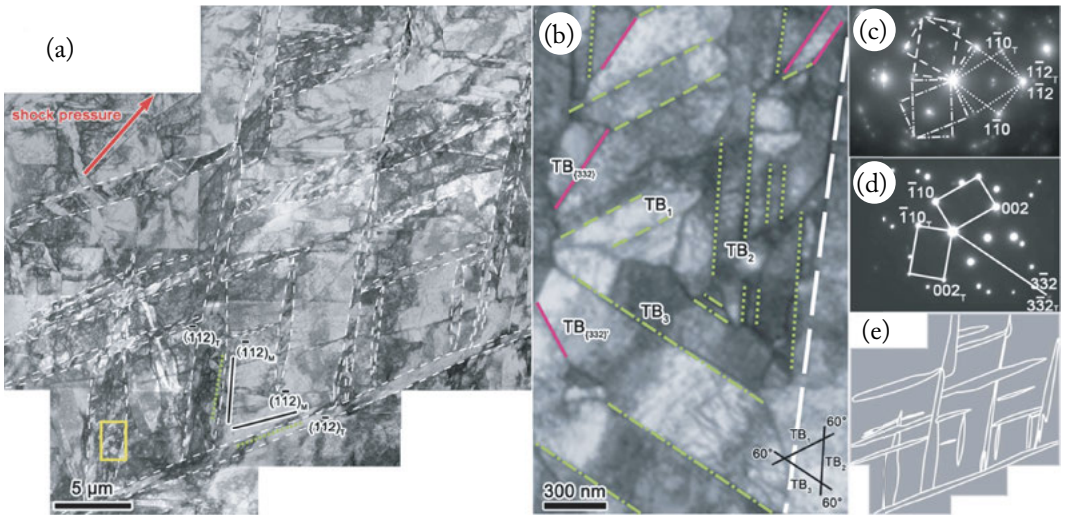

Figure 4.17: Microstructural fingerprints of phase transformation in shock compressed Fe. (a) TEM micrograph revealing the microstructure of shock compressed Fe. (b) An enlarged view of the yellow rectangle box in (a) where TB_1, TB_2, and TB_3 (dashed, dotted, and dash-dot green lines) represent three sets of {112} twins; T_{332} and $T_{(332)'}$ (pink solid lines) for two sets of {332} twins. The triangle with black solid lines reveals the angle of the three sets of $\{112\}_{bcc}$ twins. (c) Selected area electron diffraction (SAED) of the three sets of {112} twins. (d) SAED of T_{332} twins. (e) Contours of the boundaries of needle-type-martensite-like regions in (a) (white dashed lines) [326].

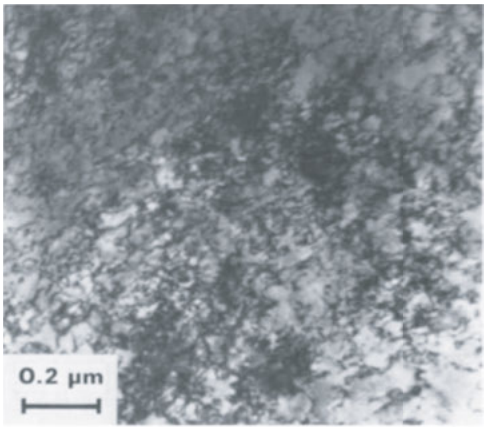

Figure 4.18: Bright field electron micrograph of the typical dislocation substructure developed in niobium shock compressed to 6 GPa [320].

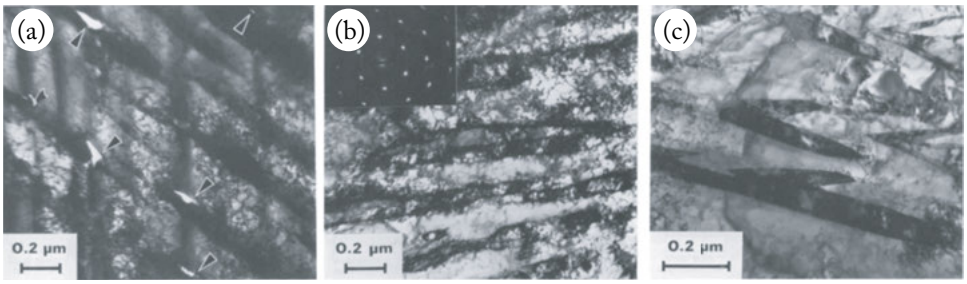

Figure 4.19: Bright field electron micrographs showing (a) microcracks formed at the intersections of two cross-linking slip bands on {110} planes, (b) microbands lying within 10° of {110} planes, and (c) two variants of cross-linking twins in the sample shock compressed to 37 GPa [320].

profuse microbands observed in the residual substructure of the recovered sample shock compressed to 37.0 GPa were developed within 10° of {110} crystallographic planes with a slight misorientation (1° or less) across the bands. Neither of the shock compressed samples exhibited macroscopic shear bands and the residual microstructures resulting from both shock compressed samples and samples deformed at low rate did not exhibit any significant difference. Therefore, Huang and Gray [320] concluded that the prevalent deformation modes in shock compressed niobium are not significantly different from other conventional deformation modes.

4.2.3 SUBSTRUCTURE IN SHOCK-COMPRESSED METALS WITH HCP LATTICE STRUCTURE

Deformation twinning is more prevalent in low symmetry crystal structures such as in HCP metals and metallic alloys where the number of available slip systems is low relative to their FCC and BCC counterparts. HCP metals and metallic alloys are similar to BCC metals, in that, when the strain rate is increased as in the case for shock compression and/or temperature is decreased as in the case for cryogenic temperatures, the rate of deformation twinning increases [23, 55, 96, 315, 327–335]. The crystallographic texture and c/a ratio of the HCP metal or metallic alloy are also influential on whether extension or contraction deformation twins are formed. Deformation twinning is responsible for the hardening and texture evolution characteristics during plastic deformation in HCP metals and metallic alloys.

Because of its superior properties (ductility, strength, corrosion and irradiation resistance, etc.), zirconium is widely used in nuclear reactors and as a solid-solution strengthener in superalloys used in aircraft turbine engines. Traditionally, the effects of shock waves on the structure-property relationships in HCP metals and metallic alloys such as zirconium have been focused on the influence of peak shock stress and pulse duration on the residual substructure and substructure evolution [336–338]. However, Cerreta et al. [60] employed a different approach by studying the influence of interstitial oxygen on the shock response and shock prestraining on the dynamic response of zirconium. They quantified the phase transformation stress as a function of the interstitial oxygen content and found that the phase transformation stress increases with increasing interstitial oxygen content. The $\alpha - \omega$ phase transformation stresses for the high-purity and low-purity zirconium were determined to be 7.1 GPa and 8.3 GPa, respectively. With further increases in the interstitial oxygen content, the $\alpha - \omega$ phase transformation was completely suppressed in zirconium shock compressed to the same stress. Cerreta et al. [60] postulated that by increasing the interstitial oxygen content, the number of octahedral sites occupied increases and, therefore, the $\alpha - \omega$ phase transformation stress increases.

High-purity zirconium samples were further shock compressed to 5.8 GPa (below the phase transformation stress) and 8.0 GPa (above the phase transformation stress) for 1 μs pulse duration, respectively, and recovered. Through substructure analysis, Cerreta et al. [60] determined that the residual substructure of the sample shock compressed to 5.8 GPa exhibited a very high dislocation density with tangled and free gliding $\langle c + a \rangle$ type dislocations throughout the grain (see Figure 4.20). They also observed a small volume fraction of twins on the $(01\bar{1}2)$ and $(11\bar{2}1)$ planes. Note that the substructure of the as-annealed material contained few dislocations and was mostly free of defects within the grain interior.

On the other hand, the residual substructure of the material shock compressed to 8.0 GPa exhibited the α-phase with very high density of both $\langle a \rangle$ and $\langle c + a \rangle$ type dislocations gliding on prism and pyramidal planes which led to a highly tangled dislocation substructure. They observed numerous grains with clusters of thin $(01\bar{1}2)$ extension twins which were populated with a high density of $\langle a \rangle$ type dislocations, as shown in Figure 4.211a. In other areas of the shock

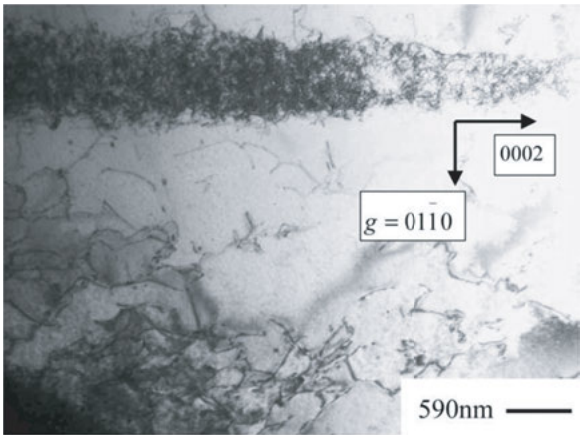

Figure 4.20: Bright field TEM image of the substructure of the 5.8 GPa shock recovered sample. Note that the as-received material was free of highly tangled dislocations [60].

recovered sample, the grains exhibited a high contrast substructure associated with high strains and high dislocations densities. The phases and orientations in these areas were identified to be $[\bar{2}11\bar{3}]\omega$ and $[\bar{1}010]\alpha$ zone axes, respectively, as shown in Figures 4.212a, 2b. Cerreta et al. [60] determined that the quasi-static response of the as-received and shock recovered zirconium samples clearly exhibited a shock hardening behavior which they attributed to the shock induced residual substructure.

The approach used by Cerreta et al. [60] to study zirconium was employed to study the influence of oxygen content on the α to ω phase transformation and shock hardening behavior in high purity α-titanium and A-70 AMS 4921 titanium alloy [64]. The α to ω phase transformation stress was determined to be 10.4 GPa for the high purity α-titanium, while the A-70 AMS 4921 titanium alloy did not undergo phase transformation when shock compressed up to 35.0 GPa. Similar to zirconium, Cerreta et al. [64] found that by increasing the interstitial oxygen content, the $\alpha - \omega$ phase transformation was completely suppressed in the A-70 AMS 4921 titanium alloy shock compressed to 35.0 GPa. According to Cerreta et al. [64], the substructure of the as-received high purity α-titanium revealed few dislocations but when shock compressed to 11.0 GPa, the residual substructure revealed a high dislocation and twin density. The dislocations were observed to reside within the deformation twins and also, within the matrix titanium. As shown in Figure 4.2211a and Figure 4.2211b, respectively, the residual substructure of the high-purity α-Ti shock compressed to 11 GPa also reveal both the α and ω phases. On the other hand, the residual substructure of the A-70 AMS 4921 titanium alloy shock compressed to 11 GPa revealed planar slip and deformation twins but no evidence of the α and ω phases. The aforementioned residual substructures in both high-purity α-Ti and

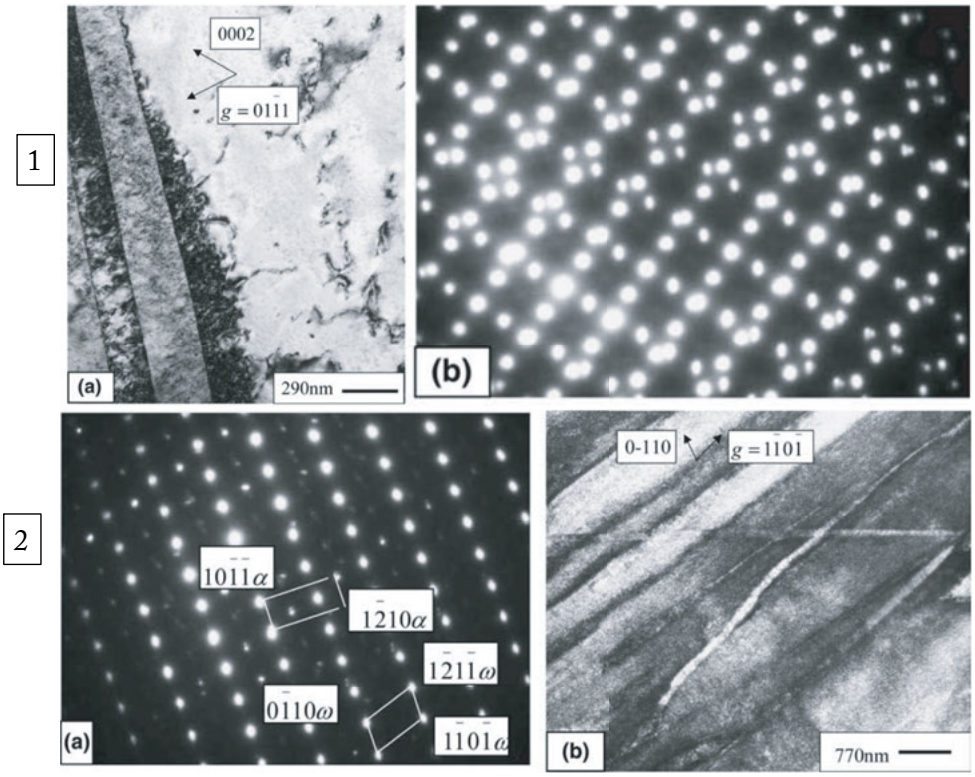

Figure 4.21: (1a) Bright field TEM image of the 8 GPa shock compressed α-phase showing $(01\bar{1}2)$ extension twins within the substructure. (1b) The resulting diffraction pattern for a twin on the $(01\bar{1}2)$ plane and the matrix. (2a) Diffraction pattern for the $[\bar{2}11\bar{3}]\omega$ and $[\bar{1}010]\alpha$ zone axes. (2b) Bright field TEM image of ω-phase in the 8 GPa shock-compressed sample [60].

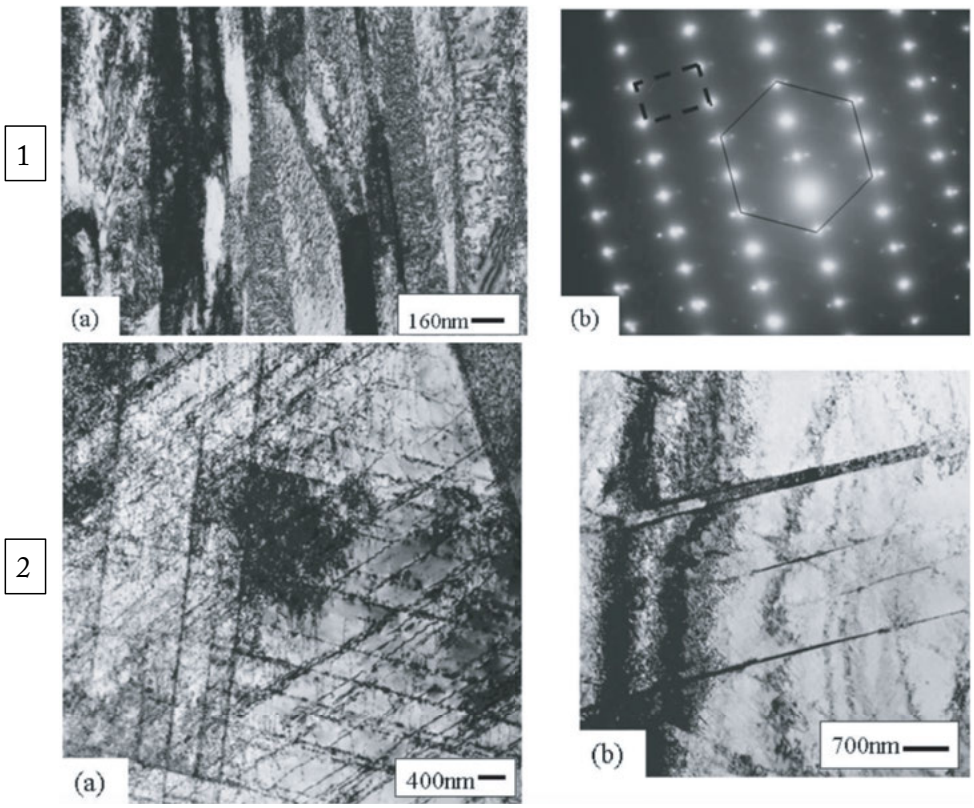

Figure 4.22: Bright field TEM images of (1a) an area containing both the α and ω phases present in the high purity α-Ti shock compressed to 11 GPa and (1b) the corresponding diffraction pattern for the $(0001)_\alpha$ (represented by a solid line (-)), and the $[\bar{1}2\bar{1}0]_\omega$ (represented by a dashed line (- -)). Bright field TEM images (2a) revealing planar slip and (2b) revealing twins within the A-70 AMS 4921 titanium alloy shock compressed to 11 GPa [64].

A-70 AMS 4921 titanium alloy shock compressed to 11 GPa are responsible for the different quasi-static behavior of both materials according to Cerreta et al. [64].

4.3 FAILURE MECHANISMS AND SPALLATION IN SHOCK COMPRESSED METALS

Failure following shock compression can take numerous forms; the most prevalent form is spallation. Spallation is the separation of a material resulting from very rapid tensile loading and for ductile materials it is a process that generally involves the nucleation, growth, and coalescence of nanoscale or microscale voids that result in macroscopic material failure by separation. For example, Curran et al. [150] showed that void nucleation generally initiates at a relatively low tensile stress level (incipient spall) and depends on the substructure, microstructure, mechanical and material properties, and tensile loading history of the material involved. The spall process is further complicated by the fact that the material first undergoes shock compression which may change the as-received substructure and microstructure of the material prior to tensile loading. Depending on the magnitude of the preceding shock stress, large amounts of defects such as dislocations, deformation twins, stacking faults, etc., can be introduced in the material and can lead to significant changes in material and mechanical properties prior to the tensile load or spall pulse [6, 265, 339].

Shock compression can also increase the number of point defects such as vacancies, vacancy clusters, and interstitials resulting primarily from the non-conservative motion of jogs [313]. Vacancy clusters are known to be potential void nucleation sites. An increase in potential void nucleation sites prior to tensile loading can effectively accelerate spallation and can lead to the reduction of spall strength. The spall strength of a material is potentially dependent on several competing mechanisms such as dislocation generation, dislocation annihilation, generation of potential void nucleation sites, temperature rise, substructure evolution, and microstructure evolution prior to tensile unloading. As a consequence of such mechanisms, the spall strength of a material is expected to strongly depend on the peak shock stress, pulse duration, initial temperature, tensile unloading rate, and initial microstructure [55, 133, 134, 138, 139, 266, 290, 340–342, 342–346]. However, a review of the open literature shows inconsistent results for spall strength dependence on peak shock stress [139, 340, 347] which points to the complexities involved during spallation.

For ductile metals, the nucleation of voids is generally classified as homogeneous or heterogeneous [19, 262, 348]. Voids nucleating from submicron heterogeneities such as dislocation tangles and networks, low angle grain boundaries, and fine impurities are referred to as homogeneous; those nucleating from larger than submicron heterogeneities such as inclusions and second-phase particles are referred to as heterogeneous. The stress required for homogeneous nucleation of voids is higher than that required for heterogeneous nucleation and, therefore, heterogeneities such as second-phase particles are favored void nucleation sites. Nevertheless, if the stress is high enough, both homogeneous and heterogeneous nucleation can be activated

simultaneously. The nucleated voids then grow and coalesce to form macrocracks and then consequent failure of the material. Sections 4.2.1, 4.2.2, and 4.2.3 concern the substructures developed in shock compressed metals with FCC, BCC, and HCP lattice structures, respectively. Sections 4.3.1, 4.3.2, and 4.3.3 will concern the spall failure in metals with FCC, BCC, and HCP lattice structures, respectively, following shock compression at the microscale, mesoscale, and macroscale.

4.3.1 SPALLATION IN METALS WITH FCC LATTICE STRUCTURE

The substructure and microstructure of shock compressed FCC metals and metallic alloys have been extensively studied through plate impact recovery experiments [23, 139, 236, 302, 342, 349–354]. These experiments have been used for several decades to examine the structure-property relationships under uniaxial strain conditions. For instance, Williams et al. [138, 139, 236] conducted a comprehensive study on 1100 commercially pure aluminum to develop a better understanding of the governing fundamental structure-property relationships under shock compression.

Williams et al. [138] conducted time-resolved in-situ spall experiments and show that the spall strength of 1100-O aluminum increased between 4 GPa and 8.3 GPa, then decreased thereafter. From shock recovery experiments, they determined that the as-received substructure of the 1100-O aluminum evolves substantially between 4 GPa and 9 GPa (see Figure 4.3). This observation in conjunction with results acquired from spall recovery experiments (see Figure 4.23) suggest that the material shock hardened, and ductile fracture by void nucleation, growth, and coalescence was the dominant fracture mode for shock stresses up to approximately 8.3 GPa. Whereas, beyond 8.3 GPa the material shock softened possibly due to reorganization of the substructure (dynamic recovery), and brittle intergranular fracture by decohesion along lamellar boundaries forming flat surfaces was the dominant fracture mode, as shown in Figure 4.24. Isolated pockets of nanovoids were observed on the fracture surface but their contributions to the dynamic recovery and fracture processes were unresolved. Microhardness measurements show an increase in residual hardness throughout the shock stress range studied, validating that the material shock hardened up to approximately 8.3 GPa but also suggest that thermal softening was not operative throughout the shock stress range studied. However, dynamic recovery was thermally influenced during shock loading.

Both symmetric real-time (in situ) and end-state (ex-situ recovery) plate impact shock experiments were conducted by Williams et al. [141] to study the spall response and role of second phase intermetallic particles on the spall properties of both 5083-H321 and 5083-ECAE + 30% cold-rolled (CR) aluminum alloys. The results from real-time plate impact experiments show that, by mechanically processing 5083-H321 aluminum using Equal Channel Angular Extrusion (ECAE) and then subsequently CR to 30% reduction in height, the average Hugoniot Elastic Limit (HEL) increases by 78%. However, this significant improvement on the dynamic yield strength under uniaxial strain conditions (HEL) was not realized for spallation. The in-

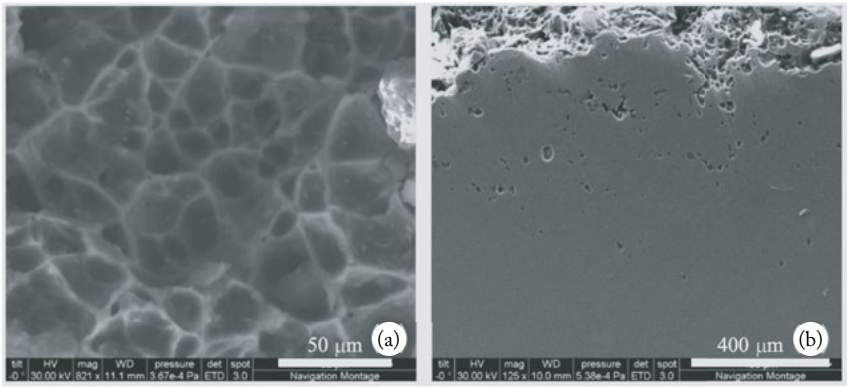

Figure 4.23: SEM micrographs of the 1100-O aluminum shock compressed to 6 GPa showing (a) dimples on the fracture surface and (b) the cross-sectional view of the fractured sample showing voids below the spall plane [236].

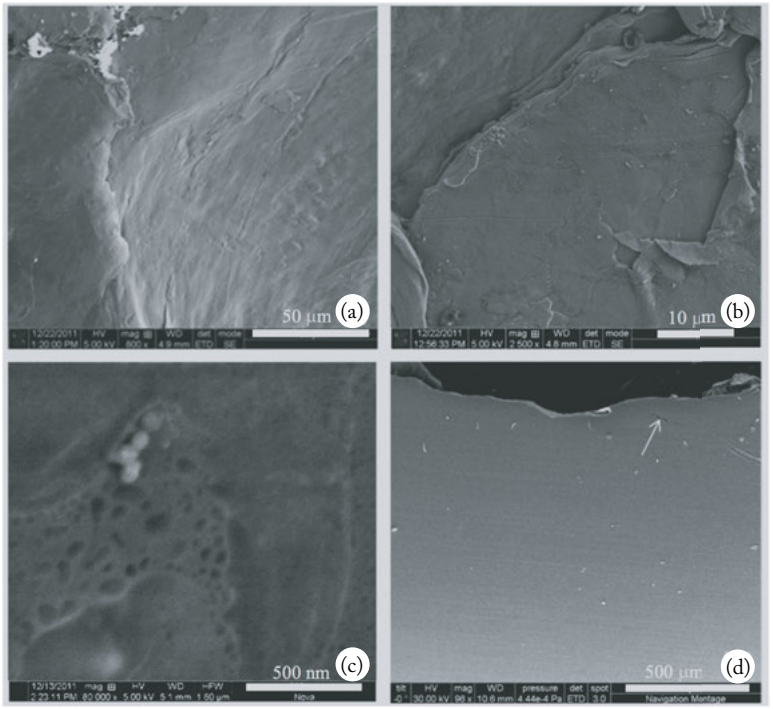

Figure 4.24: SEM micrographs of the 1100-O aluminum shock compressed to 9 GPa showing (a) intergranular spall fracture surface, (b) an enlarged view of the intergranular spall fracture surface with tongues, (c) nanovoids in isolated areas of the fracture surface, and (d) the cross-sectional view of the fractured sample [236].

situ spall results show no significant change in the spall strength of 5083-H321 aluminum shock compressed to 1.45 GPa and 2.88 GPa shock stress, respectively. On the other hand, the spall strength of the 5083-ECAE + 30% CR aluminum shock compressed to the same stress levels decreased by 37% and 23%, respectively, when compared to their 5083-H321 aluminum counterpart. Moreover, end-state shock recovery experimental results show that the second phase intermetallic Mn-Fe rich particles de-bonded from the aluminum matrix during shock compression and were potential void nucleation sites in both materials. The ex-situ shock recovery results also show that spallation occurs in both materials by void nucleation, growth, and coalescence. However, the overwhelming evidence shows that spall failure occurs along the re-aligned intermetallic Mn-Fe rich particles for the 5083-ECAE + 30% CR aluminum and this perhaps is responsible for the reduction in spall strength as a function of peak shock stress. As revealed in Figure 4.25a, the resulting spall plane in the 5083-H321 aluminum is highly localized, while that of the 5083-ECAE + 30% CR aluminum meanders across a wide damage zone consisting of multiple cracks as shown in Figure 4.25b. The dominant failure characteristic for 5083-H321 aluminum was mixed-mode (ductile-brittle), emanating from homogeneous and heterogeneous nucleation of voids, as shown in Figure 4.26.

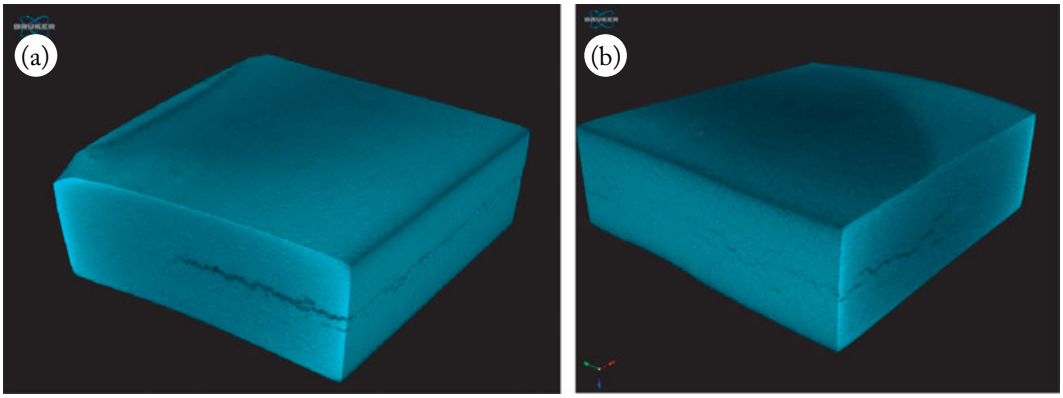

Figure 4.25: X-ray microCT scans of soft recovered (a) 5083-H321aluminum and (b) 5083-ECAE + 30% CR aluminum samples shock compressed to approximately 1.46 GPa [141].

Simultaneous time-resolved in-situ spall experiments and spall recovery experiments were conducted by Wang et al. [349] to study the effects of microstructure on the spall strength of four different types of aluminum (high purity, low porosity, 2024-T4, and 7075-T6). They determined that the high-density, high-purity aluminum (Al HP) has a higher spall strength than the low-porosity pure aluminum but the 2024-T4 aluminum exhibited the highest spall strength of all the aluminum studied followed by the 7075-T6 aluminum. From metallographic analyses of the shock recovered samples, they attributed these findings to the lower number of impurities at the grain boundaries in the Al HP samples compared to those observed in the low

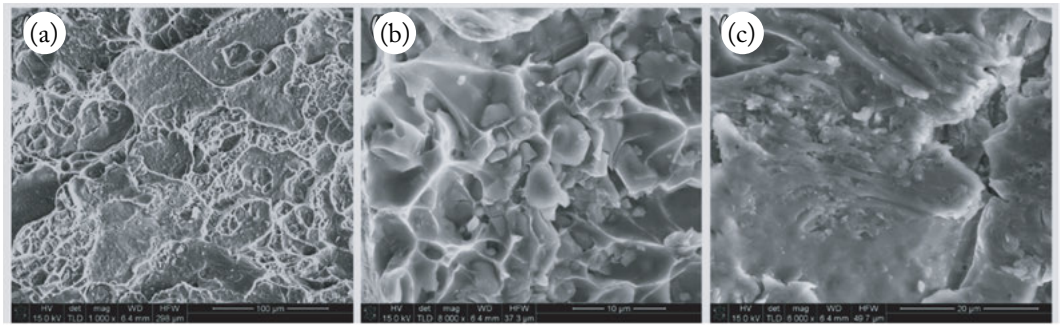

Figure 4.26: SEM micrographs of the fracture surface of 5083-H321 aluminum sample shock compressed to approximately 2.96 GPa. (a) Areas consisting of dimples resulting from void nucleation, growth, and coalescence with isolated areas of brittle fracture, (b) second-phase Mn-Fe rich particles within the void dimples, and (c) smooth brittle-like surface [141].

porosity pure aluminum. They concluded that the low number of impurities at the grain boundaries led to an improved resistance to void nucleation. As shown in Figure 4.27a, relatively low amounts of micro-voids are nucleated in the Al HP aluminum, which then grow but do not generally coalesce; whereas, for higher impact velocities, the micro-voids grow then coalesce to form major cracks and consequently spall fracture (see Figure 4.27b,c). Figure 4.28 shows the micrographs of the (a) as-received AL HP and (b) that recovered from the 246 m/s impact velocity. Figure 4.28b clearly reveals that the micro-voids primarily nucleate and grow along grain boundaries. On the other hand, Wang et al. [349] from spall recovery experiments conducted at approximately 300 m/s on 2024-T4 and 7075-T6 aluminum, respectively, were able to show that the vast majority of microvoids and/or cracks were heterogeneously nucleated at second phase particles by particle-matrix debonding at the interface, as shown in Figure 4.29a,b.

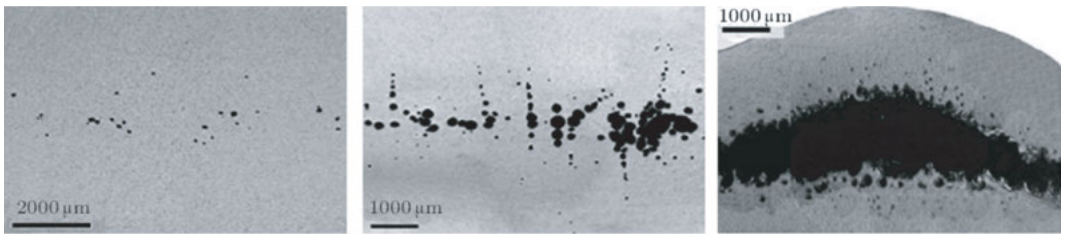

(a) (b) (c)

Figure 4.27: Optical micrographs of the cross-sectional views of the spall-recovered Al HP samples at various impact velocities; (a) 150 m/s, (b) 246 m/s, and (c) 302 m/s [349].

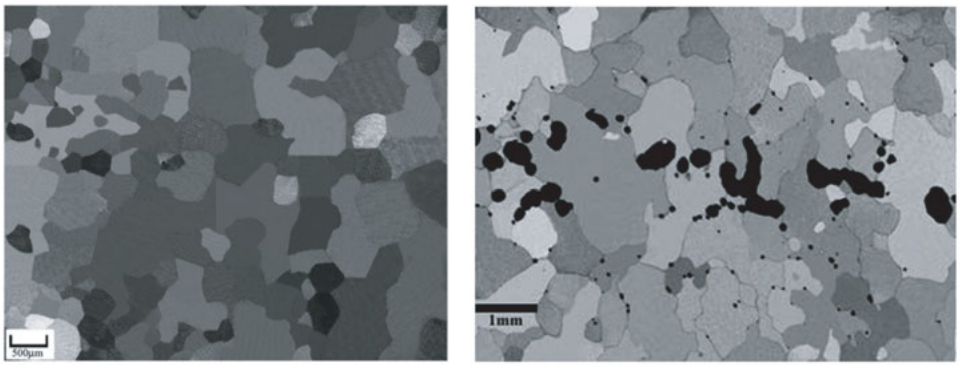

(a) (b)

Figure 4.28: Optical micrographs of the cross sectional views of (a) the as-received microstructure of Al HP material and (b) spall-recovered Al HP sample at an impact velocity of 246 m/s [349].

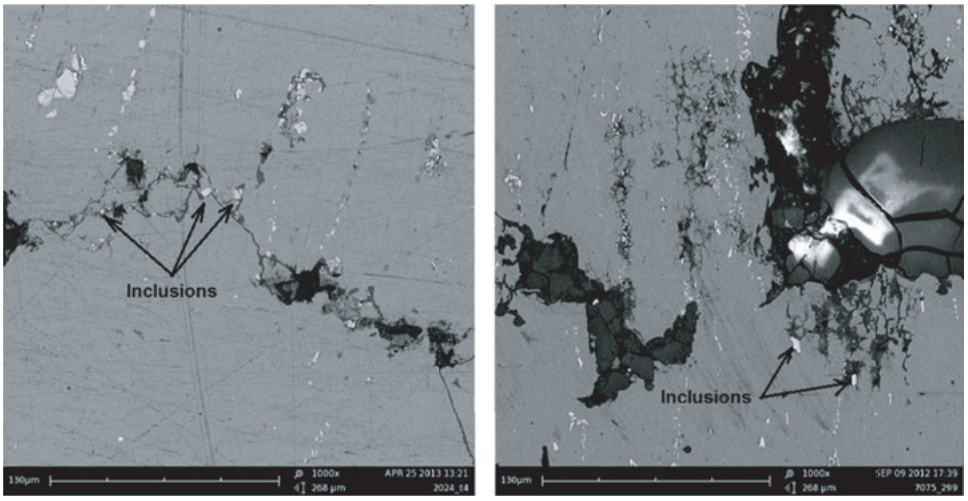

(a) (b)

Figure 4.29: SEM micrographs of the cross-sectional view of recovered samples (a) 2024-T4 and (b) 7075-T6 at an impact velocity of approximately 300 m/s [349].

The effects of microstructure on the spall fracture morphology in high-purity and low-impurity aluminum samples were studied by Brewer et al. [355] using laser-shock-induced spall failure at strain rates ranging from 2×10^6 s^{-1} to 5×10^6 s^{-1}. Their samples were fabricated from high-purity aluminum in the recrystallized form and a low-impurity aluminum alloy containing 3 %wt magnesium in both recrystallized and cold-rolled forms. Their results clearly show that the shock-compressed recrystallized pure aluminum exhibited spall fracture surfaces characterized by transgranular ductile dimpling as shown in Figures 4.30a,b. Moreover, the recrystallized aluminum-magnesium alloy with a 50 μm grain size exhibited less ductile spall surfaces, which were dominated by transgranular fracture, with some isolated transgranular ductile dimpling at the higher strain rates (see Figures 4.30c–f). Transgranular ductile dimpling regions were not evident in the recrystallized alloy samples with an average grain size of approximately 23 μm which were spalled at higher rates. The cold-rolled alloy samples exhibited spall failure surfaces consisting of brittle intergranular and transgranular fractures (see Figure 4.30g). Brewer et al. [355] correlated the acquired spall strengths to the resulting spall morphologies and determined that the measured spall strength increases with increasing ductile fracture character, and spall failure preferentially follows grain boundaries as revealed in Figure 4.31, making grain size an important factor in spall failure characteristic and fracture surface morphology.

Peralta et al. [351] studied the correlation between spall damage and local microstructure in multicrystalline copper samples using laser-driven plate impact recovery experiments at shock stresses ranging from 2–6 GPa. In order to isolate the effects of microstructure on the local response, they utilized microstructures with large grains relative to the thicknesses of the samples which were 200 μm and 1000 μm, respectively. Using Electron Backscattering Diffraction (EBSD) analyses, Peralta et al. [351] were able to correlate crystallographic orientations to porosity around microstructural features such as grain boundaries and triple points. Using this methodology, they determined that for thin samples with an average grain size of approximately 230 μm where the porosity appears in proximity to grain boundaries, transgranular damage was dominant (see Figure 4.32a,b). However, when the grain size was reduced to 150 μm, the dominant damage mode transitioned from transgranular to intergranular. Their analyses also show that thick samples with an average grain size of approximately 450 μm exhibited both modes (see Figure 4.32c,d). Intergranular damage was observed mostly in areas where the grains were smaller than average and preferred nucleation sites include grain boundaries and triple points. Also, strong damage localization was observed at the tip of deformation twins which terminate at grain boundaries that are approximately parallel to the shock direction shown in Figure 4.32c,d.

Peralta et al. [351] concluded that the cause for this strong influence on the damage mode includes impedance and spall strength mismatches across grain boundaries, original density of defects, along with a possible interplay between grain size and pulse duration for which changes in damage mode can occur provided the local value of grain size is smaller than a characteristic length scale which is the product of the shock velocity and the pulse duration.

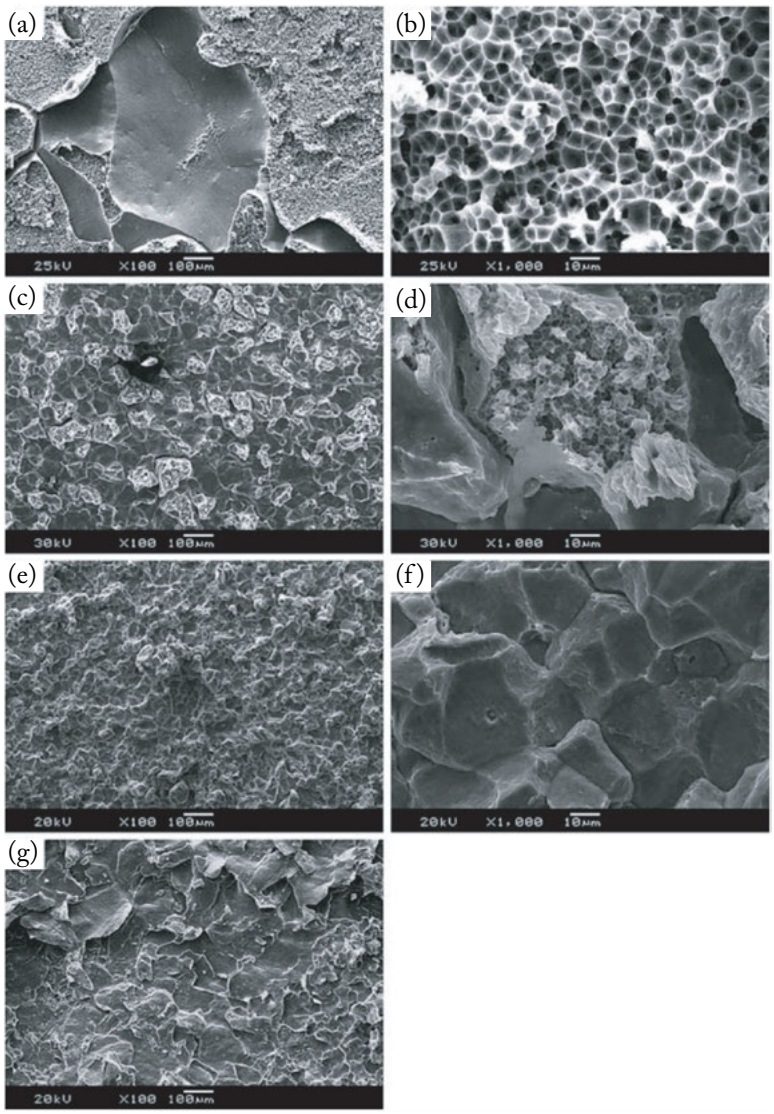

Figure 4.30: Spall failure surface features at low (left column) and high (right column) magnifications for (a) and (b) Al HP 500 μm, (c) and (d) AlMg RX 200 μm, (e) and (f) AlMg RX 500 μm, and (g) AlMg CR 500 μm targets [355].

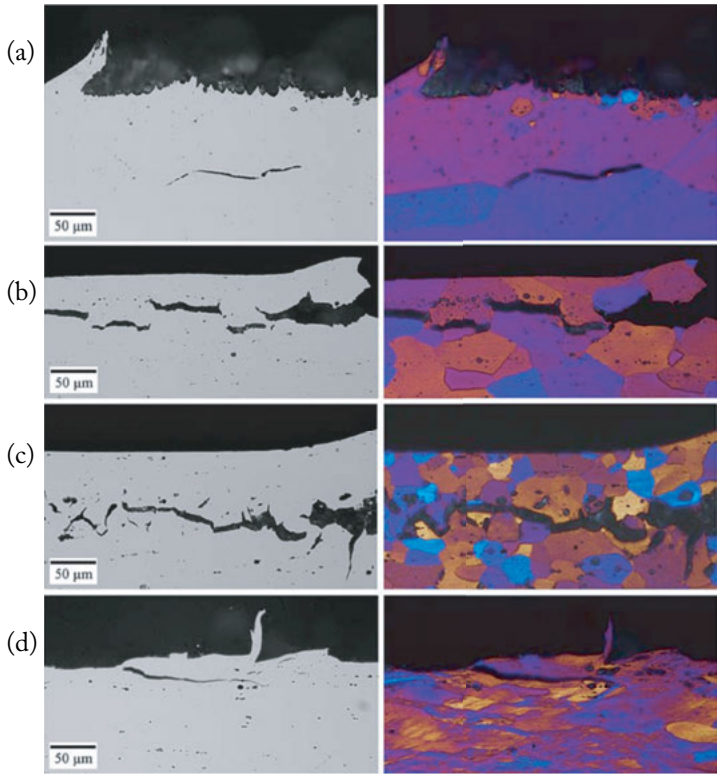

Figure 4.31: Optical micrographs of unetched (left column) and etched (right column) cross sections of the same area are shown for (a) Al HP 500 μm, (b) AlMg RX 200 μm, (c) AlMg RX 500 μm, and (d) AlMg CR 500 μm targets. The free surface of the target is at the top of each image [355].

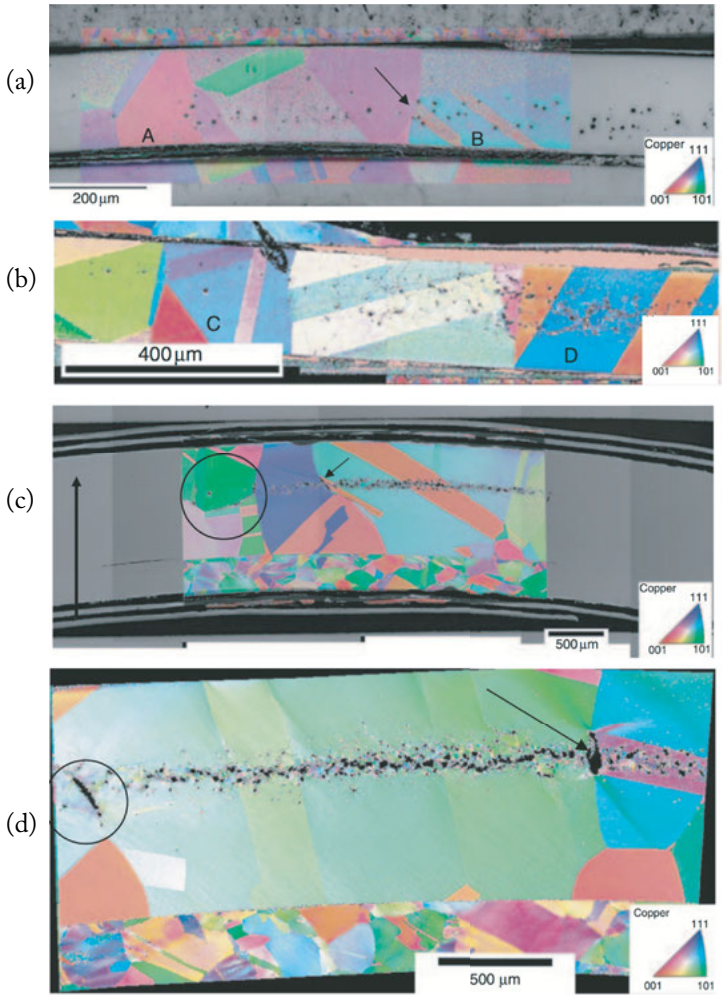

Figure 4.32: EBSD inverse pole figure maps of recovered multicrystalline copper samples (a) ~200 μm thick shock compressed to >2.6 GPa, (b) ~200 μm thick shock compressed to ~4.6 GPa, (c) ~1000 μm thick shock compressed to ~4.6 GPa, and (d) ~1000 μm thick shock compressed to ~4.8 GPa [351].

4.3.2 SPALLATION IN METALS WITH BCC LATTICE STRUCTURE

Over the past few decades, shock compression scientists and engineers have compiled a considerable amount of data on the substructure and microstructure evolution in shock compressed metals and metallics alloys with BCC lattice structure because of their importance in ballistics and nuclear weapons. Consequently, the effects of substructure and microstructure evo-

lution on the spall behavior of metals and metallic alloys with BCC lattice structure have also received considerable amount of research attention. For instance, the ductile and brittle characteristics of spall fracture in iron and some steels have been explored by numerous researchers [19, 214, 263, 264, 345, 356–365]. Interestingly, the spall strength and spall morphology changes significantly and these changes have been linked to the reversible polymorphic or allotropic phase transformation which takes place at approximately 13 GPa. When iron and some steels are shock compressed above the phase transformation stress (from α-phase to ϵ-phase) and then released to stresses below 9.8 GPa (back to the α-phase), the spall morphology has been observed to be ductile (smooth surface). But when shock compressed below the phase transformation stress (only α-phase), the spall morphology has been observed to be brittle (rough surface) [214, 363].

To decipher this observed ductile to brittle transition in spall morphology in iron and some steels, Erkman [214], Banks [358], and Barker and Hollenbach [366] proposed that the formation of a rarefaction shock and the sudden rise in the tensile stress pulse occurring in a very narrow region of the material is responsible for the formation of smooth spall surfaces. Meyers and Aimone [19], Zurek and Meyers [363], and Zurek [365] concluded that this response can lead to a very localized fracture region. On the contrary, when the material was shock compressed and spalled below the phase transformation stress of 13 GPa, the tensile stress pulse increases at a slower rate (no rarefaction shock) and, therefore, the deformation occurs in a wider region creating a rough spall surface. Zurek et al. [363, 365] have studied the influence of shock prestrain and peak pressure on spall behavior and spall failure characteristics of 4340 pearlitic steel. They found that the α-to-ϵ phase transformation strongly influences the transition in fracture mode from brittle (below 13 GPa shock stress) to ductile (above 13 GPa shock stress). The resulting spall morphologies of the 4340 pearlitic steel above and below the phase transformation stress are shown in Figure 4.33. Zurek et al. [363, 365] concluded that the spall strength of the 4340 pearlitic steel increases due to the phase transformation but pre-stress decreases the spall strength when shock compressed above the phase transformation stress with no change of mode in the spall morphology. It must be noted that some other parameters such as grain refinement [367], strain-rate [367], and local temperature rise [365, 368] can also influence the ductile-to-brittle fracture transition point.

The high strain rate deformation twinning behavior of high-purity BCC tantalum subjected to high explosively driven shocks was studied by Livescu et al. [369]. The recovered samples which were shock compressed to relatively high and low stresses exhibited significant amount of $\{112\}\langle 111\rangle$ deformation twins. From their analyses, they were able to show that for the lower shock stress, the recovered sample exhibited deformation twins that are spatially clustered at the mesoscale and, thereby, reveal the role of twin termination at grain boundaries to produce the required twin initiation stresses in neighbor grains. Furthermore, the results they acquired from electron backscatter diffraction analysis suggests that twin propagation across grain boundaries does not require minimal misorientations between the active variants of the deforma-

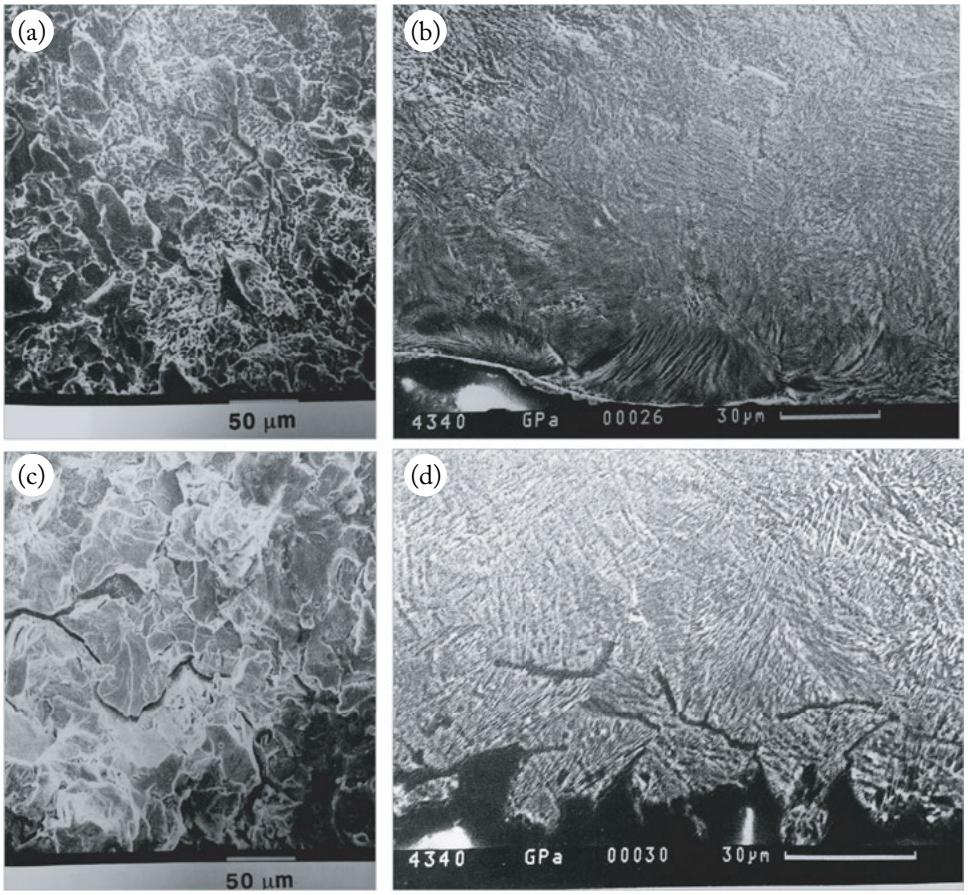

Figure 4.33: Fractographs of 4340 pearlitic steel showing (a) ductile fracture surface above 13 GPa, (b) cross section of smooth spall surface above 13 GPa, (c) brittle fracture surface below 13 GPa, and (d) cross section of rough spall surface below 13 GPa. Note that the spall plane is at the bottom of figures (b) and (d) [363, 365].

tion twins in adjacent parent grains. Livescu et al. [369] established a minimum threshold grain size of approximately 25 μm below which deformation twinning was suppressed. They observed microvoids at twin intersections which implies that deformation twinning increases the density of potential void nucleation sites during the shock compression phase (see Figure 4.34). Their overall observations show that deformation twinning plays a significant role in the deformation and damage evolution processes in shock-compressed tantalum.

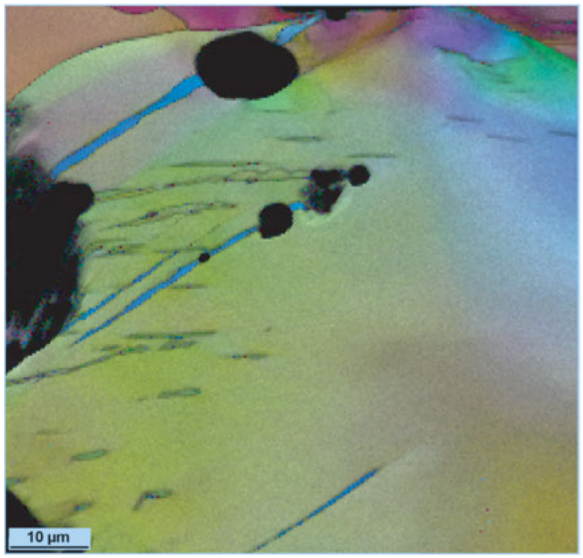

Figure 4.34: EBSD map showing intragranular voids at twin intersections in a tantalum sample shock compressed to a relatively low stress [369].

4.3.3 SPALLATION IN METALS WITH HCP LATTICE STRUCTURE

Metallic alloys of Magnesium (Mg), Zirconium (Zr), Hafnium (Hf), Yttrium (Y), and Titanium (Ti) with low-symmetry Hexagonal Close Packed (HCP) crystal lattice structure have seen an upsurge in usage for structural and other applications. This is primarily because of their attractive properties such as high specific strength relative to other traditional structural materials, excellent corrosion resistance, and low absorption cross section for thermal neutrons. This increase in usage has led to an increase in research activities relating to the mechanical behavior of these HCP metals and metallic alloys across different length-scales. Although the bulk of research relating to materials with HCP crystal lattice structure has been primarily limited to three metals and their metallic alloys (magnesium, titanium, and zirconium) because of their importance in the automotive [370–373], aerospace [374–379], defense [380–383], and nuclear [384, 385] industries; research relating to the high strain rate behavior, in particular the shock response of HCP materials is relatively low when compared to its FCC and BCC counterparts. The need to develop a better understanding of the structure-property relationships pertaining to shock compressed HCP metals and their metallic alloys is of great interest to the shock compression science community. A reasonable amount of research papers concerning the spallation and morphology of spall failure of HCP metals and their metallic alloys have been published in the open literature [61, 63, 140, 169, 170, 386–390] and this section will elucidate some of these results.

The shock and spall responses of armor-grade wrought magnesium alloy Elektron 675 were examined by Hazell et al. [386] with respect to the material's processing type and loading

direction. Two armor-grade wrought magnesium alloys Elektron 675 were examined, the cast then extruded "F condition"and the cast, extruded, then artificially aged "T5 condition."The HEL for the T5 condition was determined to be 0.38 ± 0.02 GPa which is higher than that obtained for the F condition. Precursor decay was observed in the F condition material but the T5 condition material did not exhibit precursor decay. Hazell et al. [386] attributed this significant difference in the elastic-plastic response to the aging process, which hinders dislocation nucleation and mobility and, consequently, precursor decay. They observed an increase in the HEL when the samples were shock compressed along the extrusion direction and attributed this increase to the presence of the striations of small grains (see Figure 4.35). Hazell et al. [386] observed that deformation twinning was hindered by the level of precipitation hardening in the samples. For instance, a relatively low amount of deformation twins were observed in the T5 condition samples, while more extensive deformation twins were observed in the F condition samples.

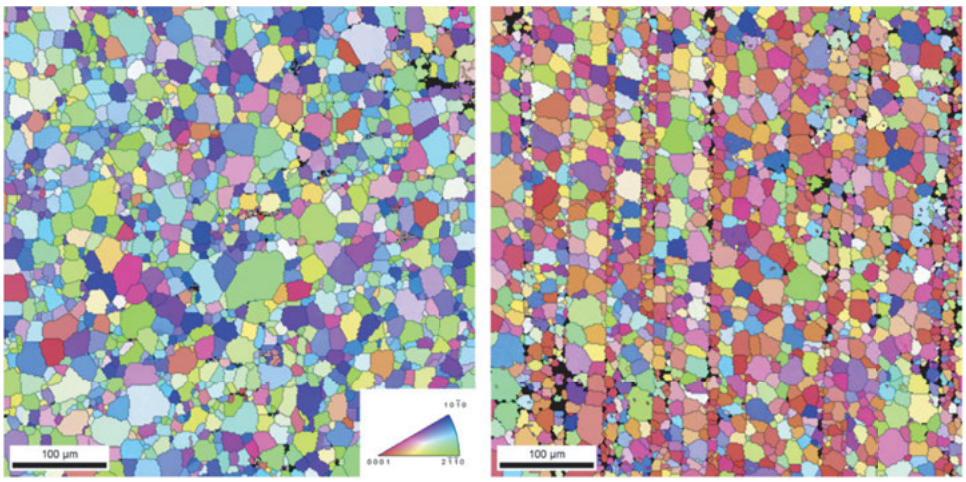

(a) (b)

Figure 4.35: Inverse pole figure maps of armor-grade wrought magnesium alloys Elektron 675 (a) normal to the extrusion direction and (b) perpendicular to the extrusion direction [386].

This research clearly reveals that the spall strength of this armor-grade wrought magnesium alloy Elektron 675 is a function of processing direction. It was determined by Hazell et al. [386] that long striations of smaller grains as revealed in Figure 4.35b may be responsible for the observed increase in spall strength when the alloy was shock compressed along the extrusion direction for both conditions. On the contrary, these long striations of smaller grains are likely responsible for the drop in spall strength when the material was shock compressed perpendicular to the extrusion direction for both conditions. In other words, these long striations of smaller grains are the weak link in the microstructure and are potential failure sites. The micrographs

in Figure 4.36a and Figure 4.37 (which is an enlarged region around the spall plane) revealed that cracks nucleate and grow perpendicular to the spall plane when the material was shock compressed along the extrusion direction and they tend to grow along the boundaries of small grains. However, Figure 4.36b reveals that when samples were shock compressed perpendicular to the extrusion direction, spall failure was activated by the presence of the small bands of grains.

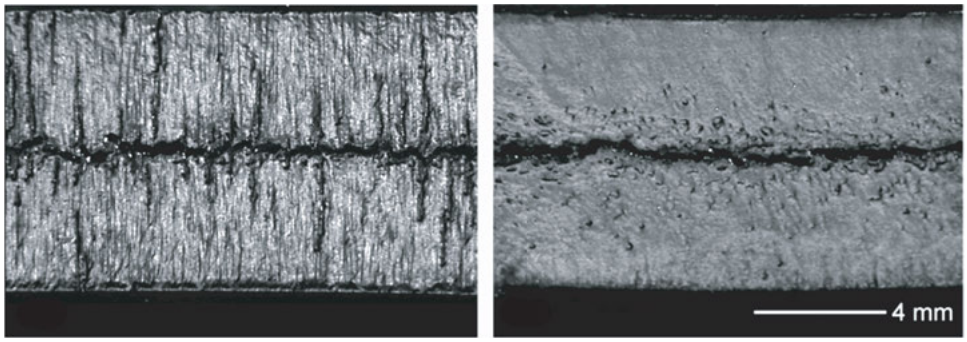

(a) (b)

Figure 4.36: Spall cracks for two T5 Elektron 675 samples: (a) shock compressed along the extrusion direction and (b) shock compressed perpendicular to the extrusion direction at approximately 1.3 GPa shock stress [386].

The effects of microstructure on the spall strength have also been studied by Farbaniec et al. [140]. They conducted both time-resolved normal plate impact experiments and spall recovery experiments to study the spall response and failure characteristics of AZ31B-4E magnesium alloy processed via Equal-Channel Angular Extrusion (ECAE). The Hugoniot Elastic Limit (HEL) of this material was determined to be approximately 0.181 ± 0.003 GPa. Farbaniec et al. [140] found that the spall strength of the shock compressed samples decreases by 5% for shock stresses ranging from 1.7–4.6 GPa. However, they concluded that this reduction in spall strength may fall within the experimental error. They performed post-test fractographic examinations on the shock-recovered samples and observed that spall failure originated at micrometer-size second-phase intermetallic inclusions which propagated through the material with very limited void growth. As shown in Figure 4.38, the second phase intermetallic inclusions were identified as Al-Mn using Energy Dispersive Spectroscopy (EDS) analysis.

Figure 4.39 shows the microstructure of the as-received and recovered materials; it reveals a uniform distribution of closely spaced submicron-sized Al-Mn particles throughout the magnesium matrix in addition to the large Al-Mn clusters. Farbaniec et al. [140] concluded that the strengthening of AZ31B-4E magnesium alloy via the ECAE process resulted in detrimental effects on its microstructure and consequently, the spall behavior, because of the process-induced cracking of second phase Al-Mn intermetallic inclusions and their weak interface strengths.

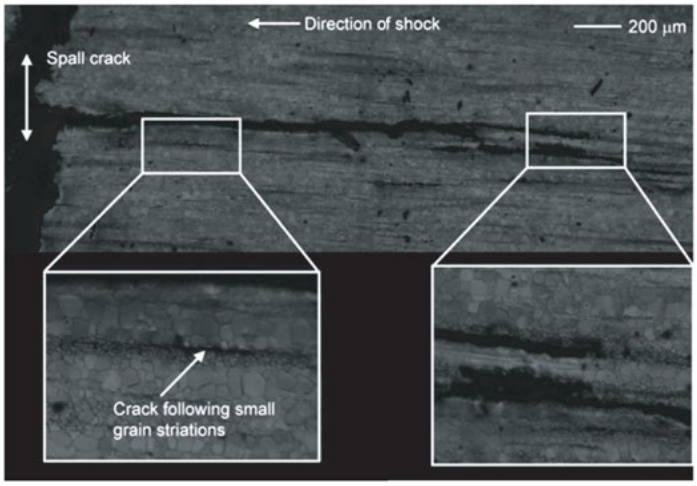

Figure 4.37: Shock recovered sample of the armor-grade wrought magnesium alloys Elektron 675 revealing the details of the cracks emanating from the spall plane parallel to the direction of impact at approximately 1.3 GPa shock stress (T5 condition shocked along extrusion direction) [386].

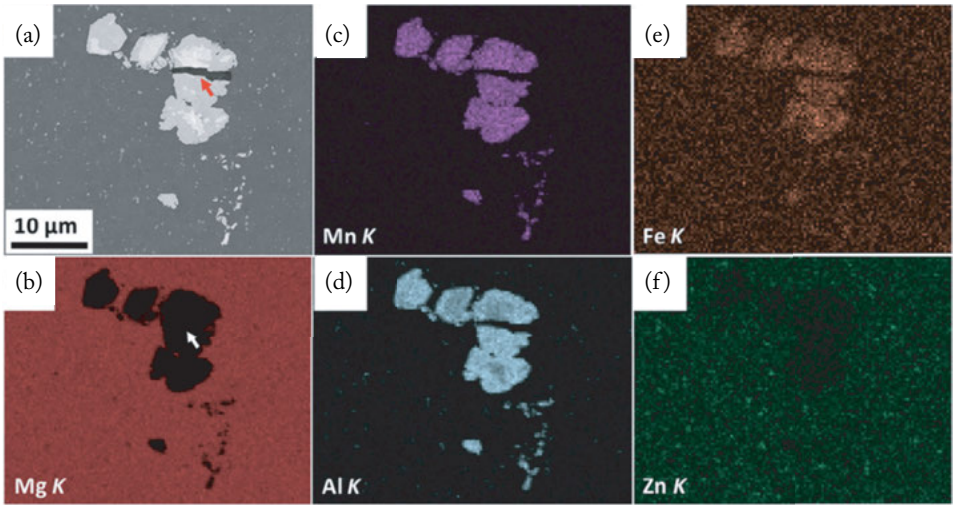

Figure 4.38: Combined SEM/EDS map analysis of the AZ31B-4E Mg alloy, where: (a) SEM micrograph of the investigated area of the as-received material, (b) EDS elemental map of Mg, (c) EDS elemental map of Mn, (d) EDS elemental map of Al, (e) EDS elemental map of Fe, and (f) EDS elemental map of Zn [140].

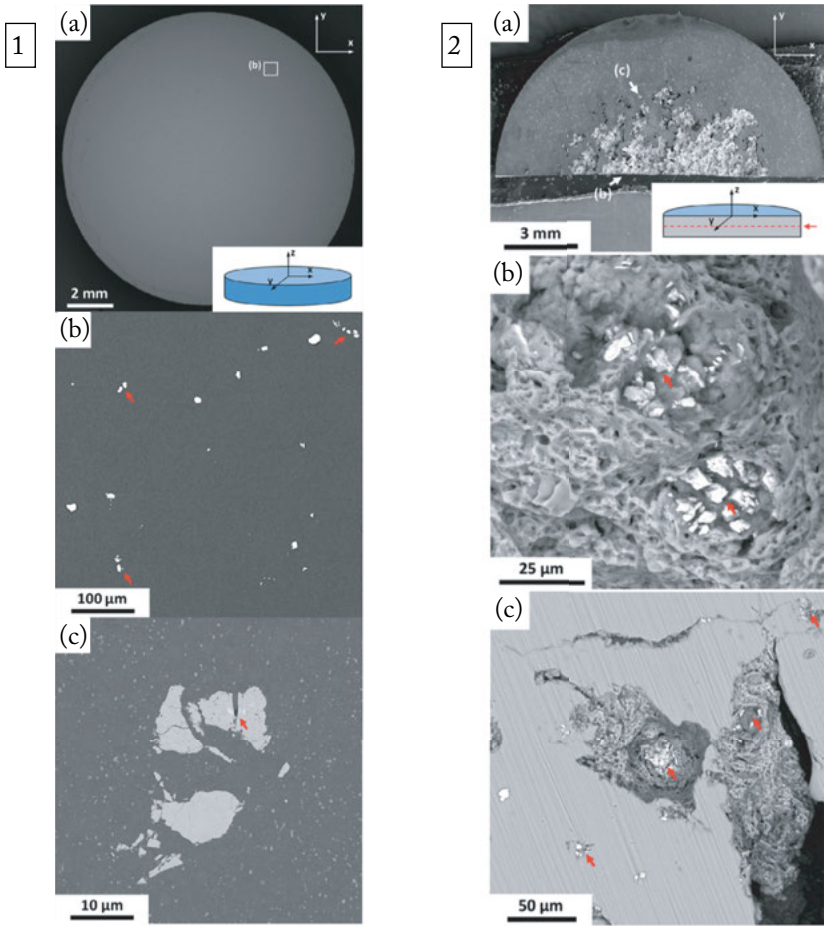

Figure 4.39: SEM micrographs of the as-received AZ31B-4E Mg alloy sample in backscattered electron contrast (BSE) mode, where: 1(a) investigated sample, 1(b) zoomed-in view secondary phases of Al-Mn, and 1(c) high-magnification of the sample showing a cluster of broken secondary phases of large Al-Mn intermetallic inclusions surrounded by a smaller distribution of the same phase. SEM micrographs (BSE mode) of the mid-plane (spall plane) of the recovered AZ31B-4E Mg alloy sample shock compressed to approximately 1.7 GPa: 2(a) investigated specimen (the red arrow indicates the position of the plane of the specimen under investigation), 2(b) zoomed-in fracture surface at the center of the spall plane with intermetallic inclusions identified by arrows, and (c) zoomed-in fracture surface at the edge of the spall plane with intermetallic inclusions [140].

They suggested that it is likely that these clusters of inclusions present in the fracture surface as shown in Figure 4.392b in this magnesium alloy were formed during the ECAE process and not during shock compression. Nevertheless, their locations on the fracture surface, and probably most important their prevalence, suggest that these inclusions act as initiation sites for spall failure. Furthermore, they hypothesized that the early stages of spall failure was dominated by nanovoid formation as shown in Figure 4.40 near the interfaces between the intermetallic inclusions and the matrix magnesium. However, the cause for nucleation, growth, and coalescence of the nanovoids cannot be attributed to vacancy clusters or neither ruled out and is therefore unresolved.

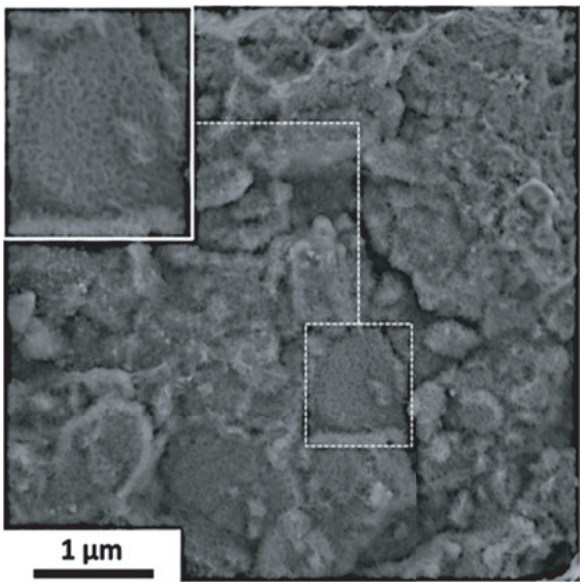

Figure 4.40: SEM micrograph of the fracture surface in the center of the spall plane revealing nanovoids at the interface between the intermetallic inclusions and the magnesium matrix. The solid box is an enlarged area of the small box [140].

Farbaniec et al. [169] also studied the spall response and failure characteristics of AMX602 magnesium alloy powder obtained from Spinning Water Atomization Process (SWAP), which was cold-pressed and hot-extruded between 573 K and 673 K [391, 392]. They employed both in-situ (real time) and ex-situ (end-state) plate impact experiments for this study and their in-situ results for this AMX602 magnesium alloy show that the spall strength increased by 8% for shock stresses ranging from 1.61–4.53 GPa. This result is contrary to that obtained for the AZ31B-4E magnesium alloy. They also determine the Hugoniot Elastic Limit to be approximately 0.187 ± 0.011 GPa, comparable to that obtained for the AZ31B-4E magnesium alloy. They analyzed the morphology of the spall surface of recovered samples using a scanning electron microscope. From

their analysis, they observed that the fracture surface of the spalled sample shock compressed to approximately 1.7 GPa was striated and the striations were unidirectionally aligned, as shown in Figure 4.41, most likely due to the presence of the lamellae-like oxide (MgO) layers. This feature is somewhat consistent with previous observations on spalled surfaces of metals consolidated by powder metallurgy.

Figure 4.42a represents a magnified view of the striated spall surface shown in Figure 4.41 and the striations are clearly visible in the horizontal direction. The pore in Figure 4.42a (enclosed by the box labeled *b*) when further magnified, reveals that the spall surface exhibits brittle-like fracture with few traces of larger cracks (indicated by the arrows), as shown in Figure 4.42b. Furthermore, the region labeled *c* in Figure 4.42b reveals a brittle-like phase on the fracture surface (marked as *ii* in Figure 4.42c) delineated from the ductile region by a major crack, which is most likely an intermetallic inclusion. However, this brittle-like phase is surrounded by a well developed ductile fracture zone with nanometer and micrometer size voids. Few precipitates believed to be intermetallic Al_2Ca compounds are observed within the voids (indicated by the arrows). Farbaniec et al. [169] made another interesting observation of a rather unusual feature inside the pore (see Figure 4.42d) and concluded that the cold compaction process of elemental powder blends followed by hot-extrusion does not always result in a homogeneous and uniform microstructure. Such types of heterogeneity are generally undesirable and can lead to non-uniform properties in the material. They speculated that local variations in spall strength values were affected by these microstructural variations in the material.

The recovered sample shock compressed to approximately 0.9 GPa, revealed isolated cracks within the spall zone spanning several hundred microns, as shown in Figure 4.43b. They characterized the spall damage as having multiple isolated horizontal cracks (indicated by the arrows in Figure 4.43b), which are linked by vertical cracks within the spall zone. Such discontinuous damage zones are likely to grow and become a well defined spall plane at higher shock stresses. Figure 4.43c represents a magnified view of the fracture surface of an isolated region depicted by *c* within the spall zone in Figure 4.43b. It is quite evident from Figure 4.43c that the spall surface is populated with nano (labeled as *nv*) and submicron size voids (labeled as *mv*). Such mixed mode failure in metals and metallic alloys can occur when both homogeneous and heterogeneous nucleation of voids are activated concurrently by the application of high enough tensile stresses. In general, low-angle grain boundaries, fine impurities and precipitates, dislocations tangles and networks, and vacancy clusters are known to be potential homogeneous nucleation sites [19, 262] for nanovoids. On the other hand, high-angle grain boundaries, inclusions, and second-phase particles are known to be potential heterogeneous nucleation sites for microvoids [19, 262]. Farbaniec et al. [169] also observed that the spall surface was populated with numerous Al_2Ca based intermetallic compounds (labeled as *ii* in Figure 4.43c) and closely spaced submicron-sized precipitates. These microstructural defects were most likely responsible for the initiation of spall failure of the sample. Based on these fractographic examinations,

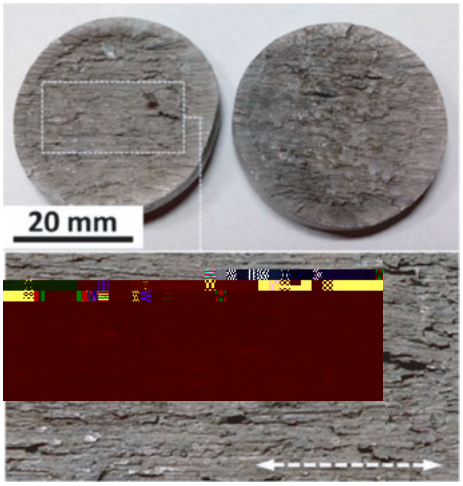

Figure 4.41: Optical micrograph of the recovered sample shock compressed to approximately 1.7 GPa [169].

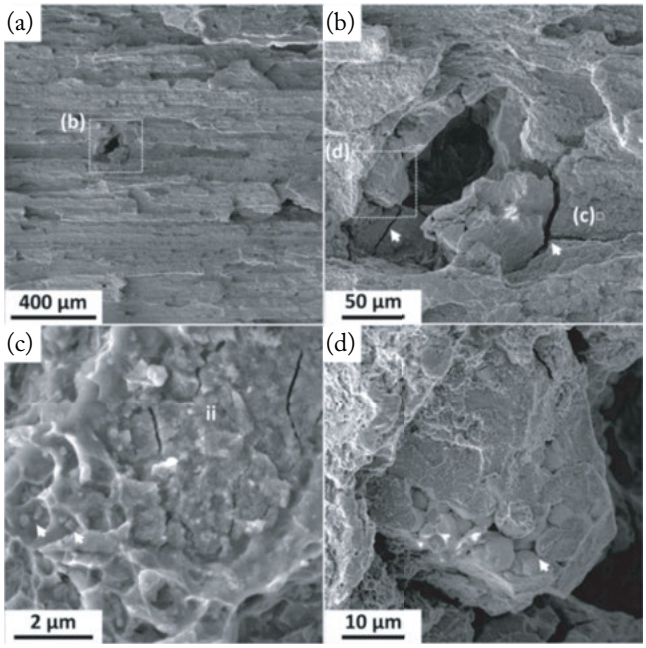

Figure 4.42: SEM micrographs of the fracture surface of the recovered AMX602 magnesium shock compressed to 1.7 GPa: (a) magnified view of the striated spall surface, (b) closeup view of the void shown in subfigure (a), (c) intermetallic Al_2Ca compound surrounded by nanometer and micrometer size voids, and (d) internal voids or microporosity in the microstructure of the as-processed Mg alloy [169].

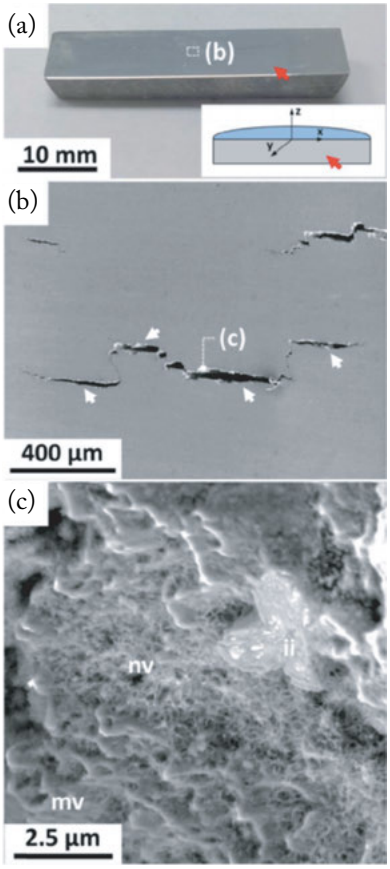

Figure 4.43: (a) Optical micrographs of the cross-sections of the recovered sample shock compressed to approximately 0.9 GPa, (b) SEM investigation of the damage zone showing isolated cracks within the spall plane, and (c) a view within the crack designated c showing micron-size or largervoid-like features (mv), nanovoids (nv), and intermetallic inclusions (ii) [169].

Farbaniec et al. [169] suggested that the dominant mechanisms for spallation is driven by the nucleation, growth, and coalescence of nanovoids and microvoids.

Jones et al. [390] conducted simultaneous time-resolved in-situ and end-state spall recovery experiments to study the directional dependence of spall strength and spall failure characteristics of an additively manufactured (AM) Ti-6Al-4V alloy. They used two pieces of selective laser melted (SLM) Ti-6Al-4V alloy produced from extra-low-interstitial (ELI) Ti-6Al-4V alloy powder such that the dynamic tensile stress developed from the collision of release waves in the material will align either along or normal to the interfaces between build layers. Wrought bar-stock Ti-6Al-4V alloy was used as a reference material, which is a representation of a tradi-

tionally manufactured material. Figure 4.44 is an inverse pole-figure map of the microstructure of the additively manufactured Ti-6Al-4V alloy. The figure reveals a microstructure constituting of fine needle-like or acicular grains of α' martensite contained within much larger columnar α grains, of which the larger columnar α grains approximately lie parallel to the build layer interfaces.

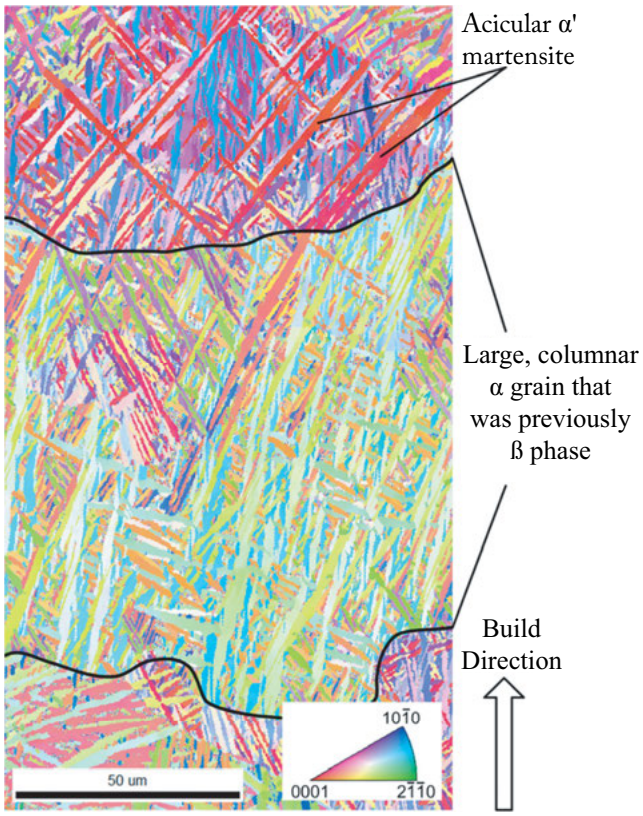

Figure 4.44: Inverse pole-figure map of the additively manufactured Ti-6Al-4V alloy; image taken along the through thickness direction [390].

From this research, Jones et al. [390] observed that when the additively manufactured Ti-6Al-4V alloy was shock compressed normal to the interfaces, the corrected spall strength determined from time-resolved in-situ shock experiments is significantly reduced. This reduction represents a 60% drop in spall strength relative to that of the wrought bar-stock Ti-6Al-4V alloy which was determined to be 5.28 $\pm$ 0.11 GPa. However, when the material was shock compressed parallel to the AM build layer interfaces, the spall strength was determined to be 95% of the wrought bar-stock Ti-6Al-4V alloy. Jones et al. [390] suggested that when the material is shock compressed and then subjected to tensile stresses normal to the AM layer interfaces,

voids and cracks are nucleated with relative ease due to the weak AM build layer interfaces, leading to delamination along these boundaries. The optical micrographs in Figure 4.45 represent spall damage evolution in both the wrought bar-stock and additively manufactured Ti-6Al-4V alloys shock compressed to 3.7 GPa (310 m/s) and 4.9 GPa (415 m/s), respectively. The general consensus derived from these experiments is that damage evolution is dependent on sample orientation. The wrought bar-stock Ti-6Al-4V alloy suffered the least damage at both stress levels followed by shocking parallel to the AM layer interfaces, and the most damage was suffered by shocking normal to the AM layer interfaces. These results corroborate the spall strength results determined from time-resolved in-situ shock experiments. It is noteworthy to point out that Jones et al. [390] obtained similar results from their quasi-static experiments using the same sample orientations but the interface weakness resulting from the SLM manufacturing process were much more pronounced in the shock experiments. Results derived from this research are strong justifications for the importance of rate-dependent studies on damage evolution in AM materials.

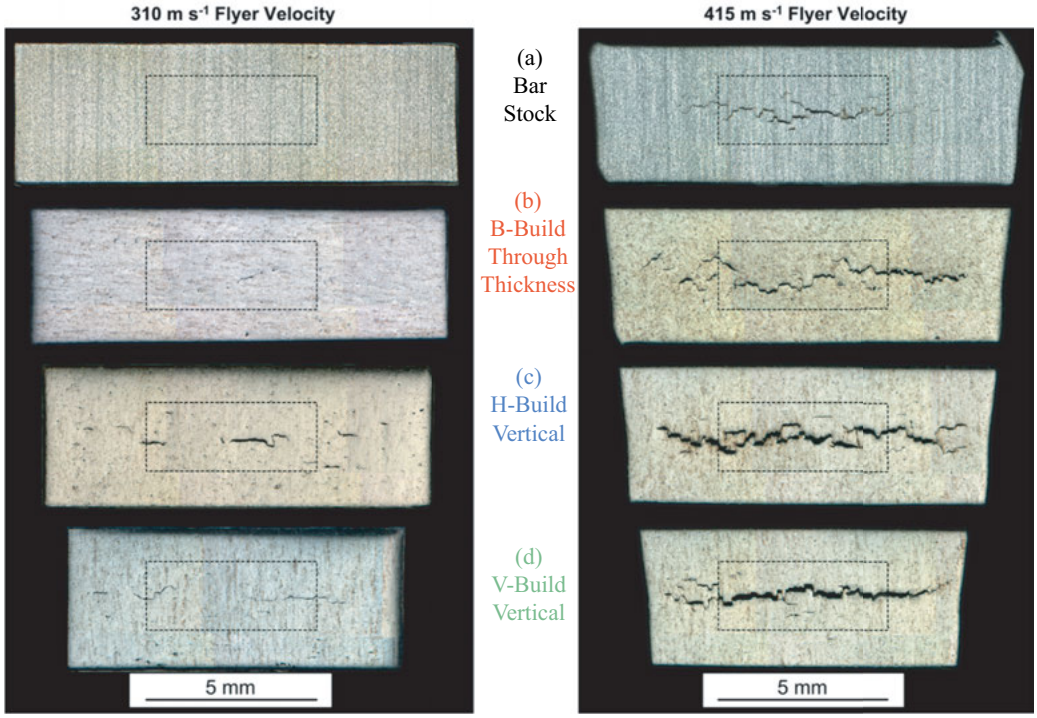

Figure 4.45: Optical micrographs of the shock recovered additively manufactured Ti-6Al-4V alloy samples. The 5 mm × 2 mm dashed boxes represent the region used for damage analysis [390].

Cerreta et al. [60, 393] studied the dynamic response of zirconium (Zr) and they have determined that the $\alpha - \omega$ phase transformation and substructure evolution can strongly influence the material's residual mechanical properties. For instance, they determined that the residual hardness of shock compressed Zr increases substantially at stresses above the threshold required for the $\alpha - \omega$ phase transformation. It is well known that ductile materials possessing high strength, tend to resist void growth under tensile stresses [130, 394–399], perhaps for this reason, Hazell et al. [387] studied the influence of shock-induced $\alpha - \omega$ phase transformation on the evolution of damage during spallation. From the micrographs shown in Figure 4.46, the classical nucleation, growth, and coalescence of ductile voids is clearly evident. The amount of residual damage shown in Figure 4.46 appears to increase with increase in shock stress up to approximately 5.3 GPa. Also, voids coalescing to form large damage zones is quite evident in Figure 4.46e. However, at approximately 7.6 GPa, spall damage becomes more disperse about the spall plane showing less evidence of void coalescence (see Figure 4.46f). Interestingly, the change in damage mode occurs between shock stresses of 5.3 GPa and 7.6 GPa, which is in proximity to the $\alpha - \omega$ phase transformation stress reported in the open literature [60]. Hazell et al. [387] postulated that the hard ω phase may be responsible for the resistance to void growth and consequently arrest damage evolution during the spall process.

4.4 MICROSTRUCTURE OF EXPLOSIVELY COMPACTED POWDERS AND POWDER MIXTURES

For several decades, a wide variety of materials, parts, and commercial products have been developed or fabricated using powder metallurgy. Numerous materials such as silicon carbide [247], boron nitride [400], nickel-base superalloys [43], titanium alloys [401], and aluminum-lithium alloys [402] have been compacted from powders and powder mixtures. Although powders and powder mixtures can be compacted or consolidated by conventional methods such as press-sintering, hot isostatic pressing (HIP), etc., explosives offer the best densification for metal and ceramic powders and powder mixtures. Powder compaction and consolidation using explosives involves very evanescent (shock rise time of ~50 ns [403]) and intense deposition of shock energy to facilitate interparticle bonding in powders and powder mixtures. Under ideal shock conditions, the densities achieved can approach 100% of the theoretical value [244]. The densities of shock consolidated ceramic powders strongly depends on the particle size of the as-received powder or powder mixture. The aim of this section is to present a concise description of the mechanisms and microstructure evolution active during the shock consolidation of powders and powder mixtures. Nevertheless, for an in-depth knowledge on the subject, the reader is strongly encouraged to review the references of [244, 251, 404–417] on shock consolidation of powders and powder mixtures.

For instance, the shock consolidation of mechanically alloyed titanium-aluminum (Ti-Al) intermetallics was investigated by Szewczaka et al. [416]. Their starting powder composed of 99.8% purity aluminum and 99.5% purity titanium with particle size ranging from 40–50 μm

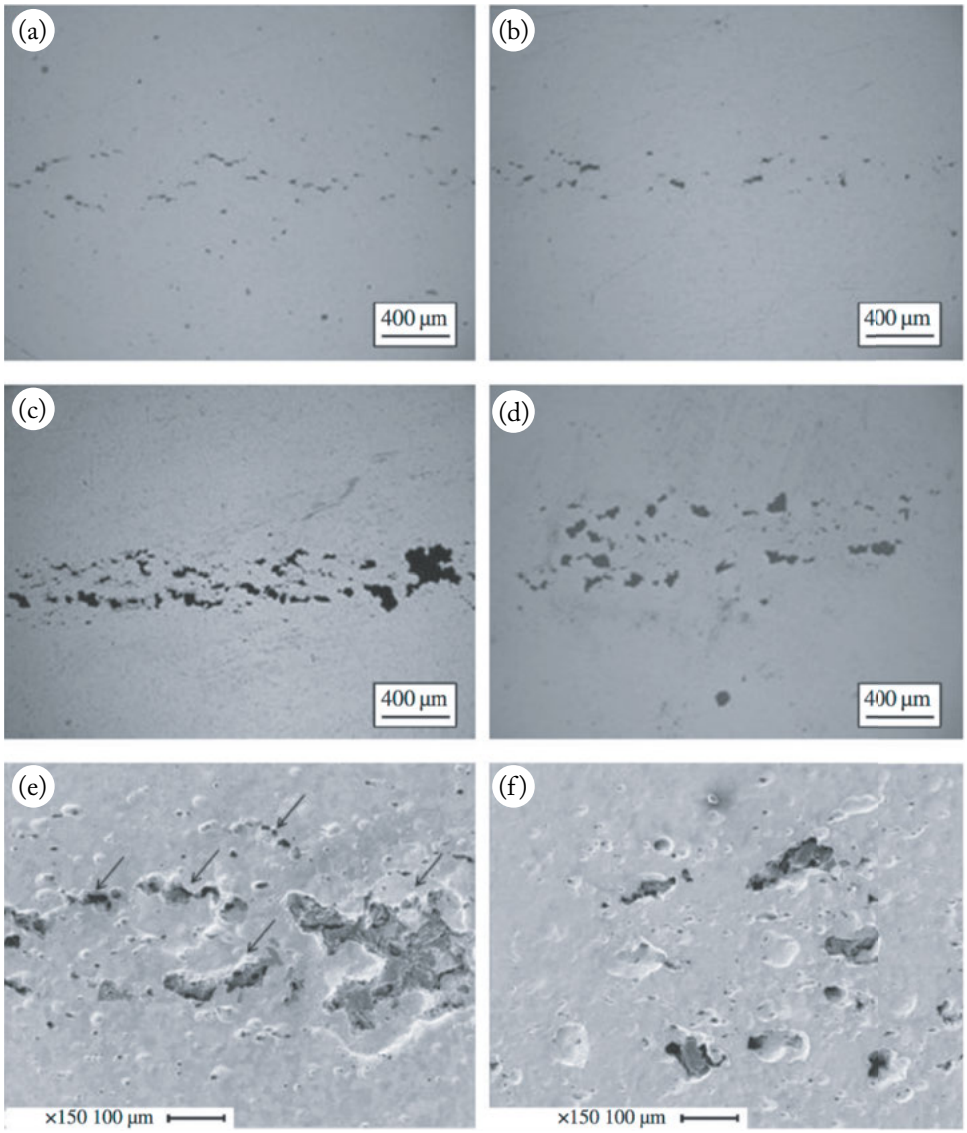

Figure 4.46: Optical micrographs of α-zirconium showing spall damage for shock stress: (a) 2.6; (b) 3.9; (c) 5.3; (d) 7.6 GPa. Scanning electron micrographs of the spall damage at (e) 5.3 and (f) 7.6 GPa. The shock direction in all micrographs is from bottom to top [387].

and 150–200 μm, respectively. Two elemental blends were attained using compositions of Ti-25at.%-Al and Ti-50at.%-Al, which were subsequently cold compacted under 500 MPa pressure to form supersaturated solid solutions. The samples were then shock consolidated with an explosive possessing a detonation velocity of 3000 m/s, generating a 4.4 GPa pressure and 400°C temperature. After shock consolidation, the samples were annealed for 1.5 h at 700°C. From the X-ray powder diffraction (XRD) results shown in Figure 4.47a, Szewczaka et al. [416] observed that the $Ti_{50}Al_{50}$ sample after 100 h of milling consists of three phases, HCP Ti(Al), FCC Al(Ti) supersaturated solutions, and an amorphous phase.

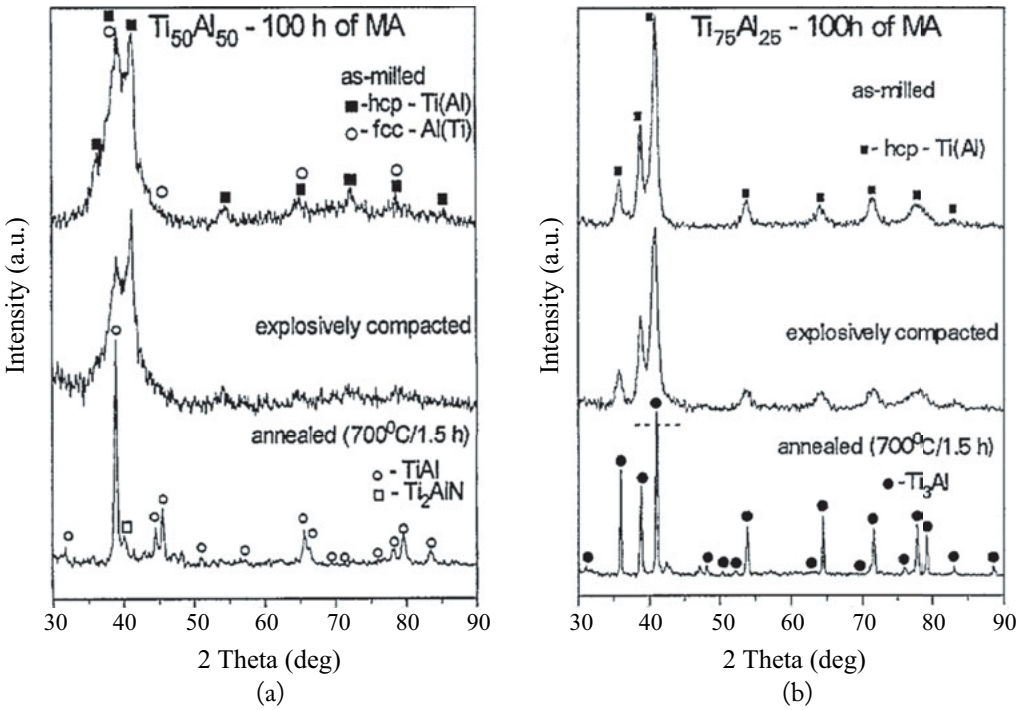

Figure 4.47: XRD patterns for (a) $Ti_{50}Al_{50}$ and (b) $Ti_{75}Al_{25}$ samples [416].

However, they only observed diffraction peaks from HCP supersaturated Ti(Al) for the $Ti_{75}Al_{25}$ samples after 100 h of milling as shown in Figure 4.47b. After shock consolidation, the XRD results in Figure 4.47a reveal a small change in the intensity of the FCC and HCP diffraction peaks for the $Ti_{50}Al_{50}$ sample, indicative of a phase transition of some part of the alloy. But the same was not true for the $Ti_{75}Al_{25}$ samples, no change was observed in the phase composition (see Figure 4.47b). It is evident from the XRD results in Figures 4.47a and 4.47b that annealing the shock consolidated materials can lead to phase transitions. The annealed shock consolidated $Ti_{50}Al_{50}$ sample reveals the formation of a TiAl-L_{10} compound with Ti_2AlN

impurities, whereas the annealed shock consolidated $Ti_{75}Al_{25}$ samples reveals a transformation of hexagonal disordered phase into hexagonal ordered phase which was identified as Ti_3Al.

Szewczaka et al. [416] concluded from this research that: (1) mechanical alloying of elemental powder mixtures of titanium and aluminum form supersaturated solid solutions and an amorphous phase in the $Ti_{50}Al_{50}$ sample; (2) grain sizes of approximately 400 nm were achieved by shock consolidating mechanically alloyed samples with no transitions of metastable phases into stable phases; (3) no significant change of amount ratio of HCP Ti(Al) and FCC Al(Ti) phases was observed in the case of the $Ti_{50}Al_{50}$ sample; (4) annealing the shock consolidated samples leads to the formation of stable phases, TiAl compound in the case of $Ti_{50}Al_{50}$ composition and Ti_3Al compound in the case of $Ti_{75}Al_{25}$; and (5) shock consolidation causes small change in the structure of lattice defects produced by mechanical alloying and a considerable change in this structure was observed after annealing.

The sintering of boron carbide and different modifications of boron were investigated by Kalandadze et al. [418]. They used pyrolytic and electrolytic amorphous boron powder with purity of 99.9-wt% and 96.0-wt%, respectively, to produce α and β rhombohedral boron from amorphous boron by crystallization at temperatures of 1200°C and 1800°C, respectively. Kalandadze et al. [418] produced boron carbide from the elements (boron and carbon) by direct synthesis at a temperature of 2000°C and the boron carbide powder was subsequently hot pressed at temperatures ranging from 1900–2100°C with pressures ranging from 20–40 MPa. The micrographs in Figure 4.48 illustrate the homogeneous and inhomogeneous grain structure emanating from hot-pressed monodisperse and polydisperse boron carbide powders. Higher densities were achieved from the monodisperse powders at lower temperatures. Note that, higher temperatures can increase the number of twins and grain size inhomogeneity due to grain growth and this is evident for the polydisperse boron carbide, as shown in Figure 4.48b. The powders were explosively shock compacted to approximately 10 GPa pressure to achieve 30% of the theoretical density. Figure 4.49 shows the residual microstructures of the shock compacted boron carbide and α-rhombohedral boron after thermal treatment and it is quite clear from the micrographs that the thermal treatment eradicates the remaining micropores after explosive compaction and facilitates grain growth.

From this study, Kalandadze et al. [418] concluded that the powder size distribution of the boron carbide defines the residual microstructure of a sintered pellet. Also, they found that the usage of α-rhombohedral boron to produce the boron carbide pellets in reactive sintering can lower the maximum sintering temperature to 1800°C due to its isostructural character. Comparing the sintering properties of α-rhombohedral, β-rhombohedral, and amorphous boron, they found that their sintering into the β-rhombohedral phase at the final stage can produce higher densities. They attributed this to the phase transformation occurrence from amorphous boron to β-rhombohedral boron through α-rhombohedral boron modification. Kalandadze et al. [418] concluded that thermal treatment after explosive compaction and subsequent sintering of boron and boron carbide eradicates micropores and facilitates grain growth.

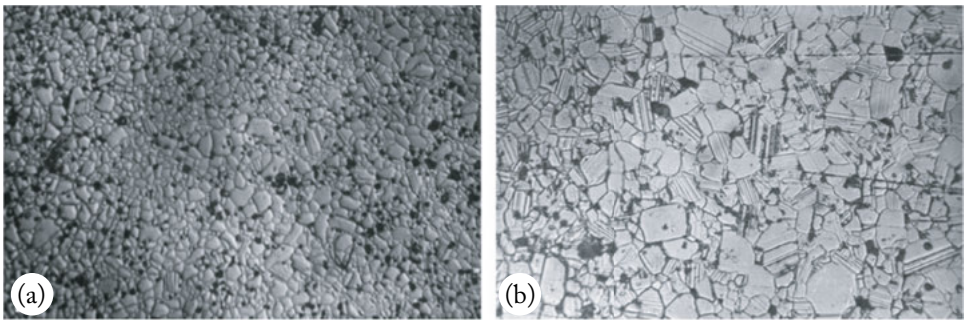

Figure 4.48: Micrographs revealing the microstructure of hot-pressed boron carbide: (a) from monodisperse powder (x300) and (b) from polydisperse powder (x300) [418].

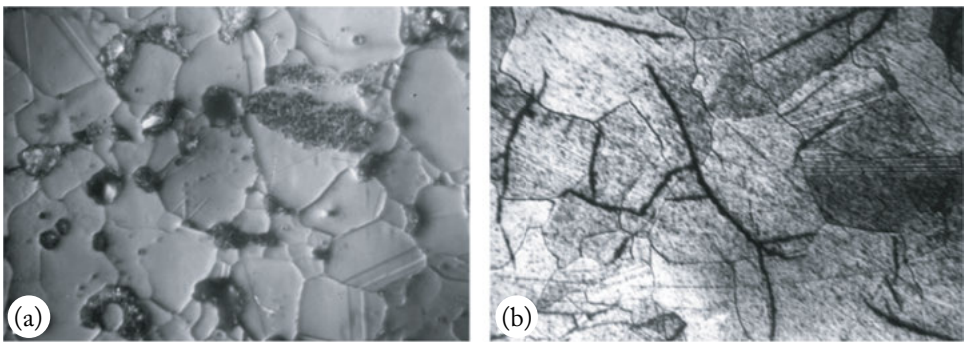

Figure 4.49: Micrographs revealing the microstructure of (a) boron carbide (x800) after the explosive compaction and thermal treatment at 1600°C and (b) α-rhombohedral boron (x800) after the explosive compaction and thermal treatment at 1200°C [418].

CHAPTER 5

The New Frontier in Shock Recovery Experiments

Although modern day shock recovery experiments have served the shock compression science community extremely well since the 1950s in developing a fundamental understanding on the structure-property relationships pertaining to condensed matter under extreme dynamic environments; its employment in shock compression science is still warranted today because of three new developing fronts. These fronts are novel materials and mechanical processing techniques, new/improved and emerging technologies in microscopy for materials science and engineering, and the recently developed time-resolved in-situ XRD shock experiments which were not available few decades ago. For instance, within the past few decades, there has been significant improvements on the development of tools required for probing the structure of materials over multiple length-scales ranging from the atomic level through the continuum level. The ability of modern microscopes to resolve and record digitized images in real time has increased tremendously in the past decade or two. Modern microscopes provide the ability to observe features that were not previously observed or studied before at exceptionally high resolution. Some of the new/improved and emerging technologies in microscopy for materials science and engineering include but are not limited to the following.

Microscopes

- Confocal Microscope [419–423]
- Electron Backscatter Diffractometry (EBSD) [424–430]
- Electron Channeling Contrast Imaging (ECCI) [431–435]
- Atomic Force Microscopy (AFM) [436–440]
- Atom Probe Tomography (APT) [441–445]
- Electron Energy-Loss Spectroscopy (EELS) [446–449]
- Energy Dispersive X-Ray (EDX) Spectroscopy [450, 451]
- Focused Ion Beam (FIB) [452–457]

- X-ray Computed Microtomography (μCT) [458–461]
- Precession Electron Diffraction (PED) [462–465]
- High-Resolution Transmission Electron Microscopy (HRTEM) [466–469]
- Scanning Transmission Electron Microscopy (STEM) [470–473]
- Phase Contrast Microscopy (PCM) [474–477]
- Phase-Contrast X-Ray Imaging (PCI) [477–481]

In addition to new/improved and emerging technologies in microscopy, which are required for probing the structure of materials across multiple length-scales, novel materials, and mechanical processing techniques are being developed. For example, coarse-grained metals and metallic alloys are currently been processed by Severe Plastic Deformation (SPD) processes to achieve very fine crystalline grain structure in the bulk. The size of these fine-grained crystalline structures can be less than 100 nm (nanocrystalline materials) or range from 100–500 nm (ultra-fine grained materials). SPD processes often involve very large strains plus complex stress states and as a consequence, enhanced mechanical properties such as superplasticity can be realized at lower temperatures. Some novel and emerging materials and SPD processes are listed below.

Novel materials

- Nanocrystalline [482–488]
- Ultra-Fine Grained [489–494]
- High-Entropy Alloys (HEAs) [495–500]
- Long-Period Stacking Ordered (LPSO) [501–507]
- Additively Manufactured [508–512]
- 3D Printed [513, 514]
- Cold Spray [515–518]
- Novel Composite and Alloys [519–521]
- Powder Metallurgy [391, 522–526]
- Metamaterials [527–534]

SPD Processes

- Equal Channel Angular Extrusion (ECAE) [535]

- High Pressure Torsion (HPT) [536]
- Accumulative Roll Bonding (ARB) [537]
- Repetitive Corrugation and Straightening (RCS) [538]
- Asymmetric Rolling (ASR) [539]
- Spinning Water Atomization Process (SWAP) + Hot Extrusion [540, 541]

The third front is the recently developed time-resolved in-situ (real-time) high-energy synchrotron X-ray diffraction (XRD) measurements via plate impact shock experiments. These experiments were developed to couple time-resolved velocity measurements with X-ray scattering (Debye-Scherrer rings or Laue spots) or imaging (phase contrast) to understand the fundamental mechanisms governing time-dependent behavior in shock compressed condensed matter. These experiments are currently being conducted with great success at three main synchrotron facilities around the world, which are listed below, and have been playing a significant role in understanding the fundamental basis of material behavior under extreme conditions [113, 153, 191, 192, 542–550]. These measurements are well suited for validating multiscale computer models designed to study shock compressed solids, but also, when these measurements are coupled with results derived from shock recovery experiments, they can help to bridge the existing knowledge gap between the ambient, shock, and release states. It should be noted that time-resolved in-situ (real-time) high-energy synchrotron X-ray diffraction (XRD) measurements are in their infancy and currently do not provide data on the morphology of the substructure, microstructure, and mesostructure of the material being interrogated. At present, data concerning the morphology of the aforementioned structures have to be derived from shock recovery experiments. Finally, this book on the subject of structure-property relationships under extreme dynamic environments closes by strongly encouraging researchers to revisit old unsolved problems and pursue new ones to develop the fundamental knowledge of the mechanisms governing the time-dependent behavior in shock-compressed condensed matter and bridge all existing knowledge gaps.

<u>High-Energy Synchrotron X-Ray Diffraction (XRD) Shock Facilities</u>

- Dynamic Compression Sector (DCS), Advanced Photon Source (APS), Argonne National Laboratory, USA
- Stanford Linear Accelerator Center (SLAC) National Accelerator Laboratory, Stanford Synchrotron Radiation Lightsource, USA
- European Synchrotron Radiation Facility (ESRF), France

References

[1] U.S. Navy. www.navy.mil/view-image.asp?id=102143 2, 3

[2] G. Doig, T. J. Barber, E. Leonardi, A. J. Neely, and H. Kleine, Aerodynamics of a supersonic projectile in proximity to a solid surface, *AIAA Journal*, vol. 48, no. 12, pp. 2916-2930, December (2010). DOI: 10.2514/1.J050505. 3

[3] G. S. Settles, *American Scientist*, 94(1), 22 (2006). DOI: 10.1511/2006.57.986 3

[4] Defence Research and Development Canada. https://www.canada.ca/en/defence-research-development/news/articles/drdc-experimental-proving-ground-supports-allied-readiness.html 2, 3

[5] C. S. Smith, *Transactions of the Metallurgical Society of AIME*, 212 (1958). 2, 3, 4, 7, 45, 48, 70

[6] G. Gray III, in *High-Pressure Shock Compression of Solids*, pp. 187–215, Springer, (1993). DOI: 10.1007/978-1-4612-0911-9_6 7, 57, 58, 79

[7] E. G. Zukas, *Metals Engineering Quarterly*, 6, 1 (1966). 7

[8] M. A. Meyers and L. E. Murr, *Shock Waves and High-Strain-Rate Phenomena in Metals*, pp. 121–151 (1981). DOI: 10.1007/978-1-4613-3219-0

[9] P. S. DeCarli and M. A. Meyers, in *Shock Waves and High-Strain-Rate Phenomena in Metals*, pp. 341–373, Springer (1981). DOI: 10.1007/978-1-4613-3219-0_22

[10] R. Orava and R. Wittman, *High Energy Rate Fabrication*, pp. 1.1–1.1, 27, University of Denver Research Institute, CO (1975). DOI: 10.1007/978-1-4615-8696-8_7

[11] W. Leslie, in *Metallurgical Effects at High Strain Rates*, pp. 571–586, Springer, (1973). DOI: 10.1007/978-1-4615-8696-8_34 7

[12] G. T. Gray III, Shock recovery experiments: An assessment. *Technical Report*, Los Alamos National Lab., NM (1989). 51

[13] L. Murr, in *Shock Waves and High-Strain-Rate Phenomena in Metals*, pp. 607–673, Springer (1981). DOI: 10.1007/978-1-4613-3219-0_37 7, 57, 58

[14] L. Murr, *Materials at High Strain Rates*, pp. 1–46, Elsevier, Essex, UK (1987). 57, 58

[15] D. Raybould and T. Blazynski, *Materials at High Strain Rates*, p. 71 (1987).

[16] K. Staudhammer, Shock wave effects and metallurgical parameters. *Technical Report*, Los Alamos National Lab., NM (1987). 7, 57

[17] D. Mikkoila and R. Wright, in *AIP Conference Proceedings*, vol. 78, pp. 98–118 (1982). 60

[18] M. Mogilevsky and L. Teplyakova, *Methodical Aspects of Investigation of Structural Changes Under Shock Loading*, (1986).

[19] M. A. Meyers and C. T. Aimone, *Progress in Materials Science*, 28(1), 1, (1983). 79, 89, 97

[20] G. Gray, *ASM International*, pp. 530–538, Materials Park, OH, (2000).

[21] G. T. Gray III, *Annual Review of Materials Research*, 42, 285 (2012).

[22] N. Bourne and G. Gray, in *Proc. of the Royal Society of London A: Mathematical, Physical and Engineering Sciences*, vol. 461, pp. 3297–3312 (2005). DOI: 10.1098/rspa.2005.1501 48

[23] S. Mahajan, *Physica Status Solidi (a)*, 2(2), 187 (1970). 7, 57, 75, 80

[24] D. G. Doran and R. K. Linde, *Solid State Physics*, 19, 229 (1967). 2, 7, 45, 48

[25] C. A. Parsons, *Philosophical Transactions of the Royal Society of London. Series A, Containing Papers of a Mathematical or Physical Character*, 220, 67, (1920). 3

[26] A. Michel-Levy and J. Wyart, *Comptes Rendus*, 208, 1030 (1939). 3

[27] P. S. DeCarli and J. C. Jamieson, *Science*, 133(3467), 1821 (1961). 4, 45, 53

[28] I. N. Riabinin, *Soviet Physics–Technical Physics*, 1:2575 (1956). 4

[29] Y. Horiguchi and Y. K. Nomura, *Bulletin of the Chemical Society of Japan*, 36(4), 486, (1963). 4

[30] G. Adadurov, I. Barkalov, A. Dremin, V. Goldanskii, P. Iampolskii, T. Ignatovich, A. Mikhailov, and V. Talroze, in *Akademiia Nauk SSSR, Doklady*, vol. 165, pp. 851–854 (1965). 4

[31] O. R. Bergmann and J. Barrington, *Journal of the American Ceramic Society*, 49(9), 502 (1966). 4, 45

[32] Y. Kimura, *Japanese Journal of Applied Physics*, 2(5), 312 (1963). 4

[33] I. Barkalov, V. Gol'danskii, V. Gustov, A. Dremin, A. Mikhailov, V. Tal'roze, and P. Yampol'skii, *Proc. of the Academy of Sciences of the USSR, Physics Chemistry Section*, 167, 217, (1966). 45

[34] A. Babare, A. Dremin, and A. Mikhailov, *Combustion, Explosion, and Shock Waves*, 5, 401 (1969).

[35] I. Ignatovich, I. Barkalov, I. Dulin, V. Zubarev, and P. Yampol'skii, *High Energy Chemistry*, 4, 394 (1970). 4

[36] T. Barbee, L. Seaman, R. Crewdson, and D. Curran, *Journal of Materials*, 7(3), 393 (1972).

[37] G. Adadurov, V. Gustov, and P. Yampol'skii, *Combustion, Explosion, and Shock Waves*, 7(2), 243 (1971). 45, 48

[38] A. L. Stevens and O. Jones, *Journal of Applied Mechanics*, 39(2), 359 (1972). 48

[39] L. Murr and K. Staudhammer, *Materials Science and Engineering*, 20, 35 (1975). 11, 58

[40] L. Seaman, D. R. Curran, and D. A. Shockey, *Journal of Applied Physics*, 47(11), 4814 (1976). DOI: 10.1063/1.322523 45

[41] R. Graham, P. M. Richards, and R. Shrouf, *Journal of Chemical Physics*, 72(5), 3421, (1980).

[42] B. Olinger and L. Newkirk, *Solid State Communications*, 37(8), 613 (1981). DOI: 10.1016/0038-1098(81)90534-2 45

[43] M. A. Meyers, B. B. Gupta, and L. E. Murr, *Journal of Metals*, 33, 21 (1981). 102

[44] J. E. Vorthman and G. E. Duvall, *Journal of Applied Physics*, 53(5), 3607 (1982). DOI: 10.1063/1.331140 45

[45] A. Sawaoka, S. Soga, and K. Kondo, *Journal of Materials Science Letters*, 1(8), 347 (1982).

[46] L. Davison, D. Webb, and R. Graham, in *AIP Conference Proceedings*, vol. 78, pp. 67–71, (1982). 45, 48

[47] Announcement, Dr. C. S. Smith becomes professor at MIT, The Tech, vol. 81, no. 4, Cambridge, MA, March 3 (1961). 4, 6

[48] Cyril Stanley Smith Dies at 88, MIT News, Massachusetts Institute of Technology, vol. 37, no. 4, September 2 (1992). 4, 6

[49] C. S. Smith, *A History of Metallography: The Development of Ideas on the Structure of Metals Before 1890*, University of Chicago Press Chicago (1960). 7

[50] C. S. Smith, *From Art to Science: Seventy-Two Objects Illustrating the Nature of Discovery*, MIT Press, Cambridge, MA (1980).

[51] C. S. Smith, *Art and History*, MIT Press, Cambridge, MA, (1981). 7

[52] R. L. Nolder and G. Thomas, *Acta Metallurgica*, 12(2), 227 (1964). 7, 11

[53] H. E. Read, J. R. Triplett, and R. A. Cecil, Dislocation dynamics and the formulation of constitutive equations for rate-dependent plastic flow in metals. *Technical Report*, Systems Science and Software, La Jolla, CA (1970). 7, 9

[54] G. Gray III and P. Follansbee. *Shock Waves in Condensed Matter* (1988). 7

[55] G. Gray III and C. Morris, Influence of peak pressure on the substructure evolution and shock wave profiles of ti-6al-4v. *Technical Report*, Los Alamos National Lab., NM (1988). 7, 75, 79

[56] F. Cao, I. J. Beyerlein, F. L. Addessio, B. H. Sencer, C. P. Trujillo, E. K. Cerreta, and G. T. Gray III, *Acta Materialia*, 58(2), 549 (2010). 7, 62

[57] D. Peckner, *The Strengthening of Metals*, Reinhold, New York (1964).

[58] M. A. Meyers, *Dynamic Behavior of Materials*, John Wiley & Sons (1994). DOI: 10.1002/9780470172278 9, 21, 52, 53, 54, 57, 58

[59] G. Gray, *Acta Metallurgica*, 36(7), 1745 (1988). 7, 62, 63

[60] E. Cerreta, G. Gray, R. Hixson, P. Rigg, and D. Brown, *Acta Materialia*, 53(6), 1751 (2005). 7, 58, 75, 76, 77, 102

[61] N. Bourne, J. Millett, and G. Gray, *Journal of Materials Science*, 44(13), 3319 (2009). 48, 49, 52, 91

[62] F. Zhang, M. Hao, F. Wang, C. Tan, X. Yu, H. Ma, and H. Cai, *Scripta Materialia*, 67(12), 951 (2012).

[63] G. Kanel, G. Garkushin, A. Savinykh, S. Razorenov, T. de Resseguier, W. Proud, and M. Tyutin, *Journal of Applied Physics*, 116(14), 143504 (2014). DOI: 10.1063/1.4897555 91

[64] E. Cerreta, G. Gray III, A. Lawson, T. Mason, and C. Morris, *Journal of Applied Physics*, 100(1), 013530 (2006). DOI: 10.1063/1.2209540 7, 58, 76, 78, 79

[65] G. Gray, P. Follansbee, and C. Frantz, *Materials Science and Engineering: A*, 111, 9 (1989). 7, 62

[66] M. A. Meyers, U. R. Andrade, and A. H. Chokshi, *Metallurgical and Materials Transactions A*, 26(11), 2881 (1995). 7, 62

[67] L. E. Murr and E. Esquivel, *Journal of Materials Science*, 39(4), 1153 (2004). 7

[68] J. Johnson and R. Rohde, *Journal of Applied Physics*, 42(11), 4171 (1971). DOI: 10.1063/1.1659750 7, 11

[69] L. M. Dougherty, G. Gray, E. K. Cerreta, R. J. McCabe, R. D. Field, and J. F. Bingert, *Scripta Materialia*, 60(9), 772 (2009). 7

[70] L. Murr, M. Meyers, C. S. Niou, Y. Chen, S. Pappu, and C. Kennedy, *Acta Materialia*, 45(1), 157 (1997). 7, 11, 69

[71] L. Hsiung and D. Lassila, *Acta Materialia*, 48(20), 4851 (2000). 69, 70

[72] G. T. Gray and K. S. Vecchio, *Metallurgical and Materials Transactions A*, 26(10), 2555 (1995). 69

[73] J. N. Florando, N. R. Barton, B. S. El-Dasher, J. M. McNaney, and M. Kumar, *Journal of Applied Physics*, 113(8), 083522 (2013).s DOI: 10.1063/1.4792227

[74] A. Zurek, W. Thissell, J. Johnson, D. Tonks, and R. Hixson, *Journal of Materials Processing Technology*, 60(1–4), 261 (1996). 7, 13, 57

[75] W. G. Johnston and J. J. Gilman, *Journal of Applied Physics*, 30(2), 129 (1959). DOI: 10.1063/1.1735121 8

[76] J. J. Gilman, *Applied Mechanics Reviews*, 21(8), 767 (1968). 9

[77] P. Follansbee, The rate dependence of structure evolution in copper and its influence on the stress-strain behavior at very high strain rates. *Technical Report*, Los Alamos National Lab., NM (1987).

[78] U. Messerschmidt, *Dislocation Dynamics During Plastic Deformation*, vol. 129, Springer Science and Business Media (2010). DOI: 10.1007/978-3-642-03177-9. 9, 58, 62

[79] E. Orowan, et al., *AIME*, 131, New York (1954). 9

[80] G. E. Duvall, *Stress Waves in Anelastic Solids*, pp. 20–32 (1964). 9

[81] J. W. Taylor, *Journal of Applied Physics*, 36(10), 3146 (1965). DOI: 10.1063/1.1702940 9

[82] A. Seeger, et al., *Dislocations and Mechanical Properties of Crystals*, p. 243, Wiley, New York (1957). 9

[83] P. Follansbee and U. Kocks, *Acta Metallurgica*, 36(1), 81 (1988). 9

[84] A. Granato, Microscopic mechanisms of dislocation drag, in *Metallurgical Effects at High Strain Rates*, Rohde, R. W., Butcher, B. M., Holland, J. R., and Karnes, C. H., Plenum Press, New York (1973). 9

[85] J. P. Hirth and J. Lothe, *Theory of Dislocations*, 2nd ed., John Willey & Sons (1982). 9

[86] P. P. Gillis, J. J. Gilman, and J. W. Taylor, *Philosophical Magazine*, 20(164), 279 (1969). 10

[87] J. Eshelby, *Proc. of the Physical Society. Section A*, 62(5), 307 (1949). 10

[88] P. Gumbsch and H. Gao, *Science*, 283(5404), 965 (1999).

[89] E. Hahn, S. Zhao, E. Bringa, and M. Meyers, *Scientific Reports*, 6 (2016).

[90] F. Frank and J. Van der Merwe, in *Proc. of the Royal Society of London A: Mathematical, Physical and Engineering Sciences*, vol. 201, pp. 261–268 (1950).

[91] J. Weertman, *Journal of Applied Physics*, 38(13), 5293 (1967). DOI: 10.1063/1.1709317 10

[92] R. von Mises, *ZAMM-Journal of Applied Mathematics and Mechanics/Zeitschrift für Angewandte Mathematik und Mechanik*, 8(3), 161 (1928). 10

[93] N. Munroe, X. Tan, and H. Gu, *Scripta Materialia*, 36(12), 1383 (1997). 11

[94] A. Staroselsky and L. Anand, *International Journal of Plasticity* 19(10), 1843 (2003).

[95] Y. Wang and J. Huang, *Acta Materialia*, 55(3), 897 (2007).

[96] M. Yoo, *Metallurgical Transactions A*, 12(3), 409 (1981). 75

[97] S. Agnew, C. Tomé, D. Brown, T. Holden, and S. Vogel, *Scripta Materialia*, 48(8), 1003 (2003).

[98] A. Akhtar, *Metallurgical and Materials Transactions A*, 6(5), 1105 (1975).

[99] M. Yoo, J. Morris, K. Ho, and S. Agnew, *Metallurgical and Materials Transactions A*, 33(3), 813 (2002).

[100] S. Mahajan and D. Williams, *International Metallurgical Reviews*, 18(2), 43 (1973). 11

[101] O. Bouaziz, S. Allain, C. Scott, P. Cugy, and D. Barbier, *Current Opinion in Solid State and Materials Science*, 15(4), 141 (2011). 11

[102] F. R. N. Nabarro, Z. S. Basinski, and D. Holt, *Advances in Physics*, 13(50), 193 (1964).

[103] F. Rosi, *AIME TRANS*, 200, 1009 (1954).

[104] J. Cox, G. Horne, and R. Mehl, *Transactions of the American Society for Metals*, 49, 118 (1957).

[105] C. S. Barrett, *Structure of Metals*, McGraw-Hill Book Company, Inc., New York (1943).

[106] A. Seeger, in *Encyclopedia of Physics*, A. Flugge, Ed., vol. 7/2, Springer, Berlin, (Crystal Physics II), p. 1 (1958). DOI: 10.1007/978-3-642-45890-3

[107] R. W. Hertzberg, Elements of fracture mechanics, *Deformation and Fracture Mechanics of Engineering Materials* (1989).

[108] J. A. Jensen and W. Backofen, *Canadian Metallurgical Quarterly*, 11(1), 39 (1972).

[109] J. R. Asay and M. Shahinpoor, *High-Pressure Shock Compression of Solids*, Springer Science and Business Media (2012). DOI: 10.1007/978-1-4612-0911-9 11, 24, 43

[110] L. Davison and R. A. Graham, *Physics Reports*, 55(4), 255 (1979).

[111] M. A. Meyers, F. Gregori, B. Kad, M. Schneider, D. Kalantar, B. Remington, G. Ravichandran, T. Boehly, and J. Wark, *Acta Materialia*, 51(5), 1211, (2003).

[112] A. Rohatgi, K. Vecchio, and G. Gray III, *Acta Materialia*, 49(3), 427 (2001). 11, 13

[113] C. Wehrenberg, D. McGonegle, C. Bolme, A. Higginbotham, A. Lazicki, H. Lee, B. Nagler, H. Park, B. Remington, R. Rudd, et al., *Nature*, 550(7677), 496 (2017). 19, 109

[114] T. de Rességuier, S. Hemery, E. Lescoute, P. Villechaise, G. Kanel, and S. Razorenov, *Journal of Applied Physics*, 121(16), 165104 (2017). DOI: 10.1063/1.4982352 11

[115] L. Chhabildas and C. Hills, *Metallurgical Application of Shock Waves and High-Strain-Rate Phenomena*, L. E. Murr et al., Eds., Basel, pp. 429–448 (1986). 11

[116] R. Nolder and G. Thomas, *Acta Metallurgica*, 11(8), 994 (1963). 11

[117] A. R. Champion and R. Rohde, *Journal of Applied Physics*, 41(5), 2213 (1970). DOI: 10.1063/1.1659190 11

[118] K. Wongwiwat and L. Murr, *Materials Science and Engineering*, 35(2), 273 (1978). 11, 13, 69

[119] R. Rohde, W. Leslie, and R. Glenn, *Metallurgical Transactions*, 3, 323, (1972). 11, 13

[120] S. Mahajan, *Physica Status Solidi (b)*, 33(1), 291 (1969). 11, 13

[121] H. Kestenbach and M. A. Meyers, *Metallurgical Transactions A* 7(12), 1943 (1976). 11, 13

[122] O. Johari and G. Thomas, *Acta Metallurgica*, 12(10), 1153 (1964). 11, 13

[123] R. DeAngelis and J. Cohen, Some crystallographic techniques for the study of mechanical twinning and their application to shock-induced twinning in copper. *Technical Report*, Northwestern University Evanston, IL Technological Institute (1963). DOI: 10.21236/ad0403801 11

[124] F. Greulich and L. Murr, *Materials Science and Engineering*, 39(1), 81, (1979). 11, 66, 67

[125] F. Grace, M. Inman, and L. Murr, *Journal of Physics D: Applied Physics*, 1(11), 1437 (1968). DOI: 10.1088/0022-3727/1/11/307 11

[126] A. Appleton and J. Waddington, *Acta Metallurgica*, 12, 681 (1963). 11

[127] S. Mahajan, *Physica Status Solidi (a)*, 2(2), 217 (1970). 13

[128] T. Antoun, L. Seaman, D. Curran, G. Kanel, S. Razorenov, and A. Utkin, *Spall Fracture (Shock Wave and High Pressure Phenomena)* (2003). 13, 15

[129] B. Hopkinson, *Philosophical Transactions of the Royal Society of London. Series A, Containing Papers of a Mathematical or Physical Character*, 213, 437 (1914). 13, 14

[130] D. Grady, *Journal of the Mechanics and Physics of Solids*, 36(3), 353 (1988). 13, 102

[131] G. Kanel, *Journal of Applied Mechanics and Technical Physics*, 42, 358 (2001).

[132] X. Chen, J. Asay, S. Dwivedi, and D. Field, *Journal of Applied Physics*, 99(2), 023528 (2006). DOI: 10.1063/1.2165409

[133] P. Trivedi, J. Asay, Y. Gupta, and D. Field, *Journal of Applied Physics*, 102(8), 083513, (2007). DOI: 10.1063/1.2798497 79

[134] G. Kanel, S. Razorenov, A. Utkin, and D. Grady, in *AIP Conference Proceedings*, vol. 370, pp. 503–506 (1996). 79

[135] E. Moshe, S. Eliezer, E. Dekel, A. Ludmirsky, Z. Henis, M. Werdiger, I. Goldberg, N. Eliaz, and D. Eliezer, *Journal of Applied Physics*, 83(8), 4004 (1998). DOI: 10.1063/1.367222

[136] G. Kanel, S. Razorenov, A. Utkin, V. Fortov, K. Baumung, H. Karow, D. Rusch, and V. Licht, *Journal of Applied Physics*, 74(12), 7162 (1993). DOI: 10.1063/1.355032

[137] G. Kanel, S. Razorenov, A. Bogatch, A. Utkin, V. Fortov, and D. Grady, *Journal of Applied Physics*, 79(11), 8310 (1996). DOI: 10.1063/1.362542

[138] C. Williams, K. Ramesh, and D. Dandekar, *Journal of Applied Physics*, 111(12), 123528 (2012). DOI: 10.1063/1.4729305 58, 79, 80

[139] C. Williams, C. Chen, K. Ramesh, and D. Dandekar, *Journal of Applied Physics*, 114(9), 093502 (2013). DOI: 10.1063/1.4817844 79, 80

[140] L. Farbaniec, C. Williams, L. Kecskes, K. Ramesh, and R. Becker, *International Journal of Impact Engineering*, 98, 34 (2016). 91, 93, 94, 95, 96

[141] C. Williams, T. Sano, T. Walter, J. Bradley, and L. Kecskes, *Journal of Dynamic Behavior of Materials*, 2(4), 476 (2016). 80, 82, 83

[142] R. Whelchel, N. Thadhani, T. Sanders, L. Kecskes, and C. Williams, in *Journal of Physics: Conference Series*, vol. 500, IOP Publishing, 112066 (2014). 13

[143] J. Smith, in *Symposium on Dynamic Behavior of Materials* ASTM International (1963). 13

[144] I. Skidmore, *Applied Materials Research*, 4(3), 131 (1965). 14

[145] B. Breed, C. L. Mader, and D. Venable, *Journal of Applied Physics*, 38(8), 3271 (1967). DOI: 10.1063/1.1710098 14

[146] F. R. Tuler and B. M. Butcher, *International Journal of Fracture*, 4(4), 431 (1968). 14

[147] S. Arrhenius, *Zeitschrift für Physikalische Chemie*, 4(1), 226 (1889). 14

[148] A. Tobolsky and H. Eyring, *The Journal of Chemical Physics*, 11(3), 125 (1943). 15

[149] S. N. Zhurkov, in *ICF1*, Japan (1965). 15

[150] D. Curran, L. Seaman, and D. Shockey, *Physics Reports*, 147(5–6), 253 (1987). 15, 79

[151] P. Rigg and Y. Gupta, *Applied Physics Letters*, 73(12), 1655 (1998). 15

[152] Y. Gupta, K. Zimmerman, P. Rigg, E. Zaretsky, D. Savage, and P. Bellamy, *Review of Scientific Instruments*, 70(10), 4008 (1999).

[153] S. J. Turneaure and Y. Gupta, *Journal of Applied Physics*, 106(3), 033513 (2009). DOI: 10.1063/1.3187929 19, 109

[154] L. Barker and R. Hollenbach, *Review of Scientific Instruments*, 36(11), 1617 (1965).

[155] L. Barker and R. Hollenbach, *Journal of Applied Physics*, 43(11), 4669 (1972). DOI: 10.1063/1.1660986

[156] O. T. Strand, D. Goosman, C. Martinez, T. Whitworth, and W. Kuhlow, *Review of Scientific Instruments*, 77(8), 083108 (2006). 15

[157] D. R. Curran, L. Seaman, and D. A. Shockey, *Physics Today*, 30, 46 (1977). 15

[158] D. Curran, D. Shockey, and L. Seaman, *Journal of Applied Physics*, 44(9), 4025 (1973). DOI: 10.1063/1.1662891

[159] J. Kalthoff and D. Shockey, *Journal of Applied Physics*, 48(3), 986 (1977). DOI: 10.1063/1.323720 15

[160] R. Graham, in *High-Pressure Shock Compression of Solids*, pp. 1–6, Springer (1993). DOI: 10.1007/978-1-4612-0911-9_1 15

[161] R. Graham, in *High-Pressure Science and Technology*, pp. 1886–1901, Springer (1979).

[162] L. Chhabildas and R. Graham, Developments in measurement techniques for shock-loaded solids. *Technical Report*, Sandia National Labs., Albuquerque, NM (1987).

[163] L. V. Al'tshuler, *Physics-Uspekhi*, 8(1), 52 (1965). 15, 32

[164] G. Kanel, *Combustion, Explosion and Shock Waves*, 18, 329 (1982).

[165] S. Razorenov and G. Kanel, *Physics of Metals and Metallography*, 74(5), 526 (1992).

[166] S. Cochran and D. Banner, *Journal of Applied Physics*, 48(7), 2729 (1977). DOI: 10.1063/1.324125

[167] J. Millett, M. Cotton, N. Bourne, N. Park, and G. Whiteman, *Journal of Applied Physics*, 115(7), 073506 (2014). DOI: 10.1063/1.4838037

[168] G. Kanel, S. Razorenov, A. Utkin, K. Baumung, H. Karow, and V. Licht, in *AIP Conference Proceedings*, vol. 309, pp. 1043–1046 (1994).

[169] L. Farbaniec, C. Williams, L. Kecskes, R. Becker, and K. Ramesh, *Materials Science and Engineering: A*, 707, 725 (2017). 91, 96, 97, 98, 99

[170] Y. Me-Bar, M. Boas, and Z. Rosenberg, *Materials Science and Engineering*, 85, 77 (1987). 91

[171] C. D. Adams, W. W. Anderson, G. T. Gray III, W. R. Blumenthal, C. T. Owens, F. J. Freibert, J. M. Montoya, and P. J. Contreras, in *AIP Conference Proceedings*, vol. 1195, pp. 509–512 (2009).

[172] S. Razorenov, A. Bogatch, G. Kanel, A. Utkin, V. Fortov, and D. Grady, in *AIP Conference Proceedings*, vol. 429, pp. 447–450 (1998).

[173] J. Belak, *Journal of Computer-Aided Materials Design*, 9(2), 165 (2002). 18

[174] N. Barton, J. Bernier, R. Becker, A. Arsenlis, R. Cavallo, J. Marian, M. Rhee, H. S. Park, B. Remington, and R. Olson, *Journal of Applied Physics*, 109(7), 073501 (2011). DOI: 10.1063/1.3553718

[175] F. L. Addessio, C. A. Bronkhorst, C. A. Bolme, D. W. Brown, E. K. Cerreta, R. A. Lebensohn, T. Lookman, D. J. Luscher, J. R. Mayeur, B. M. Morrow, et al., A high-rate, single-crystal model including phase transformations, plastic slip, and twinning. *Technical Report*, Los Alamos National Lab. (LANL), Los Alamos, NM (2016). DOI: 10.2172/1312644

[176] N. Barton and M. Rhee, *Journal of Applied Physics*, 114(12), 123507 (2013). DOI: 10.1063/1.4822027

[177] G. Agarwal, R. R. Valisetty, R. R. Namburu, A. M. Rajendran, and A. M. Dongare, *Scientific Reports*, 7(1), 12376 (2017).

[178] J. Wilkerson, *International Journal of Plasticity*, 95, 21 (2017).

[179] T. Vogler and J. D. Clayton, *Journal of the Mechanics and Physics of Solids*, 56(2), 297 (2008).

[180] M. A. Shehadeh, H. M. Zbib, and T. D. De la Rubia, *International Journal of Plasticity*, 21(12), 2369 (2005).

[181] X. Li and E. Weinan, *Journal of the Mechanics and Physics of Solids*, 53(7), 1650 (2005).

[182] J. Lloyd, J. Clayton, R. Becker, and D. McDowell, *International Journal of Plasticity*, 60, 118 (2014).

[183] R. A. Austin and D. L. McDowell, *International Journal of Plasticity*, 27(1), 1 (2011).

[184] R. A. Austin and D. L. McDowell, *International Journal of Plasticity*, 32, 134 (2012).

[185] J. Lloyd, J. Clayton, R. Austin, and D. McDowell, *Journal of the Mechanics and Physics of Solids*, 69, 14 (2014).

[186] E. Bringa, K. Rosolankova, R. Rudd, B. Remington, J. Wark, M. Duchaineau, D. Kalantar, J. Hawreliak, and J. Belak, *Nature Materials*, 5(10), 805 (2006).

[187] M. Meyers, H. Jarmakani, E. Bringa, and B. Remington, *Dislocations in Solids*, 15, 91 (2009). 18

[188] J. A. Hawreliak, B. El-Dasher, H. Lorenzana, G. Kimminau, A. Higginbotham, B. Nagler, S. M. Vinko, W. J. Murphy, T. Whitcher, J. S. Wark, et al., *Physical Review B*, 83(14), 144114 (2011). 19

[189] D. Milathianaki, S. Boutet, G. Williams, A. Higginbotham, D. Ratner, A. Gleason, M. Messerschmidt, M. M. Seibert, D. Swift, P. Hering, et al., *Science*, 342(6155), 220 (2013).

[190] A. Loveridge-Smith, A. Allen, J. Belak, T. Boehly, A. Hauer, B. Holian, D. Kalantar, G. Kyrala, R. Lee, P. Lomdahl, et al., *Physical Review Letters*, 86(11), 2349 (2001).

[191] S. Luo, B. Jensen, D. Hooks, K. Fezzaa, K. Ramos, J. Yeager, K. Kwiatkowski, and T. Shimada, *Review of Scientific Instruments*, 83(7), 073903 (2012). 109

[192] S. J. Turneaure, S. M. Sharma, T. J. Volz, J. Winey, and Y. M. Gupta, *Science Advances*, 3(10), eaao3561 (2017). 109

[193] M. J. Suggit, A. Higginbotham, J. A. Hawreliak, G. Mogni, G. Kimminau, P. Dunne, A. J. Comley, N. Park, B. A. Remington, and J. S. Wark, *Nature Communications*, 3, 1224 (2012). 19

[194] H. Kolsky, *Stress Waves in Solids*, vol. 1098, Courier Corporation (1963). 21

[195] J. Achenbach, *Wave Propagation in Elastic Solids*, vol. 16, Elsevier (2012). 21

[196] D. S. Drumheller, *Introduction to Wave Propagation in Nonlinear Fluids and Solids*, Cambridge University Press (1998). 21, 24, 38, 43

[197] G. B. Whitham, *Linear and Nonlinear Waves*, vol. 42, John Wiley & Sons (2011). DOI: 10.1002/9781118032954. 21

[198] R. J. Wasley, *Stress Wave Propagation in Solids: An Introduction*, vol. 7, M. Dekker (1973). 21

[199] A. Eringen and E. Suhubi, *Elastodynamics*, vol. II, New York, Academic Press (1975). 21

[200] R. Courant and K. O. Friedrichs, *Supersonic Flow and Shock Waves*, vol. 21, Springer Science and Business Media (1999). DOI: 10.1007/978-1-4684-9364-1 21, 24

[201] D. Grady, *Physics of Shock and Impact, Fundamentals and Dynamic Failure*, vol. 1, IOP Publishing, Bristol, UK (2017). 21

[202] D. Grady, *Physics of Shock and Impact, Materials and Shock Response*, vol. 2, IOP Publishing, Bristol, UK, (2017). 21

[203] W. Johnson, *Impact Strength of Materials*, Edward Arnold London (1972). 21

[204] P. C. Chou and A. K. Hopkins, Dynamic response of materials to intense impulsive loading, Air Force Materials Lab Wright-Patterson AFB, OH (1972). 24

[205] H. W. Liepmann and A. Roshko, *Elements of Gasdynamics*, Courier Corporation (1957). DOI: 10.1063/1.3060140

[206] G. Emanuel, Gasdynamics: Theory and applications, *American Institute of Aeronautics and Astronautics* (1986).

[207] L. Landau and E. Lifshitz, *Course of Theoretical Physics*, (1987).

[208] G. G. Roger, *Selected Topics in Shock Wave Physics and Equation of State Modeling*, World Scientific (1994). DOI: 10.1142/2290 24, 47

[209] G. Duvall and G. Fowles, in *High Pressure Physics and Chemistry*, vol. 2, p. 209 (1963). 24, 42

[210] O. Krokhin. *Physics of High Energy Density*, Eds., P. Caldirola and H. Knoepfel (1971). 32

[211] G. I. Kanel, S. V. Razorenov, and V. E. Fortov, *Shock-Wave Phenomena and the Properties of Condensed Matter* Springer Science and Business Media (2013). DOI: 10.1007/978-1-4757-4282-4 38, 43

[212] Y. B. Zel'Dovich and Y. P. Raizer, Physics of shock waves and high-temperature hydrodynamic phenomena, no. FTD-MT-64-514, Foreing Technology DIV Wright-Patterson AFB, OH (1965). 24, 37, 38

[213] M. Boslough and J. Asay, *High-Pressure Shock Compression of Solids*, pp. 7–42 (1993). DOI: 10.1007/978-1-4612-0911-9_2 25, 26

[214] J. O. Erkman, *Journal of Applied Physics*, 32(5), 939 (1961). DOI: 10.1063/1.1736137 27, 89

[215] L. Al'Tshuler, M. Pavlovskii, and V. Drakin, *Soviet Physics JETP*, 25, 260 (1967).

[216] B. J. Jensen, G. Gray III, and R. S. Hixson, *Journal of Applied Physics*, 105(10), 103502 (2009). DOI: 10.1063/1.3110188 27

[217] W. M. Rankine, *Philosophical Transactions of the Royal Society of London*, pp. 277–288 (1870). 27

[218] H. Hugoniot, in *Classic Papers in Shock Compression Science*, pp. 161–243, Springer, (1998). DOI: 10.1007/978-1-4612-2218-7_7 27

[219] M. Rice, R. G. McQueen, and J. Walsh, *Solid State Physics*, 6, 1 (1958). 32, 38

[220] D. M. S. *Mechanics*, New York, (1976). 37

[221] E. Royce, in *Physics of High Energy Density*, p. 80 (1971).

[222] S. B. Segletes, An analysis on the stability of the Mie-gruneisen equation of state for describing the behavior of shock-loaded materials. *Technical Report*, Army Ballistic Research Lab., Aberdeen Proving Ground, MD (1991). 37, 38

[223] J. M. Walsh, M. H. Rice, R. G. McQueen, and F. L. Yarger, *Physical Review*, 108(2), 196 (1957).

[224] R. McQueen and S. Marsh, *Journal of Applied Physics*, 31(7), 1253 (1960). DOI: 10.1063/1.1735815

[225] T. Ahrens, *High-Pressure Shock Compression of Solids*, 1, 75 (1993).

[226] L. Al'Tshuler, S. Brusnikin, and E. Kuz'menkov, *Journal of Applied Mechanics and Technical Physics*, 28(1), 129 (1987).

[227] R. Menikoff, in *ShockWave Science and Technology Reference Library*, pp. 143–188, Springer (2007). DOI: 10.1007/978-3-540-68408-4_4 38

[228] L. W. Morland, *Philosophical Transactions of the Royal Society of London A: Mathematical, Physical and Engineering Sciences*, 251(997), 341 (1959). 38

[229] G. Duvall, Shock waves and equations of state, *Dynamic Response of Materials to Intense Impulsive Loading*, pp. 89-121 (1972). 38

[230] G. Duvall. *Physics of High Energy Density* (1971). 43

[231] M. Wilkins, et al., *Methods in Computational Physics*, 3(1), 211 (1964).

[232] R. Clifton, *Mechanics Today*, 1, 102 (1974).

[233] F. A. McClintock and A. S. Argon, *Books*, (1966).

[234] W. Herrmann, Constitutive equation for the dynamic compaction of ductile porous materials, *Journal of Applied Physics*, 40, no. 6, pp. 2490-2499 (1969). 38

[235] J. A. Zukas, T. Nicholas, H. F. Swift, L. B. Greszczuk, D. R. Curran, and L. Malvern, *Journal of Applied Mechanics*, 50, 702 (1983). 42, 43

[236] C. Williams, C. Chen, K. Ramesh, and D. Dandekar, *Materials Science and Engineering: A*, 618, 596 (2014). 45, 50, 51, 52, 57, 58, 60, 61, 62, 80, 81

[237] N. N. Thadhani, *Progress in Materials Science*, 37(2), 117 (1993). 53, 54

[238] D. A. Fredenburg, N. N. Thadhani, and T. J. Vogler, *Materials Science and Engineering: A*, 527(15), 3349 (2010).

[239] X. Xu and N. N. Thadhani, *Scripta Materialia*, 44(10), 2477 (2001). 45

[240] C. Williams, D. Scheffler, and W. Walters, *Proc. Engineering*, 58, 453 (2013). 46

[241] R. Rabie, J. Vorthman, and J. Dienes, in *Shock Waves in Condensed Matter 1983*, pp. 199–202, Elsevier (1984). 48

[242] R. Vignjevic, K. Hughes, T. De Vuyst, N. Djordjevic, J. C. Campbell, M. Stojkovic, O. Gulavani, and S. Hiermaier, *International Journal of Impact Engineering*, 77, 16 (2015).

[243] G. Raiser, R. Clifton, and M. Ortiz, *Mechanics of Materials*, 10(1–2), 43, (1990). 48

[244] L. E. Murr, Shock waves for industrial applications (1988). 52, 53, 54, 57, 59, 102

[245] O. Bergmann and N. Bailey, *Transactions on Technology*, pp. 67–85 (1987). 53

[246] T. Akashi and A. B. Sawaoka, *Journal of Materials Science*, 22(3), 1127 (1987). 53

[247] K. I. Kondo, S. Soga, A. Sawaoka, and M. Araki, *Journal of Materials Science*, 20(3), 1033 (1985). 53, 102

[248] R. A. Graham and A. B. Sawaoka, High pressure explosive processing of ceramics (1986). 53

[249] W. Gourdin, *Progress in Materials Science*, 30(1), 39, (1986). http://www.sciencedirect.com/science/article/pii/0079642586900034 53, 54

[250] R. Prümmer, in *Explosivverdichtung Pulvriger Substanzen*, pp. 89–97, Springer (1987). DOI: 10.1007/978-3-642-82903-1_13 53

[251] N. Thadhani, *Material and Manufacturing Process*, 3(4), 493 (1988). 53, 54, 102

[252] A. B. Sawaoka, *Shock Waves in Materials Science*, Springer Science and Business Media (2012). DOI: 10.1007/978-4-431-68240-0 53

[253] L. E. Murr, in *Handbook of Materials Structures, Properties, Processing and Performance*, pp. 863–889, Springer (2015). DOI: 10.1007/978-3-319-01905-5 53, 54

[254] P. W. Cooper, *Explosives Engineering*, VCH Pub (1996). 54, 55

[255] P. W. Cooper, S. R. Kurowski, and P. W. Cooper, *Introduction to the Technology of Explosives*, VCH New York (1996).

[256] P. Cooper, J. Zukas, and W. Walters, *Explosive Effects and Applications* (2003). 54, 55

[257] K. Staudhammer and K. Johnson, *Metallurgical Application of Shock-Wave and High-Strain-Rate Phenomena*, p. 149, Marcel Dekker, New York (1986). 55

[258] E. Carton, H. Verbeek, M. Stuivinga, and J. Schoonman, *Journal of Applied Physics*, 81(7), 3038 (1997). DOI: 10.1063/1.364338 55

[259] M. Nishida, A. Chiba, K. Imamura, T. Yamaguchi, and H. Minato, *Metallurgical Transactions A*, 20(12), 2831 (1989). 55

[260] M. Meyers and S. Wang, *Acta Metallurgica*, 36(4), 925 (1988). 55

[261] D. Shockey, L. Seaman, and D. Curran, *International Journal of Fracture*, 27(3–4), 145 (1985). 57

[262] D. Shockey, L. Seaman, and D. Curran, in *Metallurgical Effects at High Strain Rates*, pp. 473–499, Springer (1973). DOI: 10.1007/978-1-4615-8696-8_27 79, 97

[263] L. Seaman, T. Barbee Jr, and D. Curran, Dynamic fracture criteria of homogeneous materials, *Technical Report*, Stanford Research Institute, Menlo Park, CA (1972). 89

[264] P. Chevrier and J. Klepaczko, *Engineering Fracture Mechanics*, 63(3), 273 (1999). 57, 89

[265] G. Gray III and J. Huang, *Materials Science and Engineering: A*, 145(1), 21 (1991). 57, 62, 63, 79

[266] L. Murr, in *Shock Waves and High-Strain-Rate Phenomena in Metals*, pp. 753–777, Springer (1981). DOI: 10.1007/978-1-4613-3219-0_42 57, 58, 79

[267] M. A. Meyers, *Metallurgical Transactions A*, 8(10), 1581 (1977). 57, 58

[268] D. H. Lassila, T. Shen, B. Y. Cao, and M. A. Meyers, *Metallurgical and Materials Transactions A*, 35(9), 2729 (2004). 57, 62

[269] U. Kocks, *Dislocations and Properties of Real Materials*, pp. 125–143 (1984). 57, 58

[270] U. Essmann and H. Mughrabi, *Philosophical Magazine A*, 40(6), 731 (1979). 58

[271] G. Gray III, Deformation substructures induced by high-rate deformation. *Technical Report*, Los Alamos National Lab., NM, (1991). 62

[272] J. G. Sevillano, P. Van Houtte, and E. Aernoudt, *Progress in Materials Science*, 25(2–4), 69 (1980).

[273] F. Cheval and L. Priester, *Scripta Metallurgica*, 23(11), 1871 (1989). 58

[274] J. J. Gilman, *Journal of Applied Physics*, 33(9), 2703 (1962). DOI: 10.1063/1.1702535 58, 62

[275] R. J. Amodeo and N. M. Ghoniem, *Res Mechanica*, 23(2–3), 137 (1988). 58

[276] H. Conrad, *JOM*, 16(7), 582 (1964). 58

[277] P. Thornton, T. Mitchell, and P. Hirsch, *Philosophical Magazine*, 7(80), 1349 (1962).

[278] A. Rohatgi, K. S. Vecchio, and G. T. Gray, *Metallurgical and Materials Transactions A*, 32(1), 135 (2001).

[279] W. Püschl, *Progress in Materials Science*, 47(4), 415 (2002).

[280] I. Karaman, H. Sehitoglu, Y. Chumlyakov, and H. Maier, *JOM*, 54(7), 31 (2002). 58

[281] T. Alden, *Metallurgical Transactions A*, 7(8), 1057 (1976). 58

[282] B. H. Sencer, S. A. Maloy, and G. T. Gray III, *Acta Materialia*, 53(11), 3293 (2005). 58, 62, 64, 65

[283] G. Gray, R. Hixson, and C. Morris, in *Shock Compression of Condensed Matter–1991*, pp. 427–430, Elsevier (1992).

[284] B. Kazmi and L. Murr, in *Shock Waves and High-Strain-Rate Phenomena in Metals*, pp. 733–752, Springer (1981). DOI: 10.1007/978-1-4613-3219-0_41

[285] L. Murr. *Shock Waves and High-Strain-Rate Phenomena in Metals*, M. A. Meyers and L. Murr, Eds. (1981). DOI: 10.1007/978-1-4613-3219-0 58, 66

[286] G. Gray III, N. Bourne, and J. Millett, *Journal of Applied Physics*, 94(10), 6430 (2003). DOI: 10.1063/1.1620679 59

[287] G. T. Gray III, in *AIP Conference Proceedings*, vol. 1426, pp. 19–26. 59, 60

[288] R. Wright and D. Mikkola, *Metallurgical Transactions A*, 16(5), 881 (1985). 59

[289] R. Wright and D. Mikkola, *Metallurgical Transactions A* 16(5), 891 (1985). 59

[290] G. Gray III and P. Follansbee, Influence of peak pressure and pulse duration on substructure development and threshold stress measurements in shock-loaded copper. *Technical Report*, Los Alamos National Lab., NM (1987). 59, 79

[291] K. Johnson, L. Murr, and K. Staudhammer, *Acta Metallurgica*, 33(4), 677 (1985). 59

[292] N. Hansen, *Materials Science and Technology*, 6(11), 1039 (1990). 62

[293] B. Bay, N. Hansen, and D. Kuhlmann-Wilsdorf, *Materials Science and Engineering: A*, 158(2), 139 (1992). 62

[294] G. Gray III and P. Follansbee, Influence of peak pressure on the substructure evolution and mechanical properties of shock-loaded 6061-t6 aluminum. *Technical Report*, Los Alamos National Lab., NM (1987). 62

[295] G. Gray III and C. Morris, *Le Journal de Physique IV*, 1(C3), C3 (1991). 62

[296] E. Cerreta, I. Frank, G. Gray III, C. Trujillo, D. Korzekwa, and L. Dougherty, *Materials Science and Engineering: A*, 501(1–2), 207 (2009).

[297] D. Brillhart, R. De Angelis, A. Preban, J. Cohen, and P. Gordon, *Transactions on AIME*, 239, 836 (1967). 68

[298] G. T. Higgins, *Metallurgical Transactions*, 2(5), 1277 (1971).

[299] V. Greenhut, P. Kingman, S. Weissmann, and M. Chen, Deformation substructure of copper single crystals after explosive loading as disclosed by electron-optical and x-ray methods. *Technical Report*, Ballistic Research Labs., Aberdeen Proving Ground, MD (1975).

[300] M. Mogilevskii and L. Bushnev, *Combustion, Explosion, and Shock Waves*, 26(2), 215 (1990).

[301] D. Mikkola and J. Cohen, *Acta Metallurgica*, 14(2), 105 (1966). 62

[302] A. Podurets, V. Raevskii, V. Khanzhin, A. Lebedev, O. Aprelkov, V. Igonin, I. Kondrokhina, A. Balandina, M. Tkachenko, J. Petit, et al., *Combustion, Explosion, and Shock Waves*, 47(5), 606 (2011). 64, 65, 80

[303] A. Perez-Bergquist, E. K. Cerreta, C. P. Trujillo, G. Gray III, C. Brandl, and T. Germann, *Scripta Materialia*, 67(4), 412 (2012). 65, 66

[304] B. Cao, D. H. Lassila, C. Huang, Y. Xu, and M. A. Meyers, *Materials Science and Engineering: A*, 527(3), 424 (2010). 66, 67, 68

[305] L. Murr, *Scripta Metallurgica*, 12(2), 201 (1978). 66

[306] L. Murr and D. Kuhlmann-Wilsdorf, *Acta Metallurgica*, 26(5), 847 (1978).

[307] L. Murr, *Materials at High Strain Rates* (1987).

[308] P. Follansbee and G. Gray, in *Advances in Plasticity*, pp. 385–388, Elsevier (1989).

[309] E. Esquivel, L. Murr, E. Trillo, and M. Baquera, *Journal of Materials Science*, 38(10), 2223 (2003). 67, 68

[310] Y. Wang, E. Bringa, J. McNaney, M. Victoria, A. Caro, A. Hodge, R. Smith, B. Torralva, B. Remington, C. Schuh, et al., *Applied Physics Letters*, 88(6), 061917 (2006). 68, 69

[311] A. Appleton and J. Waddington, *Acta Metallurgica*, 12(8), 956 (1964).

[312] A. Bekrenev, Z. Gelunova, and L. Gerasimenko, *Physics of Metals and Metallography*, 30(5), 109 (1970).

[313] H. Kressel and N. Brown, *Journal of Applied Physics*, 38(4), 1618 (1967). DOI: 10.1063/1.1709733 66, 79

[314] V. Vitek, *Dislocations and Properties of Real Materials*, pp. 30–50 (1984). 69

[315] G. Gray III, Deformation twinning: Influence of strain rate. *Technical Report*, Los Alamos National Lab., NM (1993). 69, 75

[316] L. Hsiung and D. Lassila, *Scripta Materialia*, 38(9) (1998). 69

[317] L. Hsiung and D. Lassila, *Scripta Materialia*, 39(4–5), 603 (1998).

[318] L. L. Hsiung, *Journal of Physics: Condensed Matter*, 22(38), 385702 (2010). 69

[319] C. Wittman, C. Lopatin, R. Garrett Jr, and J. Clark, *Shock-Wave and High-Strain-Rate Phenomena in Materials*, pp. 925–933, Marcel Dekker, Inc. (1992).

[320] J. Huang and G. Gray III, *Materials Science and Engineering: A*, 103(2), 241 (1988). 71, 74

[321] L. Murr, O. Inal, and A. Morales, *Applied Physics Letters*, 28(8), 432 (1976).

[322] M. Meyers, O. Vöhringer, and V. Lubarda, *Acta Materialia*, 49(19), 4025 (2001). 69

[323] L. L. Hsiung, in *AIP Conference Proceedings*, vol. 845, pp. 228–231 (2006). 69

[324] D. Bancroft, E. L. Peterson, and S. Minshall, *Journal of Applied Physics*, 27(3), 291 (1956). DOI: 10.1063/1.1722359 70

[325] L. M. Dougherty, E. K. Cerreta, E. A. Pfeif, C. P. Trujillo, and G. T. Gray III, *Acta Materialia*, 55(18), 6356 (2007). 71, 72

[326] S. Wang, M. Sui, Y. Chen, Q. Lu, E. Ma, X. Pei, Q. Li, and H. Hu, *Scientific Reports*, 3, 1086 (2013). 71, 73

[327] M. Yoo and J. Lee, *Philosophical Magazine A*, 63(5), 987 (1991). 75

[328] K. Ramesh, *Metallurgical and Materials Transactions A*, 33(13), 927 (2002).

[329] P. G. Partridge, *Metallurgical Reviews*, 12(1), 169 (1967).

[330] D. Brown, I. Beyerlein, T. Sisneros, B. Clausen, and C. Tomé, *International Journal of Plasticity*, 29, 120 (2012).

[331] G. Gray III, *Le Journal de Physique IV*, 7(C3), C3 (1997).

[332] G. Subhash, B. Pletka, and G. Ravichandran, *Metallurgical and Materials Transactions A*, 28(7), 1479 (1997).

[333] G. Gray III and P. Follansbee, Influence of strain rate on the substructure evolution and yield behavior of ti-6al-4v. *Technical Report*, Los Alamos National Lab., NM (1988).

[334] R. E. Reed-Hill, The role of deformation twinning in the plastic deformation of zirconium. *Technical Report*, Florida University, Gainesville, FL (1964).

[335] P. Follansbee and G. Gray, *Metallurgical Transactions A*, 20(5), 863 (1989). 75

[336] S. Song and G. Gray III, *Philosophical Magazine A*, 71(2), 275 (1995). 75

[337] G. Jyoti, K. Joshi, S. C. Gupta, and S. Sikka, *Philosophical Magazine Letters*, 75(5), 291 (1997).

[338] G. Dey, R. Tewari, S. Banerjee, G. Jyoti, S. C. Gupta, K. Joshi, and S. Sikka, *Acta Materialia*, 52(18), 5243 (2004). 75

[339] G. T. Gray, *MRS Online Proceedings Library Archive*, 499 (1997). 79

[340] A. Stevens and F. Tuler, *Journal of Applied Physics*, 42(13), 5665 (1971). DOI: 10.1063/1.1659997 79

[341] J. Johnson, G. Gray III, and N. Bourne, *Journal of Applied Physics*, 86(9), 4892 (1999). DOI: 10.1063/1.371527

[342] R. W. Minich, J. U. Cazamias, M. Kumar, and A. J. Schwartz, *Metallurgical and Materials Transactions A*, 35(9), 2663 (2004). 79, 80

[343] J. Escobedo, D. Dennis-Koller, E. Cerreta, B. Patterson, C. Bronkhorst, B. Hansen, D. Tonks, and R. Lebensohn, *Journal of Applied Physics*, 110(3), 033513 (2011). DOI: 10.1063/1.3607294

[344] L. Barker, B. Butcher, C. Lundergan, and D. Munson, *AIAA Journal*, 2(6), 977 (1964).

[345] C. Li, B. Li, J. Huang, H. Ma, M. Zhu, J. Zhu, and S. Luo, *Materials Science and Engineering: A* 660, 139 (2016). 89

[346] G. Kanel, S. Razorenov, K. Baumung, and J. Singer, *Journal of Applied Physics*, 90(1), 136 (2001). DOI: 10.1063/1.1374478 79

[347] J. M. Boteler and D. P. Dandekar, in *AIP Conference Proceedings*, vol. 955, pp. 481–484 (2007). 79

[348] T. Barbee, L. Seaman, and R. Crewdson, Dynamic fracture criteria of homogeneous materials. *Technical Report*, Stanford Research Institute, Menlo Park, CA (1970). 79

[349] Y. Wang, M. Qi, H. He, and L. Wang, *Mechanics of Materials*, 69(1), 270 (2014). 80, 82, 83, 84

[350] D. E. Grady, J. R. Asay, R. W. Rohde, and J. L. Wise, in *Material Behavior Under High Stress and Ultrahigh Loading Rates*, pp. 81–100, Springer (1983). DOI: 10.1007/978-1-4613-3787-4_5

[351] P. Peralta, S. DiGiacomo, S. Hashemian, S. N. Luo, D. Paisley, R. Dickerson, E. Loomis, D. Byler, K. McClellan, and H. D'Armas, *International Journal of Damage Mechanics*, 18(4), 393 (2009). 85, 88

[352] L. Wayne, K. Krishnan, S. DiGiacomo, N. Kovvali, P. Peralta, S. Luo, S. Greenfield, D. Byler, D. Paisley, K. McClellan, et al., *Scripta Materialia*, 63(11), 1065 (2010).

[353] J. Millett, N. Bourne, and G. Gray, *Metallurgical and Materials Transactions A*, 39(2), 322 (2008).

[354] Y. I. Meshcheryakov, A. Divakov, N. Zhigacheva, I. Makarevich, and B. Barakhtin, *Physical Review B*, 78(6), 064301 (2008). 80

[355] J. L. Brewer, D. A. Dalton, E. D. Jackson, A. C. Bernstein, W. Grigsby, E. M. Taleff, and T. Ditmire, *Metallurgical and Materials Transactions A*, 38(11), 2666 (2007). 85, 86, 87

[356] A. Ivanov and S. Novikov, *Zh. Eksp. Teor. Fiz*, 40(6), 1880 (1961). 89

[357] A. Balchan, *Journal of Applied Physics*, 34(2), 241 (1963). DOI: 10.1063/1.1702591

[358] E. Banks, *Journal of the Institute of Metals*, 96(12), 375 (1968). 89

[359] M. A. Meyers, C. Sarzeto, and C. Y. Hsu, *Metallurgical Transactions A*, 11(10), 1737 (1980).

[360] E. Kozlov, *International Journal of High Pressure Research*, 10(3), 541 (1992).

[361] I. Gilath, S. Eliezer, M. P. Dariel, and L. Kornblit, *Journal of Materials Science Letters*, 7(9), 915 (1988).

[362] T. de Rességuier and M. Hallouin, *Physical Review B*, 77(17), 174107 (2008).

[363] A. K. Zurek and M. A. Meyers, in *High-Pressure Shock Compression of Solids II*, pp. 25–70, Springer (1996). DOI: 10.1007/978-1-4612-2320-7_2 89, 90

[364] A. K. Zurek, P. S. Follansbee, and J. Hack, *Metallurgical Transactions A*, 21(1), 431 (1990).

[365] A. Zurek, C. Frantz, and G. Gray III, The influence of shock pre-strain and peak pressure on spall behavior of 4340 steel. *Technical Report*, Los Alamos National Lab., NM (1990). 89, 90

[366] L. Barker and R. Hollenbach, *Journal of Applied Physics*, 45(11), 4872 (1974). DOI: 10.1063/1.1663148 89

[367] M. A. Meyers and K. K. Chawla, *Mechanical Metallurgy: Principles and Applications*, vol. 761, Prentice Hall, Englewood Cliffs, NJ (1984). 89

[368] A. T. Zehnder and A. J. Rosakis, *Journal of the Mechanics and Physics of Solids*, 39(3), 385 (1991). 89

[369] V. Livescu, J. Bingert, and T. Mason, *Materials Science and Engineering: A*, 556, 155 (2012). 89, 90, 91

[370] M. Easton, A. Beer, M. Barnett, C. Davies, G. Dunlop, Y. Durandet, S. Blacket, T. Hilditch, and P. Beggs, *JOM*, 60(11), 57 (2008). 91

[371] I. Polmear, *Materials Science and Technology*, 10(1), 1 (1994).

[372] M. K. Kulekci, *The International Journal of Advanced Manufacturing Technology*, 39(9–10), 851 (2008).

[373] B. Mordike and T. Ebert, *Materials Science and Engineering: A*, 302(1), 37 (2001). 91

[374] R. Boyer, *Materials Science and Engineering: A*, 213(1–2), 103 (1996). 91

[375] I. Polmear, *Light Alloys—Metallurgy of the Light Metals*, London and New York, Edward Arnold, 288 (1989).

[376] C. Leyens and M. Peters, *Titanium and Titanium Alloys: Fundamentals and Applications*, John Wiley & Sons (2003). DOI: 10.1002/3527602119

[377] M. J. Donachie, *Titanium: A Technical Guide*, ASM International (2000).

[378] G. Lütjering and J. C. Williams, *Beta Alloys*, Springer (2007). DOI: 10.1007/978-3-540-71398-2_7

[379] D. Banerjee and J. Williams, *Acta Materialia*, 61(3), 844 (2013). 91

[380] K. Cho, T. Sano, K. Doherty, C. Yen, G. Gazonas, J. Montgomery, P. Moy, B. Davis, and R. DeLorme, Magnesium technology and manufacturing for ultra lightweight armored ground vehicles. *Technical Report*, Army Research Lab., Aberdeen Proving Ground, MD (2009). 91

[381] P. J. Hazell, *Armour: Materials, Theory, and Design*, CRC Press (2015). DOI: 10.1201/b18683

[382] J. R. Klepaczko, P. Chevrier, and X. Boidin, Low-velocity spall testing of ti-6al-4v alloy and a new spall critterion based on meso-scale. *Technical Report*, Metz University, France Lab. of Physics and Mechanics of Materials (2003).

[383] M. Burkins, M. Wells, J. Fanning, and B. Roopchand, The mechanical and ballistic properties of an electron beam single melt of ti-6al-4v plate. *Technical Report*, Army Research Lab. Aberdeen Proving Ground, MD (2001). 91

[384] C. Lemaignan and A. T. Motta, *Materials Science and Technology*, (2006). 91

[385] K. L. Murty, in *Zirconium in the Nuclear Industry: 8th International Symposium*, ASTM International (1989). 91

[386] P. Hazell, G. Appleby-Thomas, E. Wielewski, C. Stennett, and C. Siviour, *Acta Materialia*, 60(17), 6042 (2012). 91, 92, 93, 94

[387] P. Hazell, G. Appleby-Thomas, E. Wielewski, and J. Escobedo, *Philosophical Transactions on the Royal Society of London A*, 372(2023), 20130204 (2014). 102, 103

[388] E. Wielewski, G. Appleby-Thomas, P. Hazell, and A. Hameed, *Materials Science and Engineering: A*, 578, 331 (2013).

[389] Y. Ren, F. Wang, C. Tan, S. Wang, X. Yu, J. Jiang, H. Ma, and H. Cai, *Materials Science and Engineering: A*, 578, 247 (2013).

[390] D. R. Jones, S. J. Fensin, O. Dippo, R. A. Beal, V. Livescu, D. T. Martinez, C. P. Trujillo, J. Florando, M. Kumar, and G. T. Gray III, *Journal of Applied Physics*, 120(13), 135902 (2016). DOI: 10.1063/1.4963279 91, 99, 100, 101

[391] K. Kondoh, E. S. A. Hamada, H. Imai, J. Umeda, and T. Jones, *Materials and Design*, 31(3), 1540 (2010). 96, 108

[392] K. Kondoh, K. Kawabata, and H. Oginuma, *Magnesium Technology*, pp. 433–436 (2007). 96

[393] E. Cerreta, J. Escobedo, P. Rigg, C. Trujillo, D. Brown, T. Sisneros, B. Clausen, M. Lopez, T. Lookman, C. Bronkhorst, et al., *Acta Materialia*, 61(20), 7712 (2013). 102

[394] Z. Rosenberg, *Materials Science and Engineering*, 93, L17 (1987). 102

[395] J. R. Rice and D. M. Tracey, *Journal of the Mechanics and Physics of Solids*, 17(3), 201 (1969).

[396] A. L. Gurson, *Journal of Engineering Materials and Technology*, 99(1), 2 (1977).

[397] V. Tvergaard, in *Advances in Applied Mechanics*, vol. 27, pp. 83–151, Elsevier (1989).

[398] A. Mackenzie, J. Hancock, and D. Brown, *Engineering Fracture Mechanics*, 9(1), 167 (1977).

[399] F. A. McClintock, *Journal of Applied Mechanics*, 35(2), 363 (1968). 102

[400] T. J. Ahrens and H. Tan. Shock consolidation of cubic boron nitride with whiskers of silicon compounds, U.S. Patent 4,863,881, issued September 5 (1989). 102

[401] H. Coker, M. Meyers, and J. Wessels, *Journal of Materials Science*, 26(5), 1277 (1991). 102

[402] L. H. Yu, M. A. Meyers, and T. Peng, *Materials Science and Engineering: A*, 132, 257 (1991). 102

[403] T. Vreeland Jr, P. Kasiraj, A. Mutz, and N. Thadhani, *Shock consolidation of a glass-forming crystalline powder*, vol. 231, Marcel Dekker (1986). 102

[404] V. Linse. Dynamic compaction of metal and ceramic powders, nmab-394 (1983). DOI: 10.1007/978-1-4613-2411-9_20 102

[405] W. H. Gourdin, *Progress in Materials Science*, 30(1), 39 (1986).

[406] R. Prümmer, *Materialwissenschaft und Werkstofftechnik*, 20(12), 410 (1989).

[407] M. Meyers, N. Thadhani, L. Yu, et al., *Shock Waves for Industrial Applications*, Noyes, NJ, 265 (1988).

[408] J. Beatty, L. Meyer, M. Meyers, S. Nemat-Nasser, M. Meyers, L. Murr, and K. Staudhammer, *Shock-Wave and High-Strain Rate Phenomena in Materials* (1992).

[409] M. A. Meyers, K. P. Staudhammer, and L. E. Murr, *Metallurgical Applications of Shock-Wave and High-Strain-Rate Phenomena*, Dekker (1986).

[410] T. Z. Blazynski, *Explosive Welding, Forming and Compaction*, Springer Science and Business Media (2012). DOI: 10.1007/978-94-011-9751-9

[411] R. Varin, L. Zbroniec, T. Czujko, and Y. K. Song, *Materials Science and Engineering: A*, 300(1–2), 1 (2001).

[412] K. S. Vandersall and N. N. Thadhani, *Metallurgical and Materials Transactions A*, 34(1), 15 (2003).

[413] L. J. Kecskes, R. Benck, and P. Netherwood Jr, *Journal of the American Ceramic Society*, 73(2), 383 (1990).

[414] A. M. Staver, in *Shock Waves and High-Strain-Rate Phenomena in Metals*, pp. 865–880, Springer (1981). DOI: 10.1007/978-1-4613-3219-0_49

[415] N. Thadhani, N. Chawla, and W. Kibbe, *Journal of Materials Science*, 26(1), 232 (1991).

[416] E. Szewczaka, J. Paszula, A. Leonov, and H. Matyja, *Materials Science and Engineering: A*, 226, 115 (1997). 102, 104, 105

[417] L. J. Kecskes and I. W. Hall, *Journal of Materials Processing Technology*, 94(2–3), 247 (1999). 102

[418] G. Kalandadze, S. Shalamberidze, and A. Peikrishvili, *Journal of Solid State Chemistry*, 154(1), 194 (2000). 105, 106

[419] R. H. Webb, *Reports on Progress in Physics*, 59(3), 427 (1996). 107

[420] A. F. Gmitro and D. Aziz, *Optics Letters*, 18(8), 565 (1993).

[421] G. J. Tearney, R. Webb, and B. Bouma, *Optics Letters*, 23(15), 1152 (1998).

[422] K. Lindfors, T. Kalkbrenner, P. Stoller, and V. Sandoghdar, *Physical Review Letters*, 93(3), 037401 (2004).

[423] E. U. Donev, R. Lopez, L. C. Feldman, and R. F. Haglund Jr., *Nano Letters*, 9(2), 702 (2009). 107

[424] A. J. Schwartz, M. Kumar, B. L. Adams, and D. P. Field, *Electron Backscatter Diffraction in Materials Science*, Springer (2000). DOI: 10.1007/978-1-4757-3205-4 107

[425] F. Humphreys, *Journal of Materials Science*, 36(16), 3833 (2001).

[426] D. J. Prior, A. P. Boyle, F. Brenker, M. C. Cheadle, A. Day, G. Lopez, L. Peruzzo, G. J. Potts, S. Reddy, R. Spiess, et al., *American Mineralogist*, 84(11–12), 1741 (1999).

[427] A. J. Wilkinson, G. Meaden, and D. J. Dingley, *Ultramicroscopy*, 106(4–5), 307 (2006).

[428] S. I. Wright, M. M. Nowell, and D. P. Field, *Microscopy and Microanalysis*, 17(3), 316 (2011).

[429] M. Kamaya, A. J. Wilkinson, and J. M. Titchmarsh, *Nuclear Engineering and Design*, 235(6), 713 (2005).

[430] T. B. Britton, S. Birosca, M. Preuss, and A. J. Wilkinson, *Scripta Materialia*, 62(9), 639 (2010). 107

[431] I. Gutierrez-Urrutia, S. Zaefferer, and D. Raabe, *Scripta Materialia*, 61(7), 737 (2009). 107

[432] I. Gutierrez-Urrutia and D. Raabe, *Acta Materialia*, 59(16), 6449 (2011).

[433] B. Simkin and M. Crimp, *Ultramicroscopy*, 77(1–2), 65 (1999).

[434] D. E. Newbury, D. C. Joy, P. Echlin, C. E. Fiori, and J. I. Goldstein, in *Advanced Scanning Electron Microscopy and X-Ray Microanalysis*, pp. 87–145, Springer (1986). DOI: 10.1007/978-1-4757-9027-6

[435] M. A. Crimp, *Microscopy Research and Technique*, 69(5), 374 (2006). 107

[436] G. Binnig, C. F. Quate, and C. Gerber, *Physical Review Letters*, 56(9), 930 (1986). 107

[437] H. J. Butt, B. Cappella, and M. Kappl, *Surface Science Reports*, 59(1–6), 1 (2005).

[438] Y. Martin, C. Williams, and H. K. Wickramasinghe, *Journal of Applied Physics*, 61(10), 4723 (1987). DOI: 10.1063/1.338807

[439] G. Meyer and N. M. Amer, *Applied Physics Letters*, 57(20), 2089 (1990).

[440] S. Alexander, L. Hellemans, O. Marti, J. Schneir, V. Elings, P. K. Hansma, M. Longmire, and J. Gurley, *Journal of Applied Physics*, 65(1), 164 (1989). DOI: 10.1063/1.342563 107

[441] T. F. Kelly and M. K. Miller, *Review of Scientific Instruments*, 78(3), 031101 (2007). 107

[442] M. K. Miller, *Atom Probe Tomography: Analysis at the Atomic Level*, Springer Science and Business Media (2012). DOI: 10.1007/978-1-4615-4281-0

[443] M. Miller, E. Kenik, K. Russell, L. Heatherly, D. Hoelzer, and P. Maziasz, *Materials Science and Engineering: A*, 353(1–2), 140 (2003).

[444] D. N. Seidman, *Annual Review of Materials Research*, 37, 127 (2007).

[445] M. Miller and E. Kenik, *Microscopy and Microanalysis*, 10(3), 336 (2004). 107

[446] R. F. Egerton, *Electron Energy-Loss Spectroscopy in the Electron Microscope*, Springer Science and Business Media (2011). DOI: 10.1007/978-1-4615-6887-2 107

[447] H. Ibach and D. L. Mills, *Electron Energy Loss Spectroscopy and Surface Vibrations*, Academic press (2013). DOI: 10.1007/bf02725821

[448] G. Gensterblum, J. Pireaux, P. Thiry, R. Caudano, J. Vigneron, P. Lambin, A. Lucas, and W. Krätschmer, *Physical Review Letters*, 67(16), 2171 (1991).

[449] R. F. Egerton, *Reports on Progress in Physics*, 72(1), 016502 (2008). 107

[450] D. Bell and A. Garratt-Reed, *Energy Dispersive X-Ray Analysis in the Electron Microscope*, Garland Science (2003). 107

[451] S. Brodowski, W. Amelung, L. Haumaier, C. Abetz, and W. Zech, *Geoderma*, 128(1–2), 116 (2005). 107

[452] L. A. Giannuzzi and F. A. Stevie, *Micron*, 30(3), 197 (1999). 107

[453] L. A. Giannuzzi, et al., *Introduction to Focused Ion Beams: Instrumentation, Theory, Techniques and Practice*, Springer Science and Business Media (2004). DOI: 10.1007/b101190

[454] C. A. Volkert and A. M. Minor, *MRS Bulletin*, 32(5), 389 (2007).

[455] J. Melngailis, *Journal of Vacuum Science and Technology B: Microelectronics Processing and Phenomena*, 5(2), 469 (1987).

[456] A. A. Tseng, *Journal of Micromechanics and Microengineering*, 14(4), R15 (2004).

[457] R. Wirth, *Chemical Geology*, 261(3–4), 217 (2009). 107

[458] W. A. Kalender, *Physics in Medicine and Biology*, 51(13), R29 (2006). 108

[459] U. Bonse and F. Busch, *Progress in Biophysics and Molecular Biology*, 65(1–2), 133 (1996).

[460] P. J. Schilling, B. R. Karedla, A. K. Tatiparthi, M. A. Verges, and P. D. Herrington, *Composites Science and Technology*, 65(14), 2071 (2005).

[461] V. Cnudde and M. N. Boone, *Earth-Science Reviews*, 123, 1 (2013). 108

[462] A. S. Eggeman and P. A. Midgley, in *Advances in Imaging and Electron Physics*, vol. 170, pp. 1–63, Elsevier (2012). 108

[463] E. F. Rauch, J. Portillo, S. Nicolopoulos, D. Bultreys, S. Rouvimov, and P. Moeck, *Zeitschrift für Kristallographie International Journal for Structural, Physical, and Chemical Aspects of Crystalline Materials*, 225(2–3), 103 (2010).

[464] J. Portillo, E. F. Rauch, S. Nicolopoulos, M. Gemmi, and D. Bultreys, in *Materials Science Forum*, vol. 644, pp. 1–7, Transactions on Tech Publ (2010).

[465] J. L. Rouviere, A. Béché, Y. Martin, T. Denneulin, and D. Cooper, *Applied Physics Letters*, 103(24), 241913 (2013). 108

[466] R. Pease and W. Nixon, *Journal of Scientific Instruments*, 42(2), 81 (1965). 108

[467] P. Buseck, J. Cowley, and L. Eyring, *High-Resolution Transmission Electron Microscopy: An Associated Techniques*, Oxford University Press (1989).

[468] Y. Ikuhara and P. Pirouz, *Microscopy Research and Technique*, 40(3), 206 (1998).

[469] W. Jiang and M. Atzmon, *Acta Materialia*, 51(14), 4095 (2003). 108

[470] P. D. Nellist, in *Science of Microscopy*, pp. 65–132, Springer (2007). DOI: 10.1007/978-0-387-49762-4_2 108

[471] D. A. Muller, *Nature Materials*, 8(4), 263 (2009).

[472] S. Findlay, N. Shibata, H. Sawada, E. Okunishi, Y. Kondo, T. Yamamoto, and Y. Ikuhara, *Applied Physics Letters*, 95(19), 191913 (2009).

[473] N. Dellby, L. Krivanek, D. Nellist, E. Batson, and R. Lupini, *Microscopy*, 50(3), 177 (2001). 108

[474] C. Burch and J. Stock, *Journal of Scientific Instruments*, 19(5), 71 (1942). 108

[475] C. J. Mann, L. Yu, C. M. Lo, and M. K. Kim, *Optics Express*, 13(22), 8693 (2005).

[476] S. Mayo, T. Davis, T. Gureyev, P. Miller, D. Paganin, A. Pogany, A. Stevenson, and S. Wilkins, *Optics Express*, 11(19), 2289 (2003).

[477] A. Snigirev, I. Snigireva, V. Kohn, S. Kuznetsov, and I. Schelokov, *Review of Scientific Instruments*, 66(12), 5486 (1995). 108

[478] B. M. Weon, J. H. Je, Y. Hwu, and G. Margaritondo, *International Journal of Nanotechnology*, 3(2–3), 280 (2006).

[479] S. Wilkins, T. E. Gureyev, D. Gao, A. Pogany, and A. Stevenson, *Nature*, 384(6607), 335 (1996).

[480] V. Ingal and E. Beliaevskaya, *Journal of Physics D: Applied Physics*, 28(11), 2314 (1995). DOI: 10.1088/0022-3727/28/11/012

[481] P. Cloetens, R. Barrett, J. Baruchel, J. P. Guigay, and M. Schlenker, *Journal of Physics D: Applied Physics*, 29(1), 133 (1996). DOI: 10.1088/0022-3727/29/1/023 108

[482] H. Gleiter, in *Advanced Structural and Functional Materials*, pp. 1–37, Springer (1991). DOI: 10.1007/978-3-642-49261-7_1 108

[483] M. A. Meyers, A. Mishra, and D. J. Benson, *Progress in Materials Science*, 51(4), 427 (2006).

[484] C. Koch, *Nanostructured Materials*, 2(2), 109 (1993).

[485] C. Suryanarayana, *International Materials Reviews*, 40(2), 41 (1995).

[486] R. Birringer, *Materials Science and Engineering: A*, 117, 33 (1989).

[487] K. Darling, A. Roberts, Y. Mishin, S. Mathaudhu, and L. Kecskes, *Journal of Alloys and Compounds*, 573, 142 (2013).

[488] S. Turnage, M. Rajagopalan, K. Darling, P. Garg, C. Kale, B. Bazehhour, I. Adlakha, B. Hornbuckle, C. Williams, P. Peralta, et al., *Nature Communications*, 9(1), 2699 (2018). 108

[489] Y. Iwahashi, Z. Horita, M. Nemoto, J. Wang, and T. G. Langdon, *Scripta Materialia*, 35(2) (1996). 108

[490] N. Tsuji, Y. Saito, H. Utsunomiya, and S. Tanigawa, *Scripta Materialia*, 40(7), 795 (1999).

[491] R. Valiev, E. Kozlov, Y. F. Ivanov, J. Lian, A. Nazarov, and B. Baudelet, *Acta Metallurgica et Materialia*, 42(7), 2467 (1994).

[492] R. Valiev, A. Korznikov, and R. Mulyukov, *Materials Science and Engineering: A*, 168(2), 141 (1993).

[493] R. Masumura, P. Hazzledine, and C. Pande, *Acta Materialia*, 46(13), 4527 (1998).

[494] N. Tsuji, Y. Ito, Y. Saito, and Y. Minamino, *Scripta Materialia*, 47(12), 893 (2002). 108

[495] J. W. Yeh, S. K. Chen, S. J. Lin, J. Y. Gan, T. S. Chin, T. T. Shun, C. H. Tsau, and S. Y. Chang, *Advanced Engineering Materials*, 6(5), 299 (2004). 108

[496] B. Gludovatz, A. Hohenwarter, D. Catoor, E. H. Chang, E. P. George, and R. O. Ritchie, *Science*, 345(6201), 1153 (2014).

[497] C. J. Tong, M. R. Chen, J. W. Yeh, S. J. Lin, S. K. Chen, T. T. Shun, and S. Y. Chang, *Metallurgical and Materials Transactions A*, 36(5), 1263 (2005).

[498] C. J. Tong, Y. L. Chen, J. W. Yeh, S. J. Lin, S. K. Chen, T. T. Shun, C. H. Tsau, and S. Y. Chang, *Metallurgical and Materials Transactions A*, 36(4), 881 (2005).

[499] Y. Zhang, T. T. Zuo, Z. Tang, M. C. Gao, K. A. Dahmen, P. K. Liaw, and Z. P. Lu, *Progress in Materials Science*, 61, 1 (2014).

[500] O. Senkov, G. Wilks, J. Scott, and D. Miracle, *Intermetallics*, 19(5), 698 (2011). 108

[501] Y. Kawamura and M. Yamasaki, *Materials Transactions*, 48(11), 2986 (2007). 108

[502] M. Yamasaki, M. Sasaki, M. Nishijima, K. Hiraga, and Y. Kawamura, *Acta Materialia*, 55(20), 6798 (2007).

[503] X. Shao, Z. Yang, and X. Ma, *Acta Materialia*, 58(14), 4760 (2010).

[504] Y. Zhu, A. Morton, and J. Nie, *Acta Materialia*, 58(8), 2936 (2010).

[505] K. Hagihara, N. Yokotani, and Y. Umakoshi, *Intermetallics*, 18(2), 267 (2010).

[506] K. Hagihara, A. Kinoshita, Y. Sugino, M. Yamasaki, Y. Kawamura, H. Yasuda, and Y. Umakoshi, *Acta Materialia*, 58(19), 6282 (2010).

[507] M. Matsuda, S. Ii, Y. Kawamura, Y. Ikuhara, and M. Nishida, *Materials Science and Engineering: A*, 393(1–2), 269 (2005). 108

[508] B. Mueller, *Assembly Automation*, 32(2) (2012). 108

[509] T. Niendorf and F. Brenne, *Materials Characterization*, 85, 57 (2013).

[510] W. E. Frazier, *Journal of Materials Engineering and Performance*, 23(6), 1917 (2014).

[511] T. M. Mower and M. J. Long, *Materials Science and Engineering: A*, 651, 198 (2016).

[512] T. Tancogne-Dejean, A. B. Spierings, and D. Mohr, *Acta Materialia*, 116, 14 (2016). 108

[513] A. R. T. Perez, D. A. Roberson, and R. B. Wicker, *Journal of Failure Analysis and Prevention*, 14(3), 343 (2014). 108

[514] G. I. Peterson, M. B. Larsen, M. A. Ganter, D. W. Storti, and A. J. Boydston, *ACS Applied Materials and Interfaces*, 7(1), 577 (2014). 108

[515] V. K. Champagne, *The Cold Spray Materials Deposition Process: Fundamentals and Applications*, Elsevier (2007). DOI: 10.1201/9781439824122 108

[516] R. Dykhuizen and M. Smith, *Journal of Thermal Spray Technology*, 7(2), 205 (1998).

[517] M. Grujicic, C. Zhao, W. DeRosset, and D. Helfritch, *Materials and Design*, 25(8), 681 (2004).

[518] A. Papyrin, V. Kosarev, S. Klinkov, A. Alkhimov, and V. M. Fomin, *Cold Spray Technology*, Elsevier (2006). 108

[519] G. He, J. Eckert, W. Löser, and L. Schultz, *Nature Materials*, 2(1), 33 (2003). 108

[520] S. C. Tjong, *Advanced Engineering Materials*, 9(8), 639 (2007).

[521] L. Huang, L. Geng, A. Li, F. Yang, and H. Peng, *Scripta Materialia*, 60(11), 996 (2009). 108

[522] H. Hermawan, H. Alamdari, D. Mantovani, and D. Dube, *Powder Metallurgy*, 51(1), 38 (2008). 108

[523] Y. Kawamura, K. Hayashi, A. Inoue, and T. Masumoto, *Materials Transactions*, 42(7), 1172 (2001).

[524] R. M. German, *Powder Metallurgy and Particulate Materials Processing: The Processes, Materials, Products, Properties, and Applications*, Metal Powder Industries Federation, Princeton (2005).

[525] C. Goh, J. Wei, L. Lee, and M. Gupta, *Nanotechnology*, 17(1), 7 (2005).

[526] T. Schubert, W. Zieliński, A. Michalski, T. Weißgärber, B. Kieback, et al., *Scripta Materialia*, 58(4), 263 (2008). 108

[527] D. Schurig, J. Mock, B. Justice, S. A. Cummer, J. B. Pendry, A. Starr, and D. Smith, *Science*, 314(5801), 977 (2006). 108

[528] N. I. Landy, S. Sajuyigbe, J. Mock, D. Smith, and W. Padilla, *Physical Review Letters*, 100(20), 207402 (2008).

[529] J. Valentine, S. Zhang, T. Zentgraf, E. Ulin-Avila, D. A. Genov, G. Bartal, and X. Zhang, *Nature*, 455(7211), 376 (2008).

[530] H. T. Chen, W. J. Padilla, J. M. Zide, A. C. Gossard, A. J. Taylor, and R. D. Averitt, *Nature*, 444(7119), 597 (2006).

[531] S. Enoch, G. Tayeb, P. Sabouroux, N. Guérin, and P. Vincent, *Physical Review Letters*, 89(21), 213902 (2002).

[532] J. K. Gansel, M. Thiel, M. S. Rill, M. Decker, K. Bade, V. Saile, G. von Freymann, S. Linden, and M. Wegener, *Science*, 325(5947), 1513 (2009).

[533] G. Dolling, M. Wegener, C. M. Soukoulis, and S. Linden, *Optics Letters*, 32(1), 53 (2007).

[534] R. Shelby, D. Smith, S. Nemat-Nasser, and S. Schultz, *Applied Physics Letters*, 78(4), 489 (2001). 108

[535] V. Segal, *Materials Science and Engineering: A*, 271(1–2), 322 (1999). 108

[536] A. P. Zhilyaev and T. G. Langdon, *Progress in Materials Science*, 53(6), 893 (2008). 109

[537] Y. Saito, H. Utsunomiya, N. Tsuji, and T. Sakai, *Acta Materialia*, 47(2), 579 (1999). 109

[538] B. R. Sunil, *Materials and Manufacturing Processes*, 30(10), 1262 (2015). 109

[539] Q. Cui and K. Ohori, *Materials Science and Technology*, 16(10), 1095 (2000). 109

[540] I. Endo, R. Okuno, H. Satake, I. Otsuka, H. Yamamoto, A. Shintani, M. Yoshino, and M. Yagi, *Journal of the Japan Society of Powder and Powder Metallurgy*, 48(8), 697 (2001). 109

[541] S. Fujino, N. Kuroishi, M. Yoshino, T. Mukai, Y. Okanda, and K. Higashi, *Scripta Materialia*, 37(5), 673 (1997). 109

[542] Y. Gupta, S. J. Turneaure, K. Perkins, K. Zimmerman, N. Arganbright, G. Shen, and P. Chow, *Review of Scientific Instruments*, 83(12), 123905 (2012). 109

[543] S. J. Turneaure, N. Sinclair, and Y. Gupta, *Physical Review Letters*, 117(4), 045502 (2016).

[544] S. J. Turneaure, P. Renganathan, J. Winey, and Y. Gupta, *Physical Review Letters*, 120(26), 265503 (2018).

[545] B. Nagler, B. Arnold, G. Bouchard, R. F. Boyce, R. M. Boyce, A. Callen, M. Campell, R. Curiel, E. Galtier, J. Garofoli, et al., *Journal of Synchrotron Radiation*, 22(3), 520 (2015).

[546] F. Seiboth, L. Fletcher, D. McGonegle, S. Anzellini, L. Dresselhaus-Cooper, M. Frost, E. Galtier, S. Goede, M. Harmand, H. Lee, et al., *Applied Physics Letters*, 112(22), 221907 (2018).

[547] P. Loubeyre, R. LeToullec, D. Hausermann, M. Hanfland, R. Hemley, H. Mao, and L. Finger, *Nature*, 383(6602), 702 (1996).

[548] J. Hu, K. Ichiyanagi, H. Takahashi, H. Koguchi, T. Akasaka, N. Kawai, S. Nozawa, T. Sato, Y. C. Sasaki, S. I. Adachi, et al., *Journal of Applied Physics*, 111(5), 053526 (2012). DOI: 10.1063/1.3692080

[549] A. Gleason, C. Bolme, H. Lee, B. Nagler, E. Galtier, D. Milathianaki, J. Hawreliak, R. Kraus, J. Eggert, D. Fratanduono, et al., *Nature Communications*, 6, 8191 (2015).

[550] C. H. Lu, E. Hahn, B. Remington, B. Maddox, E. Bringa, and M. Meyers, *Scientific Reports*, 5, 15064 (2015). 109

Author's Biography

CYRIL L. WILLIAMS

Dr. Cyril L. Williams, P.E. is currently a Senior Research Engineer at the U.S. Army Research Laboratory. He is a Fellow of the American Society of Mechanical Engineers (ASME), Fellow of the African Scientific Institute (ASI), U.S. Army Research Laboratory Distinguish Scholar, and Federal Engineer of the Year 2015 (Department of the Army). He earned his B.Sc. and M.Sc. in Mechanical Engineering (Fatigue and Fracture) from the University of Maryland Baltimore County, then M.Sc. and Ph.D. in Mechanical Engineering (Shock Compression Science) from The Johns Hopkins University. He is currently the Army's Subject Matter Expert (SME) on the structure-property relationships in condensed matter under extreme dynamic environments. He started his career as a design engineer with the American Bottlers Equipment Company (AMBEC) in 1992 and later joined E. I. DuPont de Nemours & Co. in 2000 as a Consultant in Reliability and Mechanical Testing (Engineering Mechanics Group). Dr. Williams is a licensed Professional Engineer in Delaware (#13160) and Maryland (#44307). He is currently the executive head of ASME Government Relations (Delaware Section), member of the American Physical Society (APS)-Shock Compression of Condensed Matter (SCCM) Executive Committee and an active member of several research societies including the Sigma Xi, Society of Experimental Mechanics (SEM), The Minerals, Metals and Materials Society (TMS), and Tau Beta Pi Engineering Honor Society (TBP). He has given numerous invited talks nationally and internationally including University of Cambridge (Cavendish Laboratory), California Institute of Technology, Imperial College London (Institute of Shock Physics), and the Massachusetts Institute of Technology.